Challenge Journal of

CONCRETE RESEARCH LETTERS

Vol.16 No.1 (2025)

acoustic emission aerated concrete artificial neural network compressive strength corrosion cracking ductility durability energy absorption ferrocement flexural strength fly ash fracture mechanics mechanical properties mortar nanoparticle reinforced concrete self-compacting concrete steam curing strengthening superplasticizer tensile strength workability waste disposal water absorption

TULPAR ACADEMIC PUBLISHING

ISSN 2548-0928

Challenge Journal of Concrete Research Letters

E-mail: *cjcrl@challengejournal.com*

Web page: *cjcrl.challengejournal.com*

Tulpar Academic Publishing
www.tulparpublishing.com

Challenge Journal of Concrete Research Letters

CONTENTS

Research Articles

TULPAR ACADEMIC PUBLISHING

Challenge Journal of Concrete Research Letters

Research Article

Assessment of stresses and vibration behavior of concrete gravity dam under fluctuating hydrostatic force

Pandimani [a,*]

[a] *GMR Institute of Technology, Rajam, Vizianagaram District, 532127 Andhra Pradesh, India*

ABSTRACT

Dam structure contributes to the socio-economic development of a country but zero probability of failure of such structure is a design concern. Hence, it is essential to monitor the dam condition under the fluctuating reservoir water and the vibration effect. In this investigation, four different cases of the reservoir depths are adopted to numerically analyze the hydrostatic and modal (free-vibration) behavior of a three-dimensional (3D) gravity dam. The impact of fluctuating reservoir water and uplift pressure on the dam's internal stresses (direct, principal, shear, and Von Mises) are evaluated to examine the location of maximum stress concentration. Under these cases, the maximum displacement along the longitudinal and vertical directions is explored. It can be revealed that case 1 (with full reservoir) induces the maximum displacement on the top crest level and the peak normal stress concentrated at the heel region, respectively. The mode shapes 1 and 4, under case 4 reveals the peak and lowest time-period. Whereas, the frequency responses are in contrast to it (i.e., reverse) under the same case and modes. In comparison to cases 2, 3, and 4, case 1 exhibit the largest crest level displacements along the x-direction that are 26%, 49%, and 86% higher, respectively. Compared to case 1, the normal stresses along the x-direction declined by 51.58%, 68.74%, and 58.25%, respectively for cases 2, 3, and 4. It can be revealed that the frequency is directly related, while the time-period is inversely proportional to the mode-shapes. Overall, this study envisages a comprehensive understanding of the dam's performance, providing critical data to inform design decisions, safety assessments, and performance improvements.

ARTICLE INFO

Article history:
Received – July 16, 2024
Revision requested – September 14, 2024
Revision received – September 18, 2024
Accepted – September 26, 2024

Keywords:
Stress analysis
3D modeling
Dam-reservoir structure
Time-period
Frequency
Mode shapes

Citation: Pandimani (2025). Assessment of stresses and vibration behavior of concrete gravity dam under fluctuating hydrostatic force. *Challenge Journal of Concrete Research Letters*, 16(1), 1–14.

1. Introduction

In water resource management, structural integrity is essential to ensure the safety and longevity of water-retaining structures like gravity dams. The significant challenge for ensuring the safety of such structures relies on the fluctuating reservoir and uplift pressure effect, which compromise the stability and durability of a dam. Understanding the effect of these forces is crucial for improving the dam's performance and ensuring its structural safety. It is also essential to understand the dynamic effect, which causes severe damage to the dam structure due to the vibration. The mode shape and frequency behavior of the dam structure is a critical parameter that essentially provides valuable insights into the structural performance of the dam. It also assists engineers in predicting the potential weaknesses within the dam body and optimizing the design for durability and safety concerns. Understanding the causes and mechanisms of the structural deformation process is essential for the safety of man-made dam structures, for protecting the environment, and for the establishment of associated mitigating measures in the event of natural disasters. The impounding reservoir of a dam can cause natu-

* *Corresponding author*. Tel.: +91-89191-17823 ; E-mail address: pandimani918@gmail.com (Pandimani)
ISSN: 2548-0928 / DOI: https://doi.org/10.20528/cjcrl.2025.01.001

ral tragedies like earthquakes and the sudden collapsing of such a structure would cause severe devastation of property and human life. The environmental consequences of dam construction would have direct impacts on the physical, biological, and chemical features of rivers and riparian environments. In recent years, the evolution of vibration damage and the impact of impounding reservoir pressure have become major concerns for the safety and serviceability of dams. Reservoir and dam construction involves substantial anthropogenic and natural impacts. They are mostly positive effects but sometimes it influences the negative impact on the environment. The main purpose of dam construction involves the improvement of the local water regime which consequently enhances the national prosperity. The socioeconomic developments of the country by generating power, irrigation of cultivated land, municipal water supply, navigation, and flood control are the main goals of constructing the reservoir and dam. However, the consequences of dam construction have also some negative environmental impacts such as migration of local people, drastic changes in the reservoir's aquatic life, and natural hazards, which cannot be avoided. The structure of a solid gravity dam can be built with concrete or stone masonry material constructed to form the backwater reservoir. The lateral reservoir pressure is primarily resisted by the weight of the dam. The dam considered in this study is a multi-purpose irrigation project that is under construction across the River Godavari, located in the districts of West and East Godavari of Andhra Pradesh.

A comparative study between two and three-dimensional arch dams (gravity-type) were performed considering earth and reservoir pressure influence on the longitudinal displacement. The reservoir depth was 6.2m lowered and the effect of displacements on the crest level was investigated. It was demonstrated that both three and two-dimensional studies correlated closely with the experimental tests (Žvanut 2022). Two-dimensional static responses under fluctuating reservoir levels considering the dam structure and soil interaction were investigated through the ANSYS package. It was demonstrated that the highest crest displacement was achieved for a flexible foundation compared to a rigid one. It was inferred that beyond 2H width and 1.5H depth of foundation, the dam stresses are insignificant on the foundation-structure interaction effect (Sharma and Nallasivam 2023). A two-dimensional high-gravity dam was analyzed under 0.1 g to 0.3 g lateral ground motion to investigate the stability and stress conditions. It was concluded that the stability of the dam has been endangered by increasing earthquake intensity. It was suggested that the numerical shear and vertical stress magnitudes are more conservative than the gravity method (Ali et al. 2012). To investigate the safety measures of the dam under seismic forces, a finite element approach was employed using the domain reduction method and free-field boundary condition methods and the stresses and displacements results are compared. Later the domain reduction method was employed considering the foundation as rigid, mass, and massless for the Koyna dam. It was revealed that the dam responses are overestimated for the massless foundation type (Ghaemian et al. 2019). An appropriate finite element method (free-field boundary condition) using ABAQUS was implemented considering the effects of radiation damping, mass, and wave propagation. The responses of the foundation-dam effect assuming mass and massless were evaluated. It was illustrated that the foundation with massless assumption overestimates the magnitude of stresses and displacements (Mohammadnezhad et al. 2019). Earthquake analysis was done numerically using a case study of Koyna dam for the dam-structure interaction effect and the results are validated with past literature. A foundation with mass was assumed and the damage indices, crack evolution, displacements, and principal stresses were evaluated. The simulated result specifies that the massed foundation has a significant influence on the seismic performance of the gravity dam (Burman et al. 2008). A parametric numerical analysis was performed to explore the impact of the flexibility and rigidity foundations type on the free vibration frequency characteristics of the dam. The dam was also studied with and without the prestress effect. It was predicted that the dam with initial prestress would exhibit more frequency than that without prestressing case. It was also suggested that the initial condition and boundary conditions should be considered while assessing the dam responses under the foundation-dam interaction effect (Jafari and Khiavi 2019). A 2D roller compacted concrete dam was analyzed for dynamic responses to examine the effect of the shape and size of the gallery using the ABAQUS package. It was demonstrated that the circular shape gallery performed better regarding stress concentration, deflection, and crack formation, compared to the octagonal and square shapes (Ghaedi et al. 2016). A numerical study was executed to extract the responses of the dam structure foundation interaction assuming rigid and flexible boundaries. A numerical study was further extended to investigate the optimum depth and width of the foundation. It was concluded as related to the fixed base type, the flexible (considering foundation) base produced 10 times higher deflection. It was examined that the optimum foundation width of twice the dam height and optimum depth of 1.5 times the height of the dam was achieved (Abraham et al. 2017). Modal analysis of the gravity dam was numerically simulated considering different reservoir and tail-water levels and the effect of reservoir-foundation-dam interactions. It was concluded that the highest lateral deformation occurred under lower reservoir depth. The higher reservoir height with tail-water height offers more flexibility and reduced frequency. In contrast to the interaction between reservoir water and dam structure, the interaction between the reservoir water, dam, and foundation combination produces lesser frequency (Tidke and Adhikary 2022).

This paper highlights the 3D reservoir pressure modeling and stresses analysis of the Polavaram project gravity dam profile, which is rarely presented in the past literature. The study explores the impact of varying the u/s, uplift, and d/s water forces to investigate the peak stress concentration and displacement region within the dam. Excessive stresses within the dam can lead to a cracking or failure of concrete material, which compromises the integrity of the structure. Engineers can iden-

tify the potential zone of weakness that may require reinforcement or design adjustments to prevent any catastrophic failure. Excessive displacements can potentially lead to the overturning and sliding of dams, hence monitoring the displacement behavior under fluctuating reservoir forces ensures the dam remains within safe operating limits. It also evaluates the vibration behavior to examine the natural frequency and mode shape parameters to assess the potential weakness area inside the body of the dam. It is possible to optimize the dam geometry and materials consumption by accurately predicting the peak stresses and displacement parameters before the commencement of dam construction. It also ensures the dam structure is resilient to both static and dynamic loadings. The presented model can be adopted as a reference to examine the influence of other significant factors on dam stability and its responses to external forces, which is a future scope of this study.

2. Gravity Dam Modeling

The Indian government designated the Polavaram dam project a significant undertaking in Andhra Pradesh, as a national project (Amarnath and Shashidhar 2020). It is situated in the Godavari River and is regarded as the region's most important infrastructure undertaking. It is a multi-use dam that is being built for irrigation and hydroelectric power, and it has the potential to be the largest dam in India. The non-overflow sectional view of the dam is shown in Fig. 1, which depicts the various parameters concerning the dam. In this section, a 3D gravity dam is analyzed using STAAD Pro V8i package. The dam is studied for 4 different u/s reservoirs and tailwater depths, to assess the critical regions of displacements and stresses within the body of the dam.

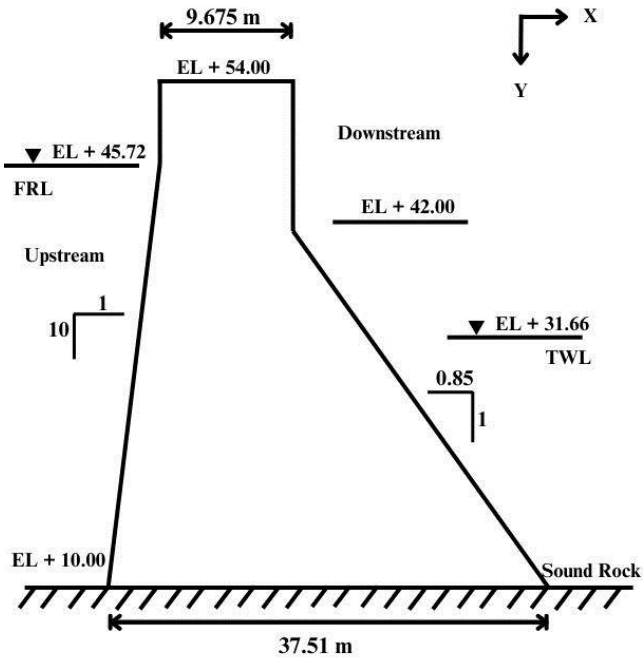

Fig. 1. Sectional view of the gravity dam (Amarnath and Shashidhar 2020).

The non-overflow section is 54m high, 9.675m in top width, and 37.51m in bottom width. In this study, the 3D structure of a dam of 20m in length is assumed for analysis purposes. From the base, an inclination of 10:1 up to a height of 35.72m and then vertically upward till the top crest level on the upstream (u/s) side. It has a downstream (d/s) slope of 1:0.85 up to a height of 32m and then vertically upward till the top crest level of the dam. A water depth of 21.66m is avail on the downstream side with a Full Reservoir Level (FRL) of 35.72m available on the upstream side respectively (with a dam base lying at RL of +10m). STAAD Pro, commercial version is an extensively employed design and structural analysis software developed by Research Engineers International (STAAD Pro 2007). Later in 2005, it was bought by Bentley Systems. It is capable of modeling structural steel, timber, cement concrete, and other composite structural elements with design codes of several nations. It is capable of performing, various geometric and material linear as well as nonlinear static and dynamic analyses. In STAAD Pro, three basic methods are available for developing the geometry of the structure such as the snap node method, coordinate method, and copy-paste method. It also consists of a few default structural models in its command wizard library for frames, solids, and truss-type structures. In this study, a default cuboid solid model is used to generate a 3D dam structure by the coordinate system method in the STAAD editor. The research methodology employed to perform this analysis work is represented in Fig. 2.

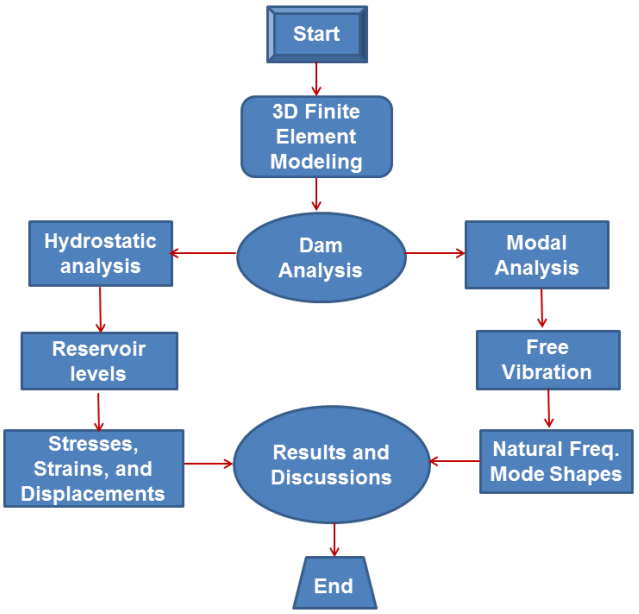

Fig. 2. Methodology used for dam analysis in STAAD Pro.

Unlike shell (plate) elements and members, solid elements do not require any attributes. However, constants such as the Poisson's ratio and elasticity modulus must be given. In addition, density needs to be provided in each load case where self-weight is included. Solid elements enable the solution of structural problems with general three-dimensional stresses. A powerful tool for solid components finite element analysis is offered for a

class of problems, including the distribution of stress in rock and soil strata or concrete dams. In this study, an eight-node, isoparametric solid element is employed to develop the dam model using STAAD Pro. Each node of this solid element has freedom in three translational directions, and the geometry shape is illustrated in Fig. 3.

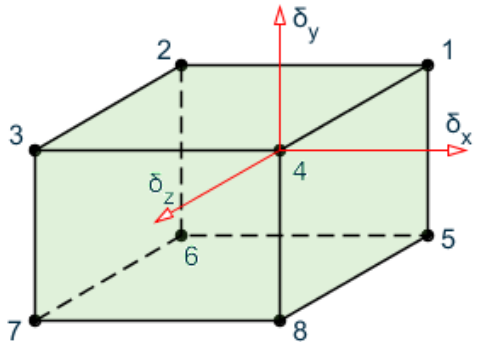

Fig. 3. Eight-node isoparametric element (STAAD Pro 2007).

It is likely to impose uniform and linearly varying pressure on the faces of the solid element through the solid load tab. On a face, a volumetric type of pressure is applied, where the intensity at one node may differ from another node within the same face. This kind of load is defined by the water weight on a dam's sloping face. If the dam is represented with solids for each component, the water height at the lower elevation nodes will be higher than those at the higher elevation nodes. The pressure can be applied in the local z-direction (normal to the element) or the global directions (i.e., x, y, and z). If we neglect the global orientation, we assume that the applied loading is normal to the face and that a positive pressure is entering the solid. At the four corner nodes of the dam section, the boundary conditions at supports are given zero displacements and rotations (fixed) in the translational directions (i.e., x, y, and z). To perform the static and modal analysis, the self-weight of the dam is input by assigning linear elastic material properties (i.e., Density and Poisson's ratio) of concrete (Pandimani et al. 2023a, 2023b). Table 1 illustrates the geometric details of the dam-reservoir structure. Table 2 represents the modulus of elasticity, Poisson's ratio, weight density, and damping ratio values that are employed in this study. The concrete grade of M35 is assumed for the 3D solid model.

Among various studied cases: Case 1: 35.72 m of reservoir water level and 21.66 m of tailwater, Case 2: 30.72 m of reservoir water level and 17.66 m of tailwater, Case 3: 25.72 m of reservoir water level and 13.66 m of tailwater, and Case 4: 35.72 m of reservoir water level with no tail-water, are the various cases assumed for the dam's analysis. The dam's dead load (self-weight), pressure due to uplift, downstream water pressure, and upstream hydrostatic pressure are the forces exerted on the dam's surface (FRL). 35.72 meters is the reservoir's upstream depth, and 21.66 meters is the highest tail-water level. A non-overflow section of the dam has a height of 44 meters. The rock foundation of the non-overflow section is available at an elevation of 10m. The top and bottom widths are 9.675m and 37.51m respectively. On the u/s and d/s sides of the dam, there is a slope of one horizontal to ten vertical and 0.85 horizontal to one vertical, respectively. The analysis assumes a 20-meter length for the dam.

Table 1. Dam-reservoir data considered.

S.No.	Parameters	Value
1	Full Reservoir depth	35.72 m
2	Maximum depth of tail water	21.66 m
3	Height of the dam	44.00 m
4	Sound rock level	10.00 m
5	Width of the dam at the bottom	37.51 m
6	Width of the dam at the top	9.675 m
7	Length of the dam considered	20.00 m
8	Upstream slope	1H:10V
9	Downstream slope	0.85H:1V

Table 2. Material properties.

S.No.	Particulars	Type/Value
1	Type of material	Concrete
2	Type of element	Solid 8-node quadrilateral
3	Young's modulus of concrete (E_c)	29580.39 N/mm^2
4	Density of concrete (D_c)	2.5 E-5 N/mm^3
5	Density of water	9810 N/m^3
6	Poisson's ratio (PRXY)	0.30
7	Damping ratio (DAMP)	0.05
8	Concrete grade	M35

3. Hydrostatic Reservoir Loadings

The solid loading diagrams for various reservoir water levels at the upstream, downstream, and uplift faces are shown in this section. As shown in Fig. 4, three forces: upstream reservoir thrust, uplift pressure, and downstream tail-water pressure are modeled as solid volume pressures acting on the corresponding faces of 3D solid elements. Throughout the length (20m) of a gravity dam, a trapezoidal (for cases 1-3) and triangular (for case 4) volumetric uplift pressure (varying load) is acting at the dam's bottom face. Whereas a varying triangle volumetric pressure is acting at the upstream and downstream faces of the dam respectively.

This study uses four case studies, as shown in Fig. 4(a-d), to determine the static and modal responses. For the first case, the water level in the u/s and d/s is 35.72m and 21.66m respectively. The reservoir depth or the second case are 30.72m u/s and 17.66m d/s respectively. The third case has water levels of 25.72m and 13.66m u/s and d/s respectively. In the last scenario, the reservoir depth is 35.72 meters on the u/s side, and there is no tail-water in the d/s face. The water level in the u/s and d/s faces affected the uplift pressure in each of the four examples. The volumetric pressure (solid hydrostatic) exerted on the different regions of the dam is shown by the green and blue colored diagram in Fig. 4.

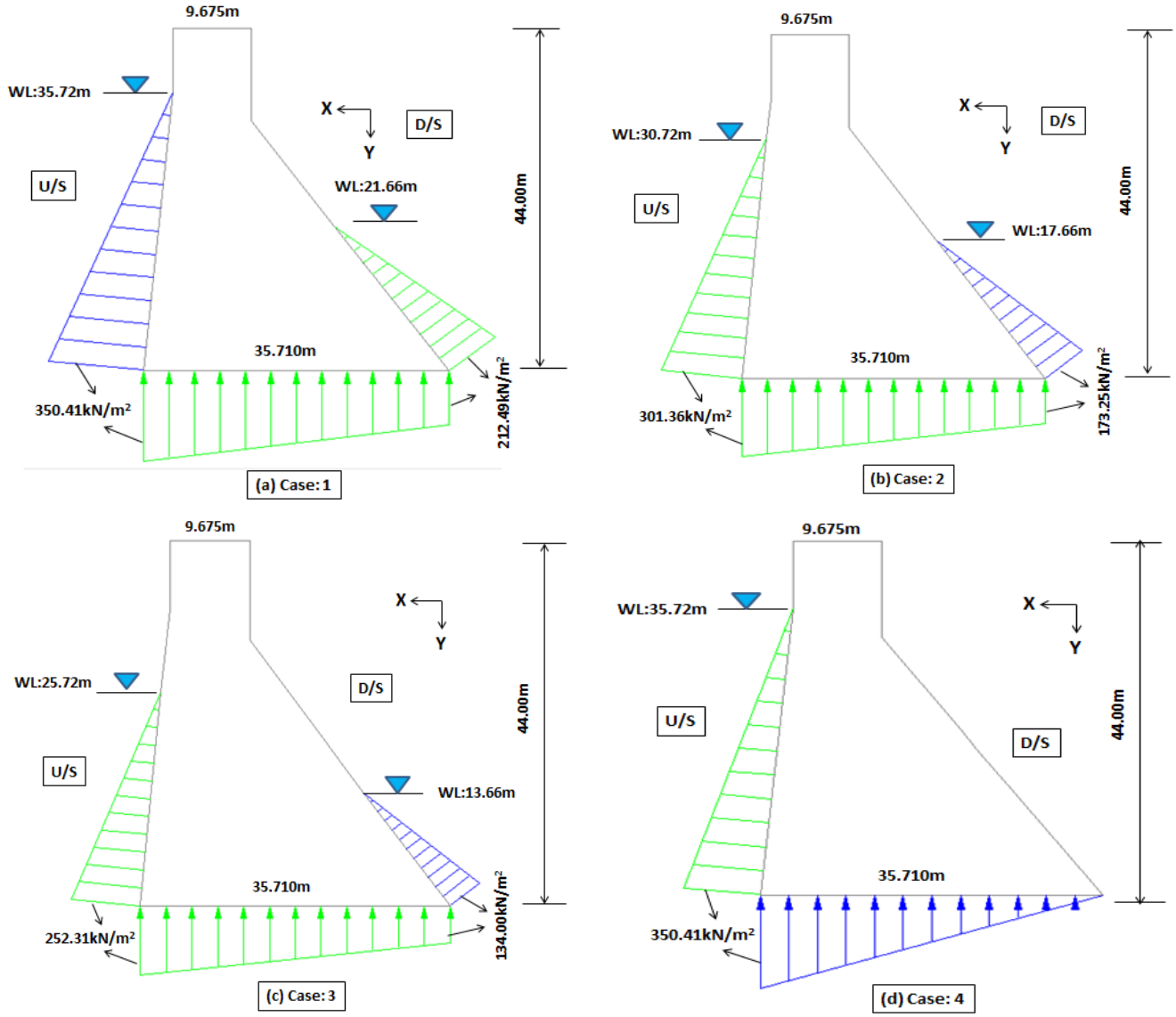

Fig. 4. Hydrostatic pressure loading diagram: (a) Case 1; (b) Case 2; (c) Case 3; (d) Case 4.

The theoretical formula presented in Eqs. (1) to (4) are employed to compute the pressure magnitudes at upstream, tail-water, and uplift, respectively (Punmia et al. 2009). The evaluated theoretical pressure intensities under various studied cases are presented in the subsequent section below.

The u/s reservoir pressure at dam base:

$$P_{(u/s)} = \gamma_w \cdot h_1 \quad (1)$$

The d/s pressure due to tail water at dam base:

$$P_{(d/s)} = \gamma_w \cdot h_2 \quad (2)$$

Uplift pressure at dam base (u/s):

$$P_{u1} = \gamma_w \cdot h_1 \quad (3)$$

Uplift pressure at dam base (d/s):

$$P_{u2} = \gamma_w \cdot h_2 \quad (4)$$

where, h_1 = u/s side height of reservoir (m); h_2 = d/s side tail-water height (m); γ_w = density of water (kN/m^3).

4. Results and Discussion

This section includes the proposed 3D solid gravity dam's graphical representation and analysis of the results under different reservoir depths and tail-water water levels. Additionally, modal behavior and the free vibration effect are illustrated. The results of solid loading are discussed, and visual representations of the stress analyses under various loading conditions and their variations in stresses are provided. Additionally, graphs illustrating how natural frequency varies under different mode shapes are displayed.

4.1. Stress analysis

Demonstrates the various case studies employed in this study to investigate the impact of fluctuating reservoir pressure exerting over the dam body. The responses like direct stress, von-Mises stress, shear stress, and principal stresses are extracted numerically and the results are interpreted comprehensively.

Table 3. Details of the hydrostatic loading cases.

S.No.	Particular details	Case-1	Case-2	Case-3	Case-4
1	Height of reservoir in the upstream (h_1), m	35.72	30.72	25.72	35.72
2	Height of tail-water in the downstream (h_2), m	21.66	17.66	13.66	0
3	Density of water (γ_w), kN/m^3	9.81	9.81	9.81	9.81
4	Reservoir u/s pressure at the top, kN/m^2	0	0	0	0
5	Reservoir u/s pressure at the bottom, kN/m^2	350.42	301.36	252.31	350.42
6	Uplift pressure in the upstream face, kN/m^2	350.42	301.36	252.31	350.42
7	Uplift pressure in the downstream face, kN/m^2	212.48	173.24	134.00	0
8	Pressure on the d/s face at the top due to tailwater, kN/m^2	0	0	0	0
9	Pressure on d/s face at the bottom due to tailwater, kN/m^2	212.48	173.24	134	0

4.1.1. Case study 1

In this case, the elevation of the u/s reservoir and tail-water is at 35.72m (FRL) and 21.66m respectively as shown in Fig. 4(a). A u/s reservoir pressure of 0 kN/m^2 atmospheric pressure and 350.420 kN/m^2 at the dam's heel portion was applied. Similarly, uplift pressures of 350.420 kN/m^2 and 212.48 kN/m^2 were applied on the dam heel and toe region respectively. A 0 kN/m^2 and 212.480 kN/m^2 were assigned at the 21.66m level (atmospheric) and toe of the dam as tail water pressure. Maximum normal stresses of magnitudes 285 kN/m^2 (comp.), 105 kN/m^2 (tensile), 147 kN/m^2 (comp.), and 147 kN/m^2 (tensile) are predicted along the x- and y-direction respectively, as illustrated in Table 5. The maximum displacement of 616.987 mm and 188.759 mm is produced along the x- and y-directions as presented in Table 4, which occurs at the dam's top crest region.

The largest and lowest von-Mises stress and principal stress of 376 kN/m^2 (comp.), 52.3 kN/m^2 (comp.) and 164 kN/m^2 (comp.), 1.13 kN/m^2 (tensile) are developed under case 1, as presented in Table 6. The dam's heel region exhibits the highest direct stress along the x-direction, whereas the u/s side of the dam experiences the highest normal stress in the y-direction respectively, as revealed in Fig. 5(a-b). The largest and lowest von-Mises contour stresses, which are concentrated at a dam's mid-height on the u/s side and top crest, respectively, are shown in Fig. 5(c). The findings indicate that, as depicted in Fig. 5(d), the top head region and the d/s side of the dam are where the least principal stress forms, and the largest principal stress occurs at the u/s face.

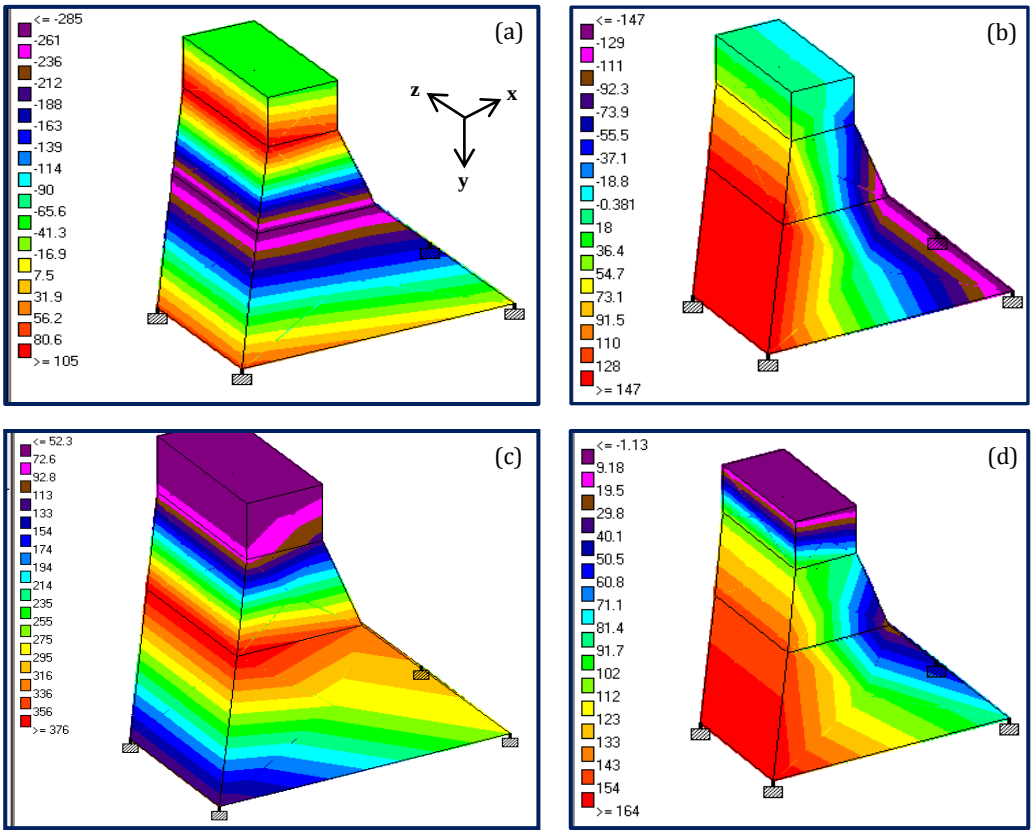

Fig. 5. Contour stress diagrams for case 1:
(a) Normal stress in x-direction; (b) Normal stress in y-direction; (c) von-Misses stress; (d) Principal stress.

4.1.2. Case study 2

As seen in Fig. 4(b), the level of the u/s water and tail-water in this case are at 30.72 m and 17.66 m, respectively. On the u/s side, a reservoir pressure of 0 kN/m² (atmospheric pressure) and 301.360 kN/m² were applied at the dam's heel region. Similarly, the uplift pressure at the dam toe and heel portion was 173.240 kN/m² and 301.360 kN/m², respectively. A tail-water pressure of 0 kN/m² and 173.240 kN/m² is assigned at 17.66m height and dam toe portion, respectively. Fig. 6(a-b) show the predicted highest and least normal stresses along the x- and y-directions, respectively. The magnitudes of these stresses are 138 kN/m² (comp.), 40.9 MPa (tensile), 126 kN/m² (comp.), and 96 kN/m² (tensile), respectively.

The highest crest level of the dam developed a maximum displacement of 456.208 mm (x-dir.) and 299.092 mm (y-dir.), as shown in Table 4. The largest and lowest von-Mises and principal stresses of 207 kN/m² (tensile), 19.9 kN/m² (tensile), and 98.2 kN/m² (tensile), 1.13 kN/m² (tensile) are developed under case 2. The highest and lowest von-Mises stresses develop at the top reservoir level on the u/s face and top crest region of the dam respectively, as shown in Fig. 6(c). It was revealed that the largest principal stress developed at the u/s side and the lowest principal stress formed at the top head region on the d/s side of the dam, as shown in Fig. 6(d). The normal stresses along the x- and y-directions are maximum on the u/s face and minimum on the d/s face of the dam respectively and illustrated in Fig. 6(a-b). Tables 5 and 6 illustrate the predicted stress results of normal, von-Mises, and principal stresses respectively.

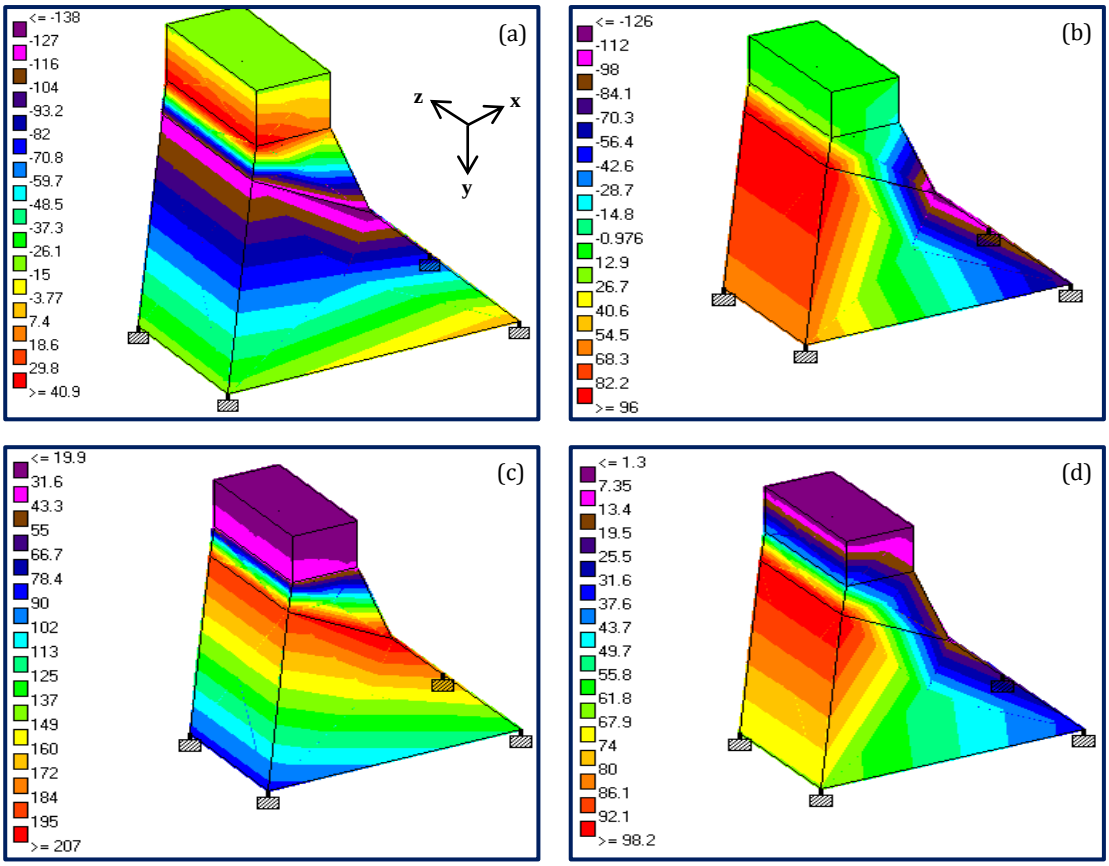

Fig. 6. Contour stress diagrams for case 2:
(a) Normal stress in x-direction; (b) Normal stress in y-direction; (c) von-Misses stress; (d) Principal stress.

4.1.3. Case study 3

As seen in Fig. 4(c), the levels of the u/s water and tail-water in this case are 25.72 m and 13.66 m, respectively. On the u/s side, a reservoir pressure of 0 kN/m² (atmospheric pressure) and 252.310 kN/m² were applied at the dam's heel region. Likewise, the uplift pressure at the dam toe and heel was 134 kN/m² and 252.310 kN/m², respectively. A tail-water pressure of 0 kN/m² and 134 kN/m² were assigned at the 16.66m level and toe of the dam. As displayed in Fig. 7(a) and (b), maximum normal stresses of magnitude 89.1 kN/m² (comp.), 42.2 kN/m² (tensile), and 61.8 kN/m² (tensile), 77 kN/m² (comp.) are anticipated along the x- and y-directions, respectively.

Table 4 illustrates the maximum displacement of 311.859 mm and 87.97 mm was developed at the top crest region of the dam. Under case 3, the von-Mises and principal stresses of maximum and minimum magnitudes of 129 kN/m² (tension), 26.30 kN/m² (tension), and 67 kN/m² (comp.), 0.047 kN/m² (comp.), are developed. Fig. 7(c) illustrates the maximum and minimum von-Mises stresses that are concentrated at the top reservoir level and top crest portion of the dam respectively, on the u/s side. It is investigated that, as indicated

in Fig. 7(d), the least principal stress develops at the top head region and d/s face of the dam respectively. Furthermore, the largest principal stress concentrated on the u/s face. The largest and lowest normal stresses are developed on the dam's u/s and d/s faces along the x- and y-directions, respectively.

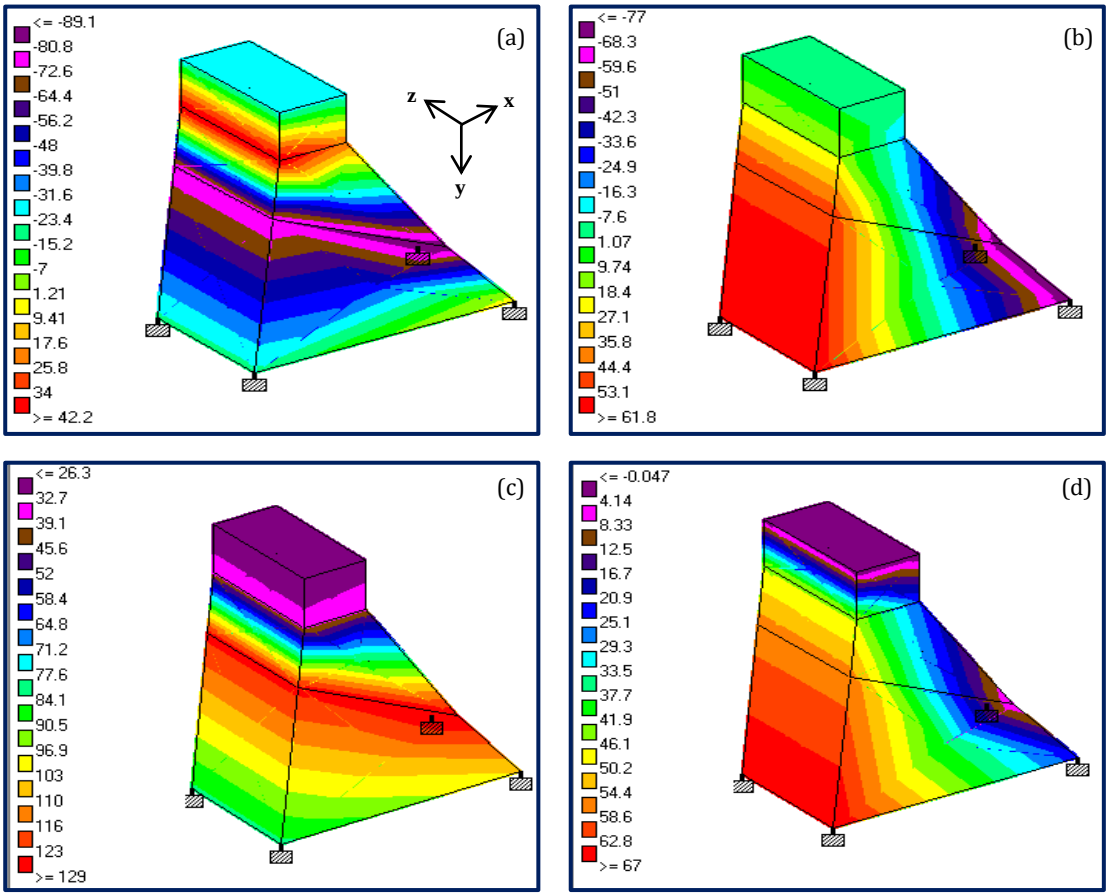

Fig. 7. Contour stress diagrams for case 3:
(a) Normal stress in x-direction; (b) Normal stress in y-direction; (c) von-Misses stress; (d) Principal stress.

4.1.4. Case study 4

As seen in Fig. 4(d), in this case, the height of the u/s levels is 35.72m (FRL.) with no tail-water. On the u/s side, a reservoir pressure of 0 kN/m^2 (atmospheric pressure) and 350.420 kN/m^2 were applied at the dam's heel region. Similarly, the uplift pressure at the dam toe and heel was set at 0 kN/m^2 and 350.420 kN/m^2, respectively. As displayed in Fig. 8(a) and (b), the maximum normal stresses of magnitudes 119 kN/m^2 (comp.), 12.8 kN/m^2 (comp.), and 222 kN/m^2 (comp.), 217 kN/m^2 (tensile), are anticipated along the x- and y-directions, respectively.

Tables 5 and 6 illustrate the predicted stress magnitudes of normal, von Mises, and principal stresses respectively. Table 4 illustrates the maximum displacement of 1369.199 mm and 395.058 mm was developed at the top crest level of the dam. The largest and lowest von-Mises and principal stresses of 321 kN/m^2 (tensile), 62.9 kN/m^2 (tensile) and 222 kN/m^2 (tensile), 14.60 kN/m^2 (comp.) are developed under case 4. The concentrations of the highest and minimum von-Mises stresses are developed at the d/s face and top head region of the dam respectively, as displayed in Fig. 8(c). As seen in Fig. 8(d), it was revealed that the lowest principal stress forms at the top crest region and d/s edge of the dam, whereas the largest principal stress forms at the u/s face.

4.2. Displacements

Table 4 illustrates the highest displacements along the x- and y-directions of a 3D gravity dam influenced by fluctuating levels of hydrostatic pressures. According to cases 1 through 4, the greatest displacements of magnitude 616.987 mm, 456.208 mm, 311.859 mm, and 87.970 mm in the x-direction and 188.759 mm, 299.092 mm, 369.199 mm, and 395.058 mm along the y-direction are anticipated. Table 4 and Fig. 9, illustrate that the maximum displacements in the x-direction descents as the reservoir depth lowers, but in contrast, this magnitude increases in the y-direction when the reservoir levels decrease. Fig. 9 shows that the greatest displacements in the x- and y-directions of 616.978 mm and 395.058 mm, respectively. In comparison to cases 2, 3, and 4, case 1 has displacements in the x-direction that are 26%, 49%, and 86% higher, respectively. Conversely, the greatest displacements under case 1 are 58%, 96%, and 109% smaller than those under cases 2, 3, and 4, respectively in the y-direction. It is determined that the dam's crest region is subjected to the largest displacements along the x- and y-directions, respectively.

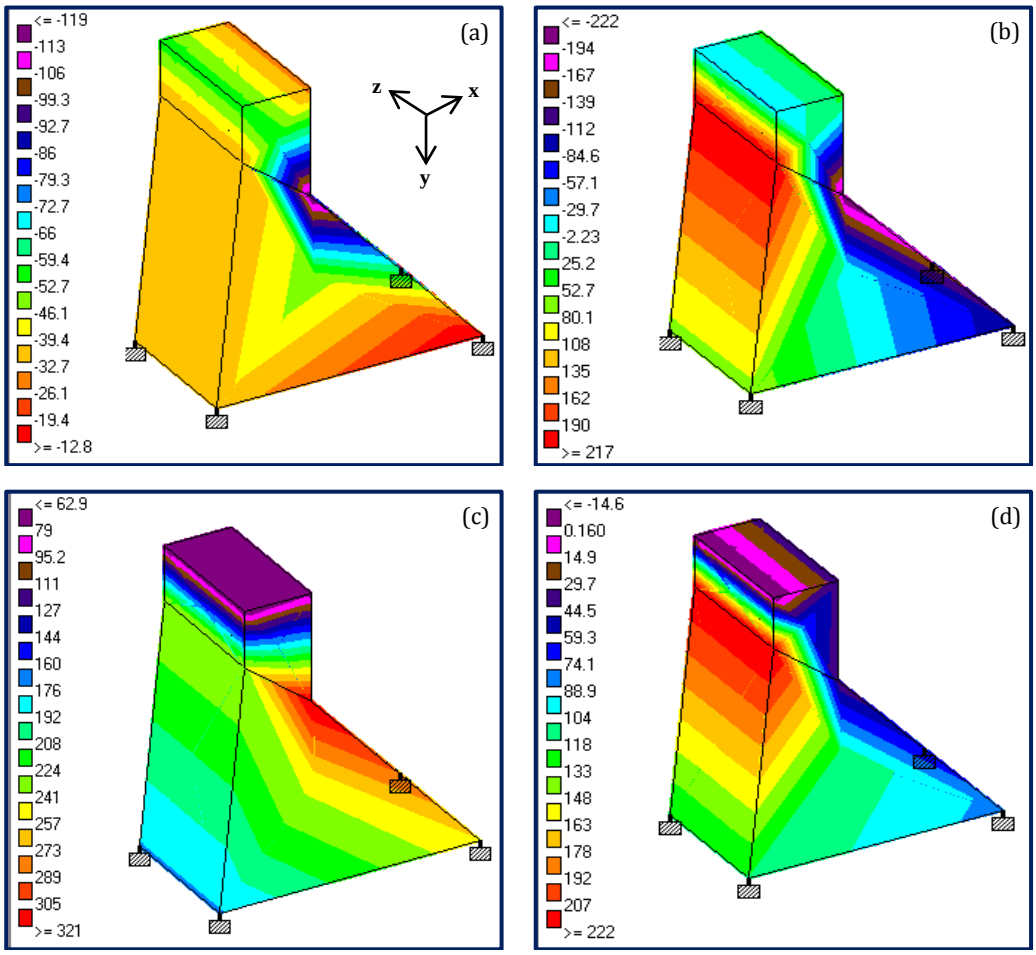

Fig. 8. Contour stress diagrams for case 4:
(a) Normal stress in x-direction; (b) Normal stress in y-direction; (c) von-Misses stress; (d) Principal stress.

Table 4. Maximum predicted displacements (mm).

Direction	Case 1	Case 2	Case 3	Case 4
x-	616.987	456.208	311.859	87.970
y-	188.759	299.092	369.199	395.058

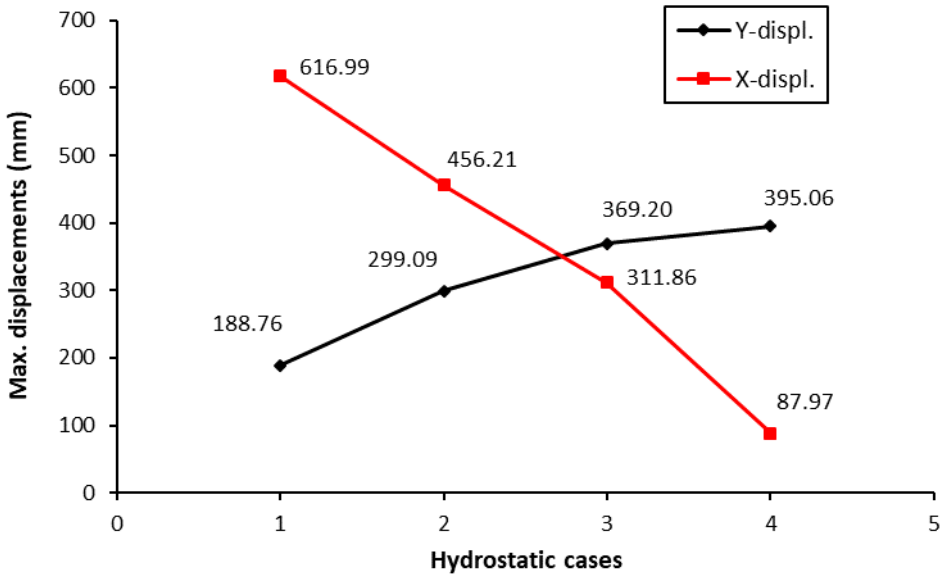

Fig. 9. Maximum node displacements along x- and y-directions.

4.3. Normal (direct) stress

Table 5 shows the expected maximum and minimum normal stress magnitudes along the x- and y-directions under the variable reservoir depths. As shown in Fig. 10, cases 1 through 4 cause maximum compressive stresses of magnitudes 285 kN/m², 138 kN/m², 89.10 kN/m², and 119 kN/m², respectively. It is observed that along the x-direction, every produced stress has a compressive nature. Similarly, as illustrated in Fig. 10, the highest stresses of magnitudes 147 kN/m², 126 kN/m², 61.80 kN/m², and 222 kN/m² were assessed for cases 1 through 4, respectively, along the y-direction. All other cases have compressive stresses in the y-direction, except case 3. Compared to case 1, the normal stresses in the x-direction for cases 2, 3, and 4 declined by 51.58%, 68.74%, and 58.25%.

Table 5. Maximum and minimum normal stresses (kN/m²).

Direction	Case1		Case 2		Case 3		Case 4	
	max	min	max	min	max	min	max	min
x-	-285	+105	-138	+40.9	-89.1	+42.2	-119	-12.8
y-	-147	+147	-126	+96	+61.8	-77	-222	+217

Note: (-) sign indicates compressive and (+) indicates tensile stresses.

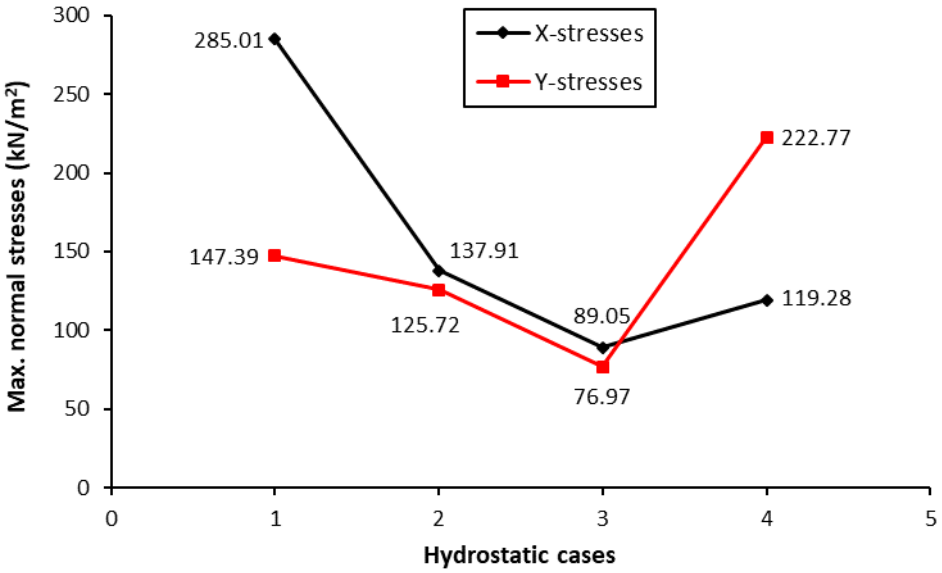

Fig. 10. Maximum normal stresses along x- and y-directions.

4.4. von-Mises and principal stresses

Table 6 displays the highest and lowest von-Mises and principal stresses for cases 1 to 4. The maximum von-Mises and principal stresses are depicted in Fig. 11. The maximum von-Mises stress of 376 kN/m² and 222 kN/m² are predicted under cases 1 and 4 respectively. In comparison to case 1, the maximum von-Mises stresses for cases 2, 3, and 4 are reduced by 44.95%, 65.70%, and 14.63%, respectively. Similar reductions of 40.12% and 59.15% are seen in the maximum principal stresses of cases 2 and 3, while a 35.37% rise is seen in case 4 relative to case 1. It is revealed that under the four different cases studied, all the principal stresses are tensile. It is examined that the maximum von-Mises stresses for case 1 is 14.63% higher than that of case 4, which reveals that it is 1.17 times that of case 4. In comparison to case 4, the maximum principal stress in case 1 decreased by 35.37%, indicating that it is 0.74 times greater than that of case 4.

Table 6. von-Mises and principal stresses (kN/m²).

	Case-1		Case-2		Case-3		Case-4	
	max	min	max	min	max	min	max	min
von-Mises stress	376	52.3	207	19.9	129	26.3	321	62.9
Principal stress	+164	-1.13	+98	+1.3	+67	-0.04	+222	-14.6

Note: (-) sign indicates compressive and (+) indicates tensile stresses.

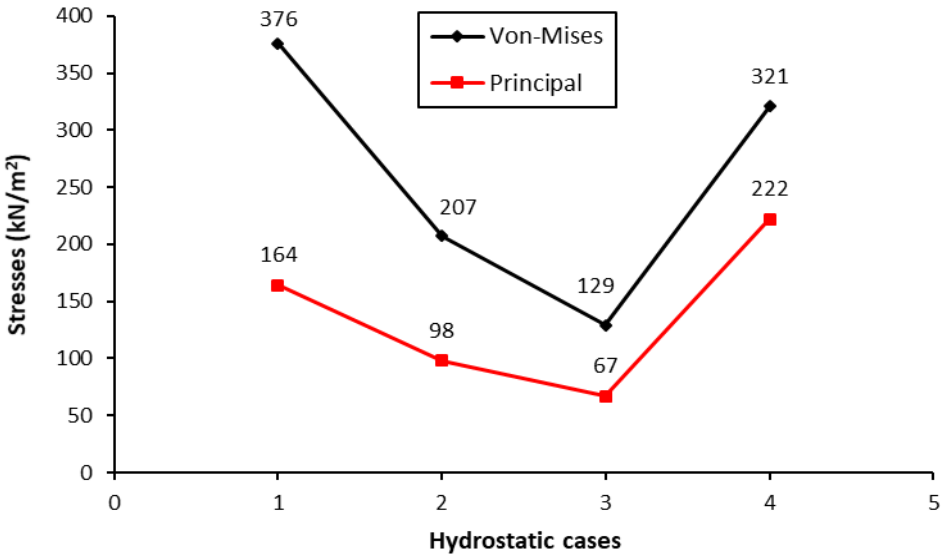

Fig. 11. Maximum von-Mises and principal stresses.

4.5. Shear stresses

Table 7 displays the maximum shear stresses in the x- and y-directions for various loading cases. It is revealed that case 4 develops the largest shear stresses. In the x-direction, the maximum shear stresses for cases 1 through 4 are, in order, 141.60 kN/m², 85.63 kN/m², 54.83 kN/m², and 135.42 kN/m² respectively. The highest shear stress magnitudes of 13.51 kN/m², 7.09 kN/m², 3.57 kN/m², and 19.08 kN/m² are recorded for cases 1 through 4, respectively, along the y-direction. It is investigated along the x-direction and found that, in comparison to case 1, case 2 offers a percentage reduction in maximum shear stress of 39.53. Similarly, in the x-direction, case 3 shows a percentage reduction in maximum shear stress of 35.97 and 61.28, respectively, when compared to cases 2 and 1. In comparison to case 1, case 4 exhibits an x-direction percentage reduction of 4.36 of the maximum shear stress. Conversely, for case 4, the maximum shear stress decreased by 58.15% and 146.98% along the x-direction respectively, when compared to cases 2 and 3.

Table 7. Maximum shear stresses (kN/m²).

Case	x-dir.	y-dir.
1	141.60	13.51
2	85.63	7.09
3	54.83	3.57
4	135.42	19.08

Furthermore, a comparison of cases 2 and 3 against case 1 along the y-direction reveals a reduction of maximum shear stress of 47.52 and 73.25 percent, respectively. In comparison to case 2, case 3 also yields a 49.65% reduction in shear stress. In contrast, the largest shear stress for case 4 in the y-direction is increased by 41.23%, 169.11%, and 434.45% compared to cases 1, 2, and 3, respectively.

4.6. Modal analysis

A method for determining the vibration specifications of the dam structure can be assessed using modal (frequency) analysis (Punmia et al. 2009; Asghari et al. 2018; Pandimani et al. 2023b). The vibration of any structure like dams can be made with force or without force and can generally be described as forced or free vibrations. Under free vibrations, the structure may oscillate at specific natural frequencies and periods, and the respective deformation is referred to as mode shape (Wang et al. 2021; Li et al. 2015; Khosravi and Heydari 2015).

The modal analysis is executed to establish the time-period, natural frequency, and respective mode shapes, which offers crucial information about the structure responses before the more realistic dynamic analysis (Punmia et al. 2009; Pandimani et al. 2023a, 2023b). Free vibration analysis is performed to extract the mode shape, time-period, and natural frequency (Hz) for the 4 solid models executed in this study. Fig.12 reveals that the natural frequency increases with the mode shape, i.e., the higher the mode number higher the frequency for all the cases. Fig.13(a-d) represent the different mode shapes from cases 1 to 4 respectively. Table 8 depicts the predicted natural frequencies and time periods under the studied cases.

Among the various cases and mode shapes, case 4 (without tail water pressure) under the fourth mode exhibits the highest natural frequency, as shown in Fig. 12. The highest time-period existed for case 1 under mode-4 and the least time-period for case 4 under mode-4 respectively, as shown in Table 8 and Fig.14. The variation of time-period under various modes of vibration is presented in Fig. 14. The natural frequency ranges from 0.571Hz to 1.503Hz for case 1, 0.660Hz to 2.819Hz for case 2, 1.062Hz to 3.733Hz for case 3, and 0.518Hz to 19.627Hz for case 4. It was concluded that the natural frequencies of mode number 4 in cases 1, 2, 3, and 4 are 2.63, 4.27, 3.52, and 37.88 times that of the first mode respectively. It is clear from Table 8 that the frequencies under the first mode increased by 15.59% for case 2

compared to case 1. The frequency is increased by 60.91% and 85.99% for case 3 in comparison to case 2 and case 1 respectively, for mode 1. In contrast, the frequency under case 4 declined by 9.28%, 21.52%, and 51.22% against the case 1, 2, and 3 respectively. Similarly, the mode 2 frequency under cases 2 and 3 are increased by 28.86% and 96.88% respectively, against case 1. Whereas, a 48.43% increase in frequency is achieved for case 3 in comparison to case 2. The frequency for the second mode under case 4 is increased by 6.70% and decreased by 17.19%, and 45.80% in comparison to cases 1, 2, and 3 respectively.

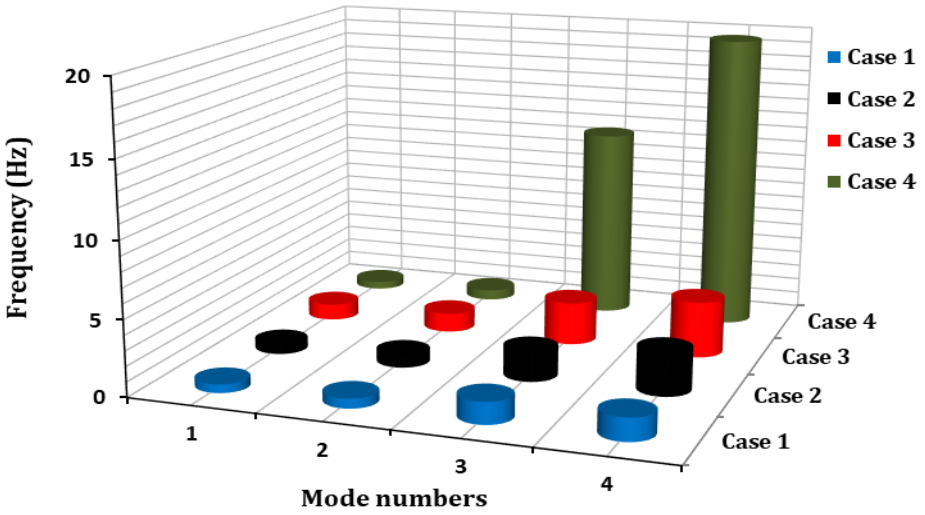

Fig. 12. Comparison of natural frequency.

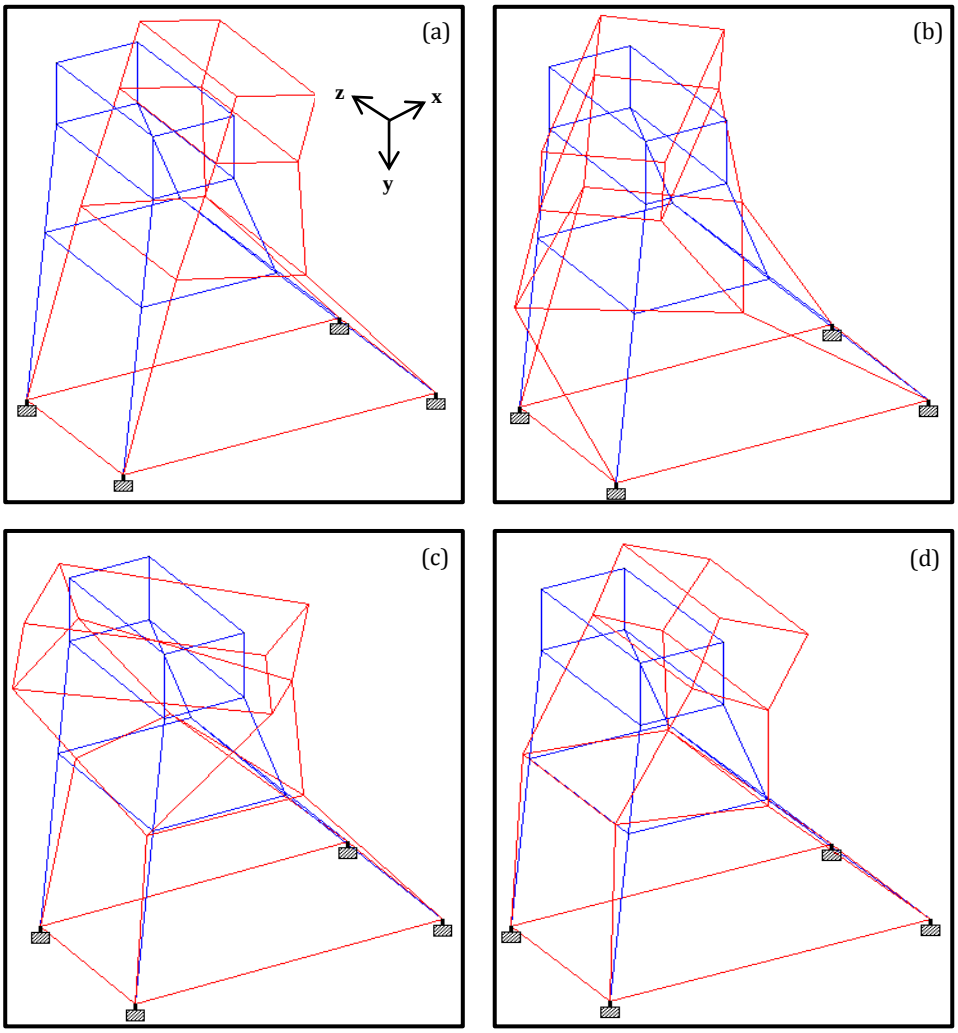

Fig. 13. Mode shapes of the dam section:
(a) Mode shape 1; (b) Mode shape 2; (c) Mode shape 3; (d) Mode shape 4.

Table 8. Modal analysis responses (free vibration).

Modes	Frequency (Hz)				Period (seconds)			
	Case-1	Case-2	Case-3	Case-4	Case-1	Case-2	Case-3	Case-4
1	0.571	0.660	1.062	0.518	1.752	1.516	0.941	1.932
2	0.641	0.826	1.262	0.684	1.561	1.210	0.793	1.462
3	1.448	1.968	2.842	12.620	0.691	0.508	0.352	0.079
4	1.503	2.819	3.733	19.627	0.665	0.355	0.268	0.051

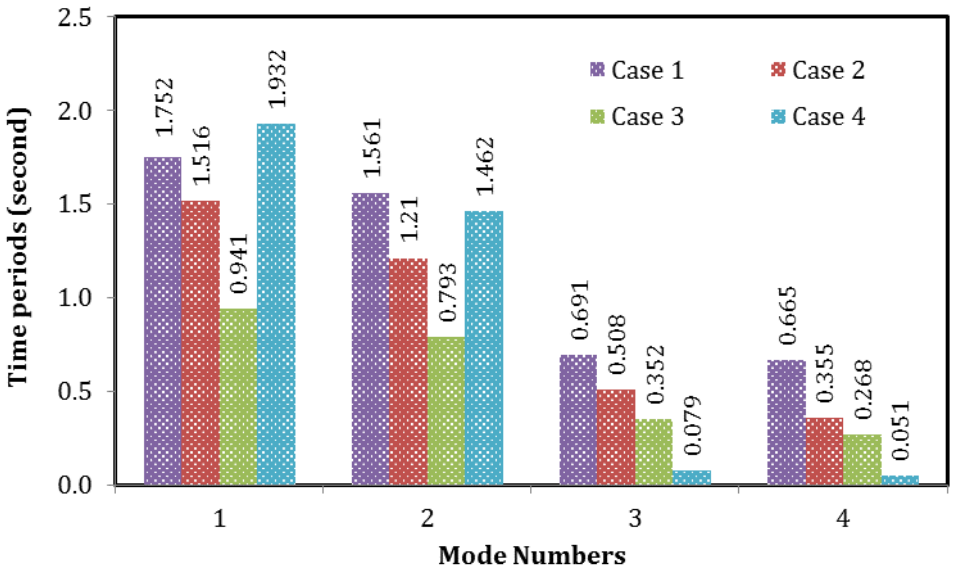

Fig. 14. Comparisons of time-periods.

Compared to case 1, the mode 3 frequency is increased by 35.91% and 96.27% for cases 2 and 3 respectively. Whereas, a 44.41% increased frequency is achieved for case 3 against case 2. A large variation in the frequency was experienced under the fourth mode in case 4 related to the other cases due to zero tail water pressure, as depicted in Table 8 and Fig. 12. An 88.56% and 148.37% increase in frequency are observed for case 2 and 3 respectively, in comparison to the case 1. Similarly, a 33.43% increase in frequency is exhibited for case 3 against case 2. Similarly, Compared to frequencies of cases 1, 2, and 3 for mode number 4, the highest percentage increments of 1205.85, 596.24, and 425.77 are obtained under case 4.

5. Conclusions

This study encompasses the 3D analysis of a solid gravity dam which demonstrates that the dam's static and vibration responses may be satisfactorily anticipated using the advanced structural analysis and design software (STAAD Pro) tool. The expected results are deemed significant, and the package's robustness through contour graphical representation and user-friendly environment offers a better comprehension of the dam responses. The major vibration properties (such as mode shape and vibration frequencies) of the dam structure are investigated through modal analysis. The critical observations of this research are illustrated below.

- The largest displacement for case 1 in the x-direction is increased by 85.74% compared to case 4, which reveals that it is 7.01 times more than that of case 4. On the other hand, the maximum displacement under case 1 decreased by 109.29% compared to case 4, meaning that it is 0.48 times larger in the y-direction than case 4.
- Cases 1 and 4 exhibit the largest normal stresses respectively, along the x- and y-directions. It is determined that, in comparison to case 4, case 1 achieves a 58.25% increase in normal stress along the x-direction. Furthermore, under case 1, a declining percentage of 51.02 is shown in the y-direction in comparison to case 4. It can be concluded that the induced tensile and compressive stresses are within the limiting strength of the materials.
- The von-Mises stresses in case 1 are found to be 1.82, 2.91, and 1.17 times greater than those in cases 2, 3, and 4, correspondingly. The primary stresses in cases 1, 2, 3, and 4 were found to be 1.67, 2.45, and 0.74 times greater, respectively. In case 1, the maximum shear stresses show 41.23% lower and 4.36% greater along the x- and y-directions, respectively, compared to case 4.
- It is demonstrated that the natural frequencies and time-periods increased with increasing mode numbers. It is revealed through modal analysis (under free vibration) that the maximum and minimum frequencies are predicted in case 4, under mode 4 and mode 1 respectively. As opposed to this, case 4 discloses the

maximum and minimum time-periods under modes 1 and 4, respectively.

The combination of a full reservoir with tail-water makes the dam more flexible, which consequently lowers the natural frequency. Conversely, in modal analysis, a reservoir with lower water depth leads to increased lateral crest deformation. A dam with a full reservoir and tail water results in a lower natural frequency than a dam without tail-water.

Acknowledgements

None declared.

Funding

The author received no financial support for the research, authorship, and/or publication of this manuscript.

Conflict of Interest

The author declared no potential conflicts of interest with respect to the research, authorship, and/or publication of this manuscript.

Data Availability

The datasets created and/or analyzed during the current study are not publicly available, but are available from the corresponding author upon reasonable request.

REFERENCES

Abraham M, Kuriakose B, Kuruvilla R (2017). Static analysis of gravity dams considering foundation-structure interaction. *Applied Mechanics and Materials*, 857, 237-242.

Ali MH, Alam MR, Haque MN, Alam MJ (2012). Comparison of design and analysis of concrete gravity dam. *Natural Resources*, 3(1), 31004.

Amarnath CR, Shashidhar T (2020). Study on backwater effect due to Polavaram Dam Project under different return periods. *Water,* 12(2), 576.

Asghari E, Taghipour R, Bozorgnasab M, Moosavi M (2018). Seismic analysis of concrete gravity dams considering foundation mass effect. *KSCE Journal of Civil Engineering*, 22, 4988-4996.

Burman A, Reddy BV, Maity D (2008). Seismic analysis of concrete gravity dams considering foundation flexibility and nonlinearity. *The 12th International Conference of International Association for Computer Methods and Advances in Geomechanics*, Goa, India.

Ghaedi K, Jameel M, Ibrahim Z, Khanzaei P (2016). Seismic analysis of Roller Compacted Concrete (RCC) dams considering effect of sizes and shapes of galleries. *KSCE Journal of Civil Engineering*, 20, 261-272.

Ghaemian M, Noorzad A, Mohammadnezhad H (2019). Assessment of foundation mass and earthquake input mechanism effect on dam–reservoir–foundation system response. *International Journal of Civil Engineering,* 17, 473-480.

Jafari SR, Khiavi P (2019). Parametric study of the modal behavior of concrete gravity dam by using finite element method. *Civil Engineering Journal*, 5(12), 2614-2625.

Khosravi S, Heydari MM (2015). Design and modal analysis of gravity dams by ANSYS parametric design language. *Walailak Journal of Science and Technology*, 12(2), 167-180.

Li M C, Guo XY, Shi J, Zhu ZB (2015). Seepage and stress analysis of anti-seepage structures constructed with different concrete materials in an RCC gravity dam. *Water Science and Engineering*, 8(4), 326-334.

Mohammadnezhad H, Ghaemian M, Noorzad A (2019). Seismic analysis of dam-foundation-reservoir system including the effects of foundation mass and radiation damping. *Earthquake Engineering and Engineering Vibration*, 18, 203-218.

Pandimani, Rao YD, Krishna IG (2024). FE modeling for ultimate behavior predictions of RC beam. *Asian Journal of Civil Engineering*, 25(1), 477-493.

Pandimani, Sankar TS, Priyatham BPRVS, Ramkumar BAV (2024). Evaluation of SSI impact on the structural performance of RC buildings. *Asian Journal of Civil Engineering*, 25(2), 1295-1307.

Punmia BC, Lal PBB, Jain AK, Jain AK (2009). Irrigation and Water Power Engineering. Laxmi Publications, Ltd., India.

Sharma A, Nallasivam K (2023). Static analysis of a concrete gravity dam using the finite element technique. *Asian Journal of Civil Engineering*, 24(8), 2939-2957.

STAAD Pro (2007). Technical reference manual. Research Engineers, a Bentley Solutions Center. www.bentley.com/staad.

Tidke AR, Adhikary S (2022). Vibration characteristics of gravity dams for varying reservoir and tailwater heights, and interaction effects. In *Symposium in Earthquake Engineering,* Singapore: Springer Nature Singapore, 171-180.

Wang C, Zhang H, Zhang Y, Guo L, Wang Y, Thira Htun TT (2021). Influences on the seismic response of a gravity dam with different foundation and reservoir modeling assumptions. *Water*, 13(21), 3072.

Žvanut P (2022). 3D finite element analysis of a concrete dam behavior under changing hydrostatic load: A case study. *Materials*, 15(3), 921.

Challenge Journal of Concrete Research Letters

Research Article

Photocatalytic activation of fibrous lightweight polymer concrete surfaces under artificial light source

Serdal Ünal [a], Mehmet Canbaz [a,*]

[a] *Department of Civil Engineering, Eskişehir Osmangazi University, 26480 Eskişehir, Türkiye*

ABSTRACT

In general, surface contamination of building materials is caused by pollution, which can be divided into human-made and natural sources. Building materials whose surfaces are exposed to pollutants from these sources for a long time show chemical and physical degradation and lose their function over time and their service life is shortened. Due to photocatalytic feature provided to the material surfaces, organic pollutants on the surface are degraded as a result of oxidation and reduction reactions under the influence of light. In this study, the self-cleaning performance was measured on the surfaces of fibrous lightweight polymer concretes with titanium dioxide (TiO_2) reinforcement incorporated into the structure. Perlite-based concrete specimens with TiO_2/resin ratios of 0%, 3%, 6% and 9% and fiber/resin ratios of 0%, 0.5% and 1% were prepared. When the results of the self-cleaning test with Rhodamine B dye were examined, the samples with a TiO_2/resin ratio of 9% had the highest degradation percentages of about 67%. This study shows that photocatalytic properties can be imparted to lightweight polymer concretes with different structures from conventional concrete by TiO_2 reinforcement.

ARTICLE INFO

Article history:
Received – September 5, 2024
Revision requested – September 30, 2024
Revision received – November 8, 2024
Accepted – November 19, 2024

Keywords:
Photocatalytic activation
Polymer concrete
Fiber
Self-cleaning

Citation: Ünal S, Canbaz M (2025). Photocatalytic activation of fibrous lightweight polymer concrete surfaces under artificial light source. *Challenge Journal of Concrete Research Letters*, 16(1), 15–24.

1. Introduction

Innovation in the construction industry and sustainability goals are driving the continuous evolution of materials science (Sui Pheng et al. 2019). Conventional concretes can have limitations in some applications, often due to their weight and various physical limitations (Seymour 2019). Concretes defined as lightweight concretes are concretes with a lower density than normal concretes. The density of these concretes is generally less than 1800 kg/m^3. The reason for the lower density of lightweight concretes is that these concretes are produced by using lightweight aggregates such as perlite, expanded clay, pumice or materials such as foam concrete. Such concretes can be preferred in both structural and non-structural applications (Khan et al. 2024; Thienel et al. 2020). Therefore, the search for lightweight and high performance alternatives has led to the development of polymer concretes (Nodehi 2022; Bedi et al. 2013). Polymer concretes are building materials that contain a variety of mineral and organic materials bound with resins, with optimized mechanical and chemical properties. These materials offer advantages such as light weight, high durability, and modifiability, providing a wide range of applications in construction (Sarde and Patil 2019). Cement-based concretes typically achieve a compressive strength of 30–35 MPa and a flexural strength of 7–8 MPa, whereas polymer concretes exhibit significantly higher strengths, reaching 90–100 MPa in compression and 20–25 MPa in flexure (Ulu 2024; Cakir 2022).

The use of polymer concretes in the field of building materials is increasing. Polymer concretes can be used in many different areas of use such as drainage channels,

* *Corresponding author*. Tel.: +90-222-239-3750 ; E-mail address: mcanbaz@ogu.edu.tr (M. Canbaz)
ISSN: 2548-0928 / DOI: https://doi.org/10.20528/cjcrl.2025.01.002

cable channels, tunnel coating elements, precast structural elements, wear-resistant ground roads, countertops, wall tiles, exterior coating elements, pool elements, and machine tool beds. In addition to its ability to be less labor-efficient, polymer concrete has higher mechanical strength and higher chemical resistance then classical concrete (Ulu 2024). Today, new studies are being carried out to reinforce polymer concretes, add various fibers and improve their physical properties (Kiruthika et al. 2021; Güler 2024; Rebeiz et al. 2004). The use of fibers in concrete aims to enhance its tensile strength by improving load-bearing capacity and bridging cracks, thereby preventing their propagation (Şengel et al. 2022).

The use of photocatalytic materials in construction building materials is rapidly expanding. Failure to protect the exterior surface of materials such as concrete, exterior paints, grouts, tile mosaics, plaster materials and coatings and the harboring of microorganisms can lead to serious problems (Haider et al. 2019). TiO_2 photocatalysis has become a real practical technology after the mid-1990s, especially in the field of building materials (Hashimoto 2005). The Jubilee Church in Rome, Italy, is the first building to contain self-cleaning concrete (Cedillo-Gonzalez et al. 2018). Self-cleaning properties are emerging as an important aspect to increase the sustainability of modern building materials (Ćurčić 2019; Folli et al. 2012). Contamination and staining on the surface of building materials are both aesthetically problematic and increase maintenance costs. Therefore, the self-cleaning ability of materials is of great importance in terms of reducing maintenance costs and achieving long-term cost-effectiveness (Zailan et al. 2017). Self-cleaning refers to the removal of contaminants and stains accumulated on the surface over time, and this process is usually achieved by additives with photocatalytic properties (Dikkar et al. 2021; Zhao et al. 2015). Titanium dioxide (TiO_2) plays an important role in this context. When exposed to UV light, TiO_2 oxidatively degrades contaminants, allowing the surface to be cleaned, thus maintaining the appearance and performance of the material for a long time (Beeldens 2006). This property increases the resistance of materials to environmental pollutants, reduces maintenance requirements and thus provides a cost-effective application (Ünal and Canbaz 2022). The generation of electron-hole pair for TiO_2 photocatalysis can be written as follows in Eq. (1) (Guo et al. 2019).

$$TiO_2 + hv \rightarrow h^+(TiO_2) + e^-(TiO_2) \quad (1)$$

If the reactions are briefly summarized; super oxygen (O_2•), hydroxy (•OH), peroxy (HO_2•) radicals are synthesized as a result of the reactions of the water and oxygen molecule groups on the surface and the trapping of gaps and electrons. These radicals thus produced realize photocatalytic redox reactions. The super oxygens, hydroxy and peroxy groups formed as a result of these oxidation and reduction reactions on the material surfaces break down the organic compounds on the material surface into harmless products. This photomineralization can be shown in a simple way as in Eq. (2) (Carp et al. 2004).

$$\text{organic compounds} \xrightarrow{\text{semiconductor}} CO_2 + H_2O + \text{mineral acid} \quad (2)$$

There are many studies on the use of concrete and resins in combination with fibers to produce different composite materials; however, there are no studies on materials lightened by perlite, showing photocatalytic properties and containing different proportions of fibers. There is also growing interest in studies on self-cleaning of various building material surfaces. Measuring the self-cleaning performance of materials such as the composite material produced in this study is one of the first studies in this field. In this study, the effects of TiO_2 and fibers were investigated in detail to improve the self-cleaning ability of polymer concrete. In addition, the use of perlite and fibers aims to improve the physical properties of polymer concrete and make it lighter. Perlite is known for its low density and high insulating capacity, while fibers can increase the tensile strength of the concrete matrix and reduce the risk of cracking (Topçu and Işıkdağ 2008; Cojocaru et al. 2023). The combination of TiO_2, perlite and fibers aims to optimize both the functional and structural performance of the material. The focus of the research is on the effects of different TiO_2-resin-fiber ratios on the self-cleaning performance of polymer concretes. Specimens were prepared with different TiO_2/resin ratios (0%, 3%, 6%, 9%) and fiber/resin ratios (0%, 0.5%, 1%). The data obtained showed that the self-cleaning capacity improved significantly with increasing TiO_2 content; in particular, the specimens with 9% TiO_2/resin ratio showed the highest performance. These results demonstrate how careful optimization of the proportions of additives used in the development of polymer concretes can be effective in improving material performance and environmental sustainability. The results offer potential improvements for both the building materials industry and environmental protection.

2. Experimental Study

2.1. Materials

The construction materials in this study were used in a previous research and their structural characteristics were provided by Ünal and Canbaz (2024).

- Binder: Polyester type resin was used as a binder in the study. The polyester used is TP100 type of Turkuaz Polyester (Kocaeli, Türkiye) brand. Casting-type orthophthalic based unsaturated polyester resin was used as binder. The mechanical, physical and chemical properties of the polyester resin are shown in Table 1.

Hardeners are accelerators or heat-activated chemicals that regulate the curing of polyester resin. They initiate cross-linking reactions between the resin and reactive monomers. In this way, solidification of the resin is provided. Methyl ethyl ketone peroxide (Mek Peroxide) of Turkuaz Polyster was used as hardener in the experimental study.

Accelerators are used in the curing of unsaturated polyester resins with organic peroxides at room temperature. Accelerator activates the hardener and enables the reaction to start. In the experimental study, cobalt octoate from Turkuaz Polyster was used as accelerator.

Table 1. Properties of polyester resin.

Viscosity Cps	Appearance	Exothermic heat, °C	Specific weight, kg/m³	Working time, min.	Tensile str., MPa	Bending str., MPa	Hardness Barcol
350–500	Clear, liquid	175	1.17	10–15	50–60	85–95	40–42

- Fiber: Polypropylene fibers obtained from Şişecam Company (İstanbul, Türkiye) were used in the study. The chemical and physical properties of the fibers used in the blend are given in Table 2.
- TiO_2: The TiO_2 used in production is in the anatase phase and was sourced from Refsan (Kütahya, Türkiye). As the purity of the material is very high, no additional purification was required. The properties of the powders used in the initial stage, as reported by the manufacturers, are shown in Table 3.
- Perlite: Perlite obtained from Uzay Perlit Company (İstanbul, Türkiye) was used in the study. The chemical and physical properties of the fibers used in the blend are given in Table 4. The granulometry of the expanded perlite used in the study is shown in Fig. 1.

Table 2. Properties of fiber.

Fiber diameter, µm	Clipping length, mm	Moisture content, %	Type of binder	Amount of binder, %
13	4.5–6.0	0.07	Silane	0.7 ± 0.2

Table 3. Properties of TiO_2.

Phase	Average grain size, µm	Purity, %	Fineness, m²/g	Density, kg/dm³
Anatase	5	> 99	82	4.21

Table 4. Properties of perlite.

Specific weight, kg/m³	Average grain size, mm	SiO_2, %	Al_2O_3, %	Na_2O, %	K_2O, %	MgO, %	PH
50–60	0–3	74	14	3	5	0.5	7

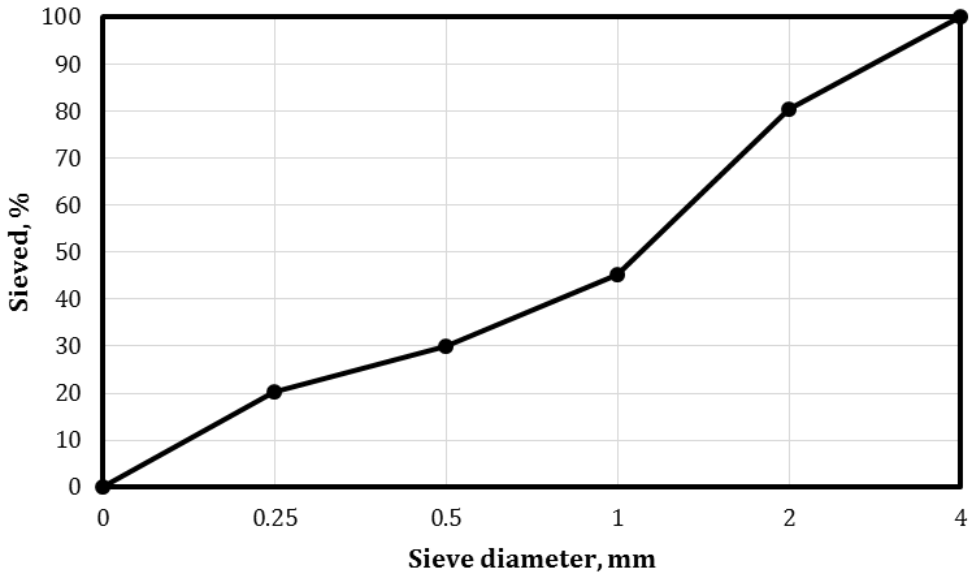

Fig. 1. Granulometry of expanded perlite used in the study.

2.2. Method and tests

The first step in specimen production was to produce control specimens. In the production stage, perlite and polyester were prepared for production in separate containers. Hardener was added to the polyester at a rate of 2% of resin and accelerator at a rate of 1%. All components were mixed until a homogeneous mixture was obtained. The mixture was poured into 4x4x16 cm metal moulds after thorough compaction to avoid voids. The surfaces of the moulds were lubricated with mould oil before casting. The mixture was allowed to set for 30-40 minutes. At the end of the setting process, the moulds were opened and the specimens were prepared for the experiment after 1 day.

For the production of the additive specimens, polyester was mixed with perlite by adding hardener and accelerator before mixing with perlite. The mixture was then poured into the container with perlite to obtain a homogeneous mixture. TiO_2 (0% - 3% - 6% - 9%) and fibers (0% - 0.5% - 1%) were then added to the mixture in different proportions to the resin and thoroughly mixed. The resulting mixture was poured into metal moulds lubricated with moulding oil and again thoroughly compacted to avoid voids. Table 5 shows the mixing ratios of the concrete specimens. Since the polymerization time can reach 7 days depending on the type of resin, the tests were carried out 7 days after production.

The photocatalytic tests were carried out according to the UNI 11259 standard. Rhodamine B dye, the preferred pollutant in this standard, is the most commonly used pollutant in photocatalytic colour tests. A solution with a concentration of 50 mg/dm^3 was prepared with Rhodamine-B powder (UNI 11259 2008). For colorimetric measurements, a spectrophotometer using the L^*a^*b (CIE) colour system (directional 65°/10° and diffuse 8°/d sphere geometry) was preferred (Ünal and Canbaz 2022). In this colour system, $\pm a$ is green-red, $\pm b$ is blue-yellow and L is lightness (Durmuş 2020; McGrath et al. 2017). In the study, measurements were taken at five different points on each sample surface and the results were averaged. Colorimetric measurements were taken at the beginning, 4 hours and 26 hours. The 4 hour and 26 hour self-cleaning performance was calculated using the formulas in Eqs. (3) and (4). The self-cleaning experiments were repeated a total of 3 times on the same surfaces of the same specimens to study the long-term effects. In this way, the loss of self-cleaning performance over long periods was also analyzed. The UNI 11259 (2008) standard requires R_4>25% after 4 hours and R_{26}>50% after 26 hours.

Table 5. Mix proportion of photocatalytic fibrous lightweight polymer concrete.

Perlite/Polyester resin	Accelerator/Polyester resin	Hardener/Polyester resin	TiO_2/Polyester resin	Fiber/Polyester resin
0.11	0.01	0.02	0/0.03/0.06/0.09	0/0.005/0.01

$$R_4 = [(a_0 - a_4)/ a_0)] \times 100 \quad (3)$$

$$R_{26} = [(a_0 - a_{26})/ a_0)] \times 100 \quad (4)$$

a_0 : Colour coordinate value a, before illumination with UV lamp
a_4 : Colour coordinate value a, after 4 hours of UV irradiation
a_{26} : Colour coordinate value a, after 26 hours of UV irradiation
R_4 : Degradation rate after 4 hours of UV irradiation
R_{26} : Degradation rate after 26 hours of UV irradiation (UNI 11259 2008)

ΔE is the colour difference in the CIELAB colour space between an object of the same size observed by a CIE standard observer in the same neutral environment. ΔE is calculated using the following Eq. (5) (Zhang and Guo 2021):

$$\Delta E = [(\Delta L)^2 + (\Delta a)^2 + (\Delta b)^2]^{1/2} \quad (5)$$

ΔE : Colour difference
ΔL : Difference between the coordinates of L
Δa : Difference between the coordinates of a
Δb : Difference between the coordinates of b

3. Discussion

3.1. Properties of fresh SCC

In the analysis of the results, the changes in the a colour coordinate, as defined in the UNI 11259 standard, were first studied. Fig. 2 shows the degradation rates obtained using Eqs. (1) and (2) as a result of colorimetric measurements on fiber-free specimens. Fig. 2 provides that the specimens with 9% TiO_2 achieved the highest colour coordinate change with 36.92% at the end of 4 hours in the first experiment. After the 9T0F specimen, the best performance was achieved by the 6T0F specimen with 6% TiO_2. Both the 6T0F and 9T0F specimens met the requirement of being above the 25% limit at the end of 4 hours as specified in the UNI 11259 standard. The 3T0F and 0T0F specimens were below the 25% limit. When analysing the self-cleaning performance after 26 hours, the 9T0F specimen reached the highest value with 66.15%. 6T0F reached 60.65% after 26 hours. Both specimens met the requirement to be above the 50% limit at the end of 26 hours, as specified in the UNI 11259 standard. Specimens 3T0F and 0T0F remained below the 50% limit after 26 hours. It can be said that 9T0F and 6T0F specimens showed self-cleaning properties in the first test.

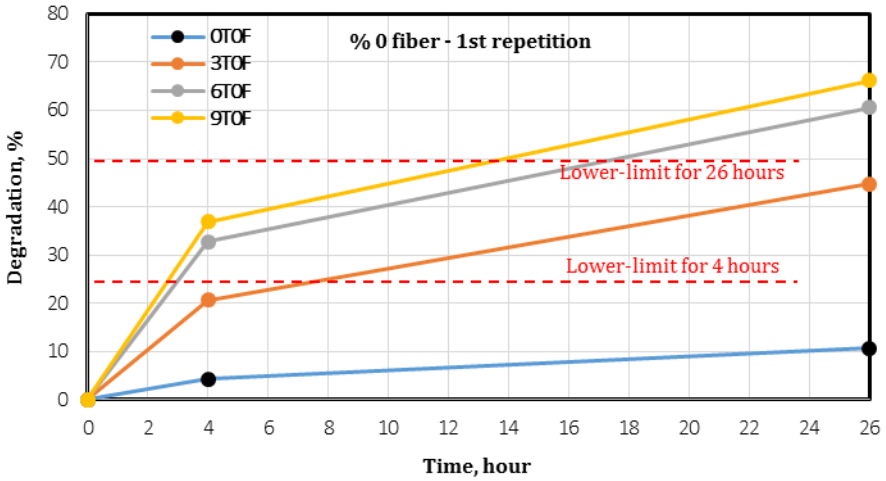

Fig. 2. Degradation of fiber-free specimens at the 1st repetition.

Fig. 3 shows the results of the 2nd and 3rd self-cleaning tests on the fiber-free specimens. The tests were carried out at 1 month intervals to examine the long term effects. Analysis of Fig. 3 shows that the 9T0F and 6T0F specimens performed very well in the repeat tests. In both repeat tests, 9T0F specimens gave the highest results. In the 3rd repeat test, the 9T0F specimen, which achieved a maximum colour coordinate change of 66.67% at the end of 26 hours, did not lose its self-cleaning performance over long periods. The 6T0F spec-imen reached a degradation rate of 60.65% after 26 hours in the first test. In the 3rd self-cleaning test, it is seen that it reached 55% at the end of 26 hours. Therefore, it can be said that the specimens containing 6% TiO_2 tend to show lower performance in the long term than the specimens containing 9% TiO_2. The control sample 0T0F without TiO_2 and fiber achieved an average degradation rate of 10% in all tests. The self-cleaning performance of the 3T0F specimens was below the UNI 11259 limits.

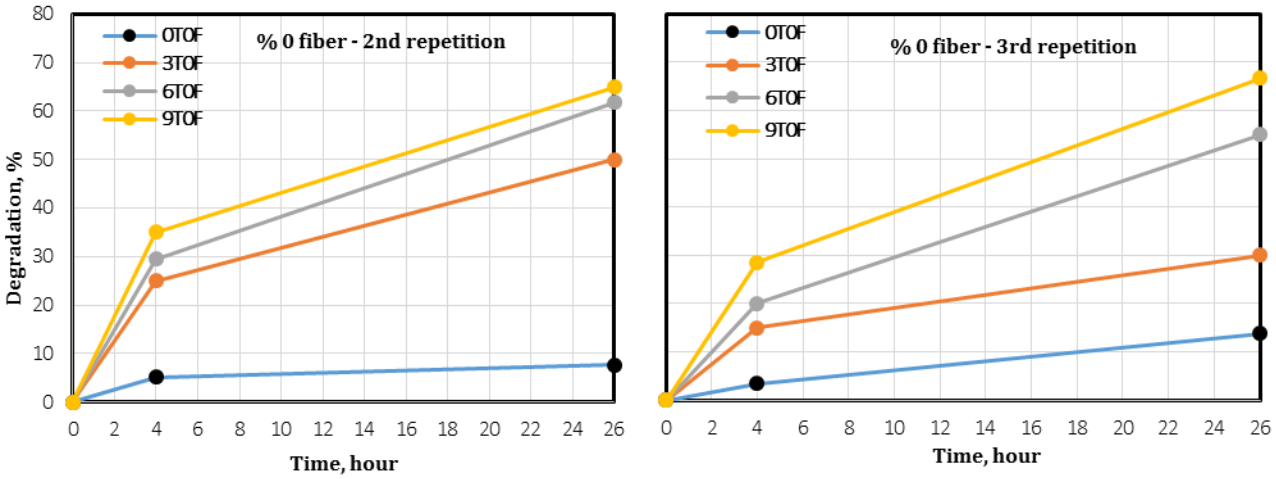

Fig. 3. Degradation of fiber-free specimens at 2nd and 3rd repetitions.

Fig. 4 shows the results of the first self-cleaning test on samples containing 0.5% fiber. Looking at the first test results, it can be seen that there is not much difference between the specimens containing 0.5% fiber and no fiber. In this case, it is clear that a small amount of fiber additive does not make a significant difference to the self-cleaning performance. As with the fiber-free samples, the specimens containing 0.5% fiber had the highest self-cleaning rate at 4 hours and 26 hours, and the specimens containing 9% TiO_2 had the highest self-cleaning rate. The 9T0.5F specimens achieved a degradation rate of 35.48% after 4 hours and 64.51% after 26 hours. With the results obtained, the 9T0.5F and 6T0.5F specimens were above the UNI 11259 limits, while the 3T0.5F and 0T0.5F specimens were below the UNI 11259 limits.

Fig. 5 shows the results of the second and third self-cleaning tests on samples containing 0.5% fiber. Looking at the results of the second test, it can be seen that there are no significant differences in values from the first test. In the second test it can be seen that the 9T0.5F specimens achieved the highest rate of degradation at the end of 4 hours and 26 hours. The 9T0.5F specimens achieved 30.43% degradation rate after 4 hours and 65.21% degradation after 26 hours. After 9T0.5F, the most effective ingredient was 6T0.5F. 6T0.5F specimens achieved

30.32% degradation rate after 4 hours and 60% degradation rate after 26 hours. The 3T0.5F and 0T0.5F specimens were below the lower limits specified in the UNI 11259 standard. 0T0.5F, which does not contain TiO_2 in its structure, reached a maximum degradation rate of 12% after 26 hours. This percentage was obtained due to the heat generated by the artificial UV source on the concrete surface. Therefore, according to the test results obtained, it can be said that the specimens without TiO_2 in their structure do not have self-cleaning properties.

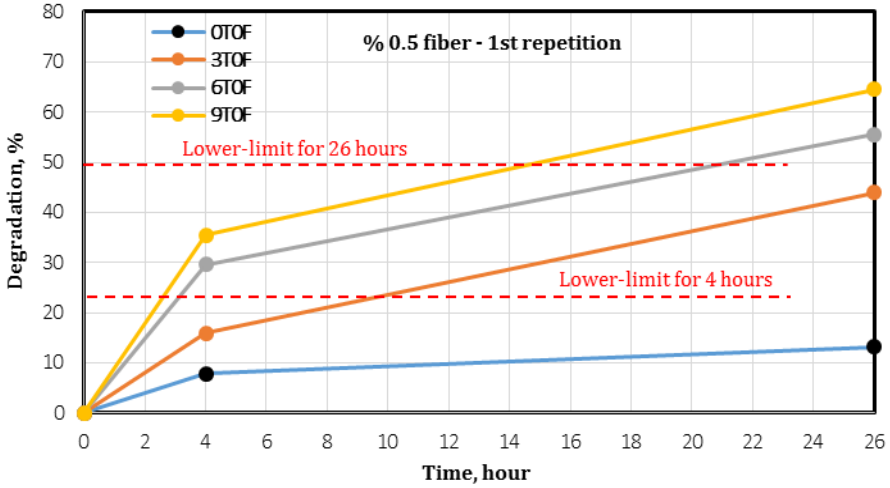

Fig. 4. Degradation of specimens containing 0.5% fiber at the 1st repetition.

When the results of the third self-cleaning test on the specimens containing 0.5% fiber are examined, the most significant difference is observed in the 6T0.5F specimen. At the end of 26 hours, the degradation rate of the 6T0.5F sample, which was 60% in the 2nd test, decreased to 50% in the 3rd test. Although the 50% degradation rate is within the UNI lower limit, it is worrying for its long-term performance. The specimens containing 9% TiO_2 did not lose performance in the long term. Another notable situation in the 3rd self-cleaning test was the 3T0.5F specimens. After 26 hours, the degradation rate of the 3T0.5F specimen, which was 41.93% in the 2nd test, decreased to 25% in the 3rd test. This shows that as the TiO_2 content decreases, the self-cleaning performance continues to decrease in the long term.

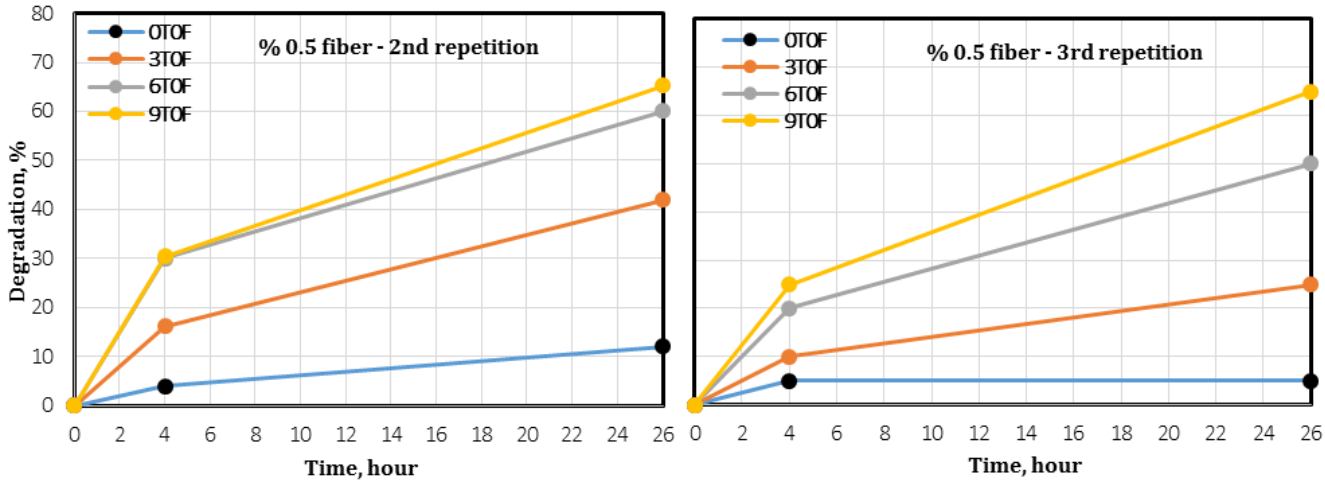

Fig. 5. Degradation of specimens containing 0.5% fiber at 2nd and 3rd repetitions.

Fig. 6 shows the first test results showing the self-cleaning performance of the specimens containing 1% fiber. As can be seen from the graph, there is a slight decrease in the self-cleaning rate as the fiber content increases. For example, 9T0F with no fiber content achieved a 66.15% degradation rate after 26 hours in the first test, while 9T1F with 1% fiber content achieved a 58.62% degradation rate after 26 hours in the first test. Fibers are not resistant to UV radiation and may show some expansion due to the temperature generated on the surface and internal structure by the light from the UV source, thus limiting the TiO_2's effective area. Nevertheless, 9T1F and 6T1F exceeded the UNI 11259 lower limit after 4 and 26 hours. 3T1F and 0T1F specimens were below the UNI limits at both 4 hours and 26 hours.

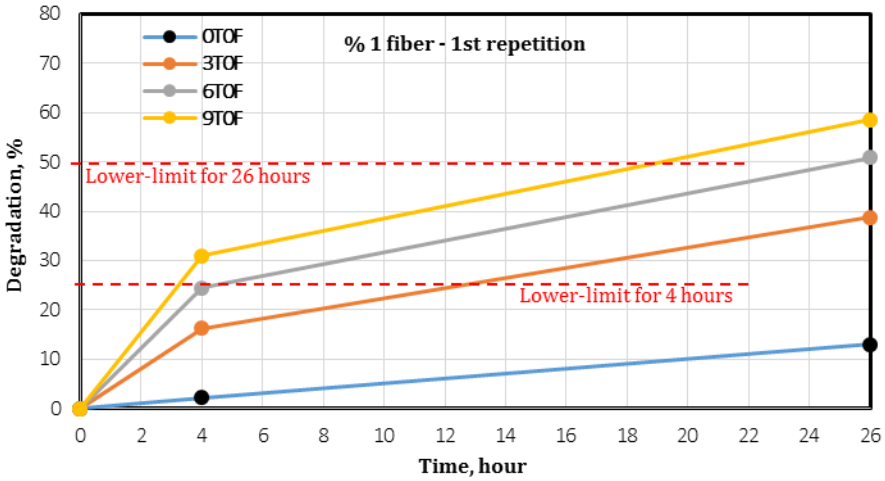

Fig. 6. Degradation of specimens containing 1% fiber at the 1st repetition.

Fig. 7 shows the second and third test results showing the self-cleaning performance of the samples containing 1% fiber. Analyzing the second test results, it can be seen that the 9T1F and 6T1F samples performed above the UNI limits at both 4 and 26 hours. In the second test, 9T1F showed the highest self-cleaning performance. While 9T1F achieved 32% degradation after 4 hours, it achieved 60% degradation after 26 hours. 6T1F achieved 28% degradation after 4 hours and 52% degradation after 26 hours. With these results, it can be said that the 1st and 2nd test results are close to each other. 3T1F and 0T1F specimens were below the UNI 11259 limits, as in the other tests.

Looking at the third test results showing the self-cleaning performance of the samples containing 1% fiber, the most remarkable performance was achieved in 6T1F. The degradation rate, which was about 25% at the end of 4 hours in the 1st and 2nd test results, decreased to 20% in the 3rd repeat test. The degradation rate, which was approximately 52% at the end of 26 hours in the 1st and 2nd test results, decreased to 40% in the 3rd repeat test. Looking at the results obtained in the 3rd test, it can be said that the 6T1F sample with 1% fiber has lost its self-cleaning ability in the long term. Looking at all the results obtained in general, it can be seen that the use of 9% TiO_2 is ideal for fibrous lightweight polymer concretes in both the short and long term. Specimen 3T1F, which does not contain TiO_2 and contains 3% TiO_2, remained below the UNI lower limits in the 3rd test. From these results it can be seen that the fibrous lightweight polymer concretes without TiO_2 and with 3% TiO_2 did not show self-cleaning properties in any of the tests.

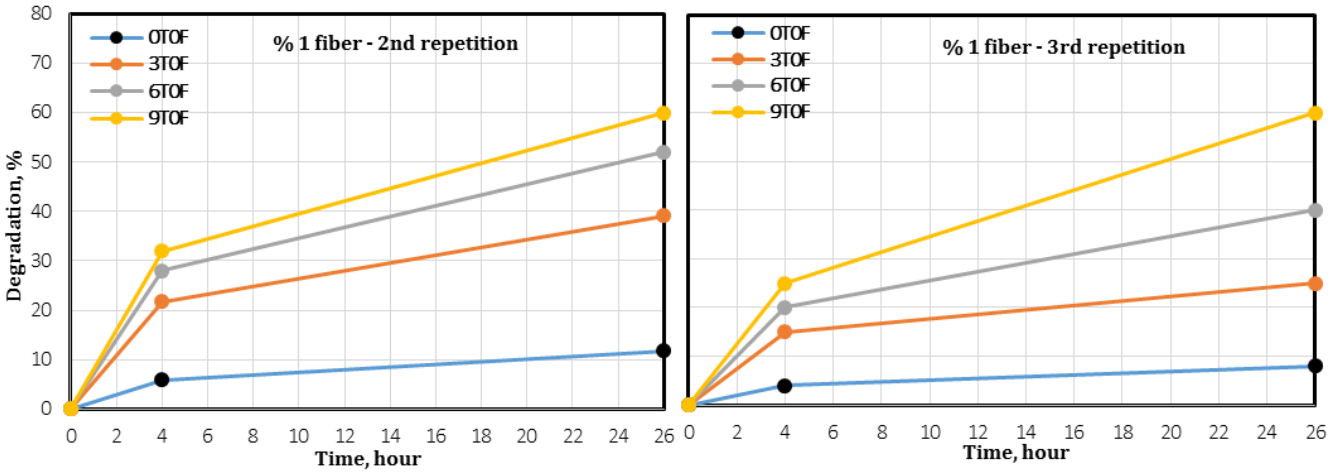

Fig. 7. Degradation of specimens containing 1% fiber at 2nd and 3rd repetitions.

Fig. 8 shows the results of the first, second and third self-cleaning tests on fiber-free specimens. The values obtained are the average of the values obtained in all the tests. The ΔE value is obtained from the changes in L, a, b coordinates using Eq. (3) and expresses the total colour change. Fig. 8 shows that 9T0F with 9% TiO_2 achieved the highest ΔE value at the end of 4 hours and 26 hours. 9T0F reached 12 at the end of 4 hours and 18 ΔE value at the end of 26 hours. The ΔE value between 0-2 indicates that there is no significant change in the colour structure. It was found that the ΔE of the 0T0F specimen without TiO_2 was also in this range. The ΔE range of the 6T0F was between 9T0F and 3T0F specimens.

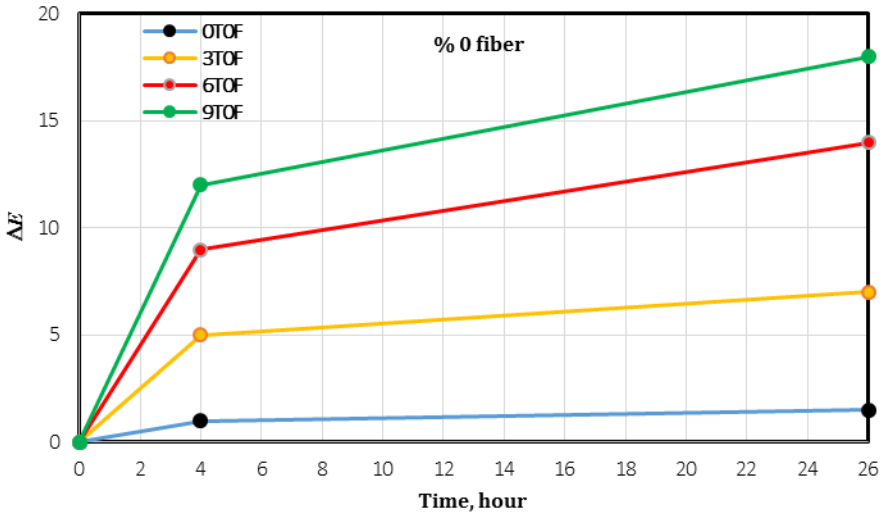

Fig. 8. Δ*E* values of fiber-free specimens.

Fig. 9 shows the results of the first, second and third self-cleaning tests on specimens containing 0.5% fiber. The values obtained are the average of the values obtained in all the tests. From Fig. 9, it can be seen that 9T0.5F with 9% TiO_2 reached the highest Δ*E* value after 4 hours and 26 hours, as in the samples without fiber. 9T0.5F reached a Δ*E* value of 13 at the end of 4 hours and 17 at the end of 26 hours. When the test results were examined, it was found that increasing the fiber content from 0% to 0.5% was not very effective in changing the Δ*E* values of the specimens. It was found that the Δ*E* of the 0T0.5F specimen without TiO_2 was within the 0-2 limit.

Fig. 10 shows the Δ*E* results of the samples containing 1% fiber. It can be seen that the specimens with the highest colour change was the specimen with 9% TiO_2. As the fiber content increased, the Δ*E* values of the specimens containing 9% TiO_2 decreased slightly. The Δ*E* values of the fiber free sample 9T0F at the end of 4 hours and 26 hours were 12 and 18 respectively. However, the Δ*E* values of 9T1F specimens with 1% fiber content were 11 and 16 respectively. The fiber structure is not resistant to UV radiation and the high coefficient of expansion slightly reduced the Δ*E* value.

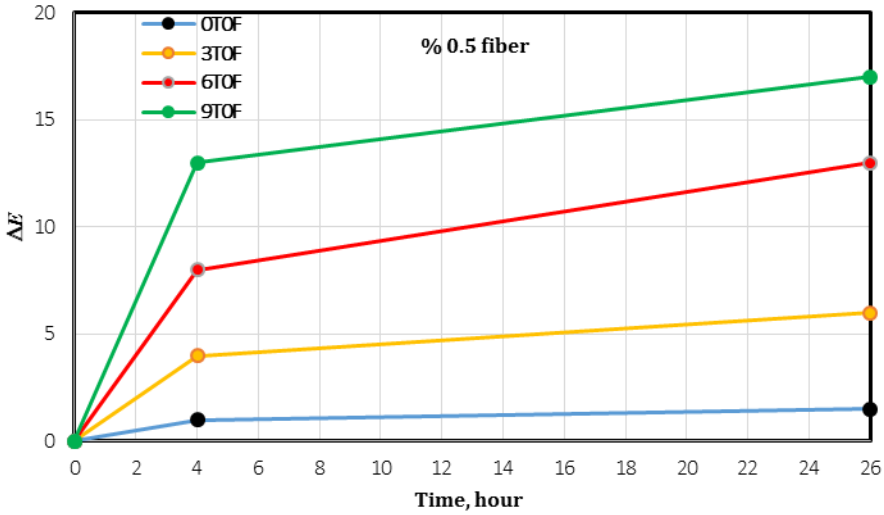

Fig. 9. *ΔE* values of specimens containing 0.5% fiber.

4. Conclusions

The conclusions of the study are summarized as:

- While increasing the fiber ratio from 0% to 0.5% did not cause any change in the *a*-coordinate in the first tests, increasing the fiber ratio to 1% caused a decrease in the *a*-coordinate change of up to 10%.
- The increase in fiber content affected the specimen which containing 3% and 6% TiO_2 most in the long term. When comparing the 3rd tests, they showed decreases of up to 15% due to the fiber increase.
- The specimens that did not show a decrease in performance in both short and long term were the specimens containing 9% TiO_2.
- When all the contents were compared, the specimens with 9% TiO_2 exceeded the limits set by the UNI 11259 standard in all the tests. The specimens with 9% TiO_2 reached the highest degradation rate of

36.92% after 4 hours and 66.67% after 26 hours. 18 ΔE value and a high colour change was obtained.

Looking at the overall results, the increase in fibre content has a slightly negative effect on the self-cleaning performance. However, considering its contribution to mechanical properties, it is recommended to use 1% fiber. It is recommended to use 9% TiO_2 in lightweight polymer concretes with photocatalytic properties to obtain permanent self-cleaning performance in short and long term. In this field, measuring the self-cleaning performance with different photocatalysts at different mixing ratios is recommended for future studies.

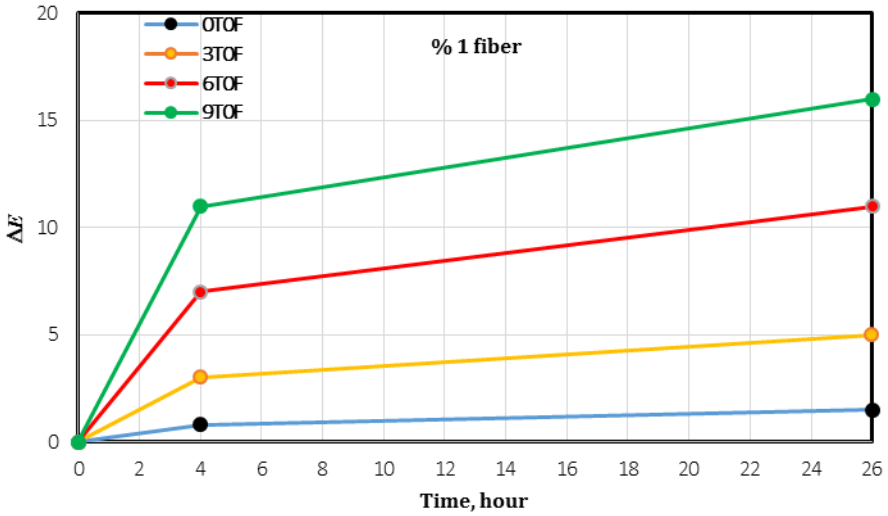

Fig. 10. ΔE values of specimens containing 1% fiber.

Acknowledgements

None declared.

Funding

The authors received no financial support for the research, authorship, and/or publication of this manuscript.

Conflict of Interest

The authors declared no potential conflicts of interest with respect to the research, authorship, and/or publication of this manuscript.

Author Contributions

All of the authors made substantial contributions to conception and design, or acquisition of data, or analysis and interpretation of data; were involved in drafting the manuscript or revising it critically for important intellectual content; and gave final approval of the version to be published.

Data Availability

The datasets created and/or analyzed during the current study are not publicly available, but are available from the corresponding author upon reasonable request.

REFERENCES

Bedi R, Chandra R, Singh SP (2013). Mechanical properties of polymer concrete. *Journal of Composites*, 2013(8), 948745.

Beeldens A (2006). An environmental friendly solution for air purification and self-cleaning effect: the application of TiO_2 as photocatalyst in concrete. *Proceedings of Transport Research Arena Europe–TRA*, Göteborg, Sweden, 1-9.

Cakir F (2022). Effect of curing time on polymer concrete strength. *Challenge Journal of Concrete Research Letters*, 13(2), 54-61.

Carp O, Huisman CL, Reller A (2004). Photoinduced reactivity of titanium dioxide. *Progress in Solid State Chemistry*, 32, 33-177.

Cedillo-González EI, Barbieri V, Falcaro P, Torres-Martínez LM, Juárez-Ramírez I, Villanova L, Siligardi C (2018). Influence of domestic and environmental weathering in the self-cleaning performance and durability of TiO_2 photocatalytic coatings. *Building and Environment*, 132, 96-103.

Cojocaru A, Isopescu DN, Maxineasa SG (2023). Perlite concrete: a review. *IOP Conference Series: Materials Science and Engineering*, 1283(1), 012003.

Ćurčić AA (2019). Photocatalytic self–cleaning facades in achitectural design. *Facta Universitatis, Series: Architecture and Civil Engineering*, 16(3), 425-436.

Dikkar H, Kapre V, Diwan A, Sekar SK (2021). Titanium dioxide as a photocatalyst to create self-cleaning concrete. *Materials Today: Proceedings*, 45, 4058-4062.

Folli A, Pade C, Hansen TB, De Marco T, Macphee DE (2012). TiO_2 photocatalysis in cementitious systems: Insights into self-cleaning and depollution chemistry. *Cement and Concrete Research*, 42(3), 539-548.

Guo Q, Zhou C, Ma Z, Yang X (2019). Fundamentals of TiO_2 photocatalysis: concepts, mechanisms, and challenges. *Advanced Materials*, 31(50), 1901997.

Güler E (2024). The effect of dust sugar filter waste on soil dynamic parameters and liquefaction. *Journal of Material Cycles and Waste Management*, 26(4), 1-19.

Haider AJ, Jameel ZN, Al-Hussaini IH (2019). Review on: Titanium dioxide applications. *Energy Procedia*, 157, 17-29.

Hashimoto K, Irie H, Fujishima A (2005). TiO_2 photocatalysis: a historical overview and future prospects. *Japanese Journal of Applied Physics*, 44(12R), 8269.

Khan SA, Hussain F, Khushnood RA, Amjad H, Ahmad F (2024). Feasibility study of expanded clay aggregate lightweight concrete for nonstructural applications. *Advances in Civil Engineering*, 2024(1), 8263261.

Kiruthika C, Prabha SL, Neelamegam M (2021). Different aspects of polyester polymer concrete for sustainable construction. *Materials Today: Proceedings*, 43, 1622-1625.

Nodehi M (2022). Epoxy, polyester and vinyl ester based polymer concrete: a review. *Innovative Infrastructure Solutions*, 7(1), 64.

Sarde B, Patil YD (2019). Recent research status on polymer composite used in concrete-an overview. *Materials Today: Proceedings*, 18, 3780-3790.

Rebeiz KS, Serhal SP, Craft AP (2004). Properties of polymer concrete using fly ash. *Journal of Materials in Civil Engineering*, 16(1), 15-19.

Seymour H (2019). The Multinational Construction Industry. Taylor & Francis, Routledge.

Sui Pheng L, Shing Hou L, Pheng LS, Hou LS (2019). The economy and the construction industry: A study at the firm level. In: *Construction Quality and the Economy*, Springer Nature, 21-54.

Şengel H, Kınık K, Erol H, Canbaz M (2022). Effect of waste steel tire wired concrete on the mechanical behavior under impact loading. *Challenge Journal of Structural Mechanics*, 8(4), 150-158.

Thienel KC, Haller T, Beuntner N (2020). Lightweight concrete–From basics to innovations. *Materials*, 13(5), 1120.

Topçu İB, Işıkdağ B (2008). Effect of expanded perlite aggregate on the properties of lightweight concrete. *Journal of Materials Processing Technology*, 204(1-3), 34-38.

Ulu A (2024). Effect of resin amount on the damping properties of polymer concrete. *Challenge Journal of Concrete Research Letters*, 15(2), 47-55.

Ünal S, Canbaz M (2022). Effect of industrial wastes on self-cleaning properties of concrete containing anatase-TiO_2. *Revista de la Construcción*, 21(3), 493-505.

Ünal S, Canbaz M (2024). Mechanical properties of lightweight photocatalytic marbelite. *Challenge Journal of Structural Mechanics*, 10(4), 159-165.

Zailan SN, Mahmed N, Abdullah MMAB, Sandu AV, Shahedan NF (2017). Review on characterization and mechanical performance of self-cleaning concrete. *MATEC Web of Conferences*, 97, 01022.

Zhang S, Guo Y (2021). Measurement of gem colour using a computer vision system: A case study with jadeite-jade. *Minerals*, 11(8), 791.

Zhao A, Yang J, Yang EH (2015). Self-cleaning engineered cementitious composites. *Cement and Concrete Composites*, 64, 74-83.

Challenge Journal of Concrete Research Letters

Research Article

Flowability and compressive strength of ternary blended cement mortar of coal bottom ash and ground cockle shell ash

Nabilla Mohamad [a], Rahimah Embong [a], Nor Hazurina Othman [b], Khairunisa Muthusamy [a,*], Mohd Faizal Md Jaafar [a]

[a] *Faculty of Civil Engineering Technology, Universiti Malaysia Pahang Al-Sultan Abdullah, 26300 Kuantan, Pahang, Malaysia*
[b] *Faculty of Civil Engineering and Built Environment, Universiti Tun Hussein Onn Malaysia, 86400 Batu Pahat, Johor, Malaysia*

ABSTRACT

Flourishing cement industry to meet the demand of construction industry has negative impact to the global environment owing to the carbon emission during calcination of cement. At the same time, the disposal of coal bottom ash and cockle shell from coal power plant and cockle trade which pollutes the environment also need to be resolved. In view of circular economy, the present research aims to produce ternary blended cement consisting of coal bottom ash (CBA) and cockle shell ash (CSA) for sustainable mortar production. The research was conducted to determine the effect of CBA as partial cement replacement on flowability and compressive strength of CSA blended cement mortar. Seven mortar mixes consisting of CBA as supplementary cementitious material ranging from 0% to 60% by weight of cement were prepared. All specimens were water cured up to 56 days. The flowability test was conducted to assess the properties of the fresh state, while hardened properties were evaluated through compressive strength test at 1, 3, 7, 28, and 56 days. The results showed flowability decreased by 5% to 31% with increasing CBA content compared to the control mix. The use finer sized CBA forms a slightly stickier mortar mix with lower flowability. A combination 10% to 20% CBA is the best percentage to use for formation of CSA mortar with enhanced strength. However, a maximum strength of 23 MPa was achieved at 56 days with an optimal CBA replacement of 10%. This research demonstrates the potential by transforming industrial waste for low-carbon cement production to save the use of landfills for waste disposal and optimize consumption of non-renewable resources.

ARTICLE INFO

Article history:
Received – July 31, 2024
Revision requested – September 13, 2024
Revision received – November 30, 2024
Accepted – December 16, 2024

Keywords:
Coal bottom ash
Cockle shell waste
Cement replacement
Sustainable construction
Cleaner environment

Citation: Mohamad N, Embong R, Othman NH, Muthusamy K, Jaafar MFM (2025). Flowability and compressive strength of ternary blended cement mortar of coal bottom ash and ground cockle shell ash. *Challenge Journal of Concrete Research Letters*, 16(1), 25–32.

1. Introduction

The most popular material used in building and infrastructure construction is concrete, a mixture made mostly of aggregates, water, and binder (Shanks et al. 2019). The advantageous attributes of the concrete in terms of flexibility, robustness, sustainability, and low-cost has led it to be used globally (Singh et al. 2020). Concrete is used in all types of building construction. The increase in the use of concrete as main building material due to expanding population demand also results in a flourishing cement manufacturing trade. Production of cement is increasing by 2.5% per year and it is anticipated to be between 3.7 and 4.4 Gt by 2050 (Akashi et al. 2011). About 60% of global CO_2 emissions is from cement industry (Scrivener et al. 2018). On overall, concrete industry is accountable for roughly 10% of worldwide industrial CO2 emissions, which contribute to climate change (Amin et al. 2019; Adesina 2020). Realizing that cement is increasingly used owing to its role as a

* *Corresponding author*. Tel.: +60-9-431-5014 ; E-mail address: khairunisa@umpsa.edu.my (K. Muthusamy)
ISSN: 2548-0928 / DOI: https://doi.org/10.20528/cjcrl.2025.01.003

sole binder in the famously utilized concrete worldwide, unearthing new alternate material would decrease the reliance on cement and benefits the environment. Thus, investigating alternatives that use materials with a lower carbon footprint and can replace Portland cement in this regard is crucial to promote cleaner industry. Inclusion of by-product from industrial activity as a filler or pozzolanic material in concrete has thus been the subject of extensive research in recent years. A variety of waste have been investigated its use as an alternative binder in concrete such as fly ash, slag, palm oil fuel ash, rice husk ash, oyster shell ash, cockle shell ash and many more. However, as the cement consumption continue to rise, more alternative materials need to be discovered to produce low carbon cement and also to reduce reliance on the consumption of natural resource. In view of circular economy, recycling the waste from any industries for product development would benefits the environment and decrease use of landfill space for disposal purpose.

The increasing for energy from various industries has resulted in larger quantity of coal used in coal power plants. Fly ash and coal bottom ash (CBA) are by-products generated at plant which disposed as environmental polluting waste. From the whole coal ash, approximately 10 to 20% of is comprised of CBA (Argiz et al. 2017). CBA is among the largest form of industrial wastes generated by coal-fired thermal power plants (Baite et al. 2016). Due to rapid development, the quantity of solid wastes generated from coal-fired power plants every year continues to increase (Ramzi Hannan et al. 2020). This, in turn, produces a large volume of CBA which is disposed of as wastes. The dumping of this waste poses negative effect to the environment (Muthusamy et al. 2018). Dumping of this waste contaminates the soil and reduces the quality of air as well as water (Singh et al. 2022) which affect the living things. The existence SiO_2 and Al_2O_3 in CBA has enabled it to possess pozzolanic activity (Basirun, et al. 2017; Menéndez et al. 2021) which makes it suitable candidate for cement replacement. The beneficial effect of CBA when used at the right proportion which results in concrete strength increment owing to pozzolanic reaction that creates denser internal structure makes more exploration were carried out to reveal its potential. Investigation has been conducted on the use of CBA as partial cement replacement in concrete (Argiz et al. 2017), high strength concrete (Khongpermgoson et al. 2020) and geopolymer concrete (Ping et al. 2022). Nevertheless, the application of CBA in construction material production needs to be increased to reduce waste dumping at landfill.

In the Southeast Asian region, cockles (Anadara granosa), which live primarily on intertidal mudflats, are an essential protein source. It is one type of sea mollusc an widely consumed in various delicacies in Southeast Asian countries. Worldwide mollusk production (16 million tons) accounts for approximately 22% of global aquaculture growth (Food & Agriculture Organization 2016). A cockle is an edible, marine bivalve mollusk. Bivalve shellfish are very common in marine species (Eziefula et al. 2018). According to Shellfish Association of Great Britain (2012), cockles are a low-calorie food. A total of 100 g of cockles contains only 53 kcal compared to 180 kcal in 100 g of salmon (Shellfish Association of Great Britain 2012). Blood cockles are a common source of protein for Southeast Asian coastal communities, such as Malaysia, Singapore, Thailand and Indonesia (Mirsadeghi et al. 2011). Consumer demand for shellfish and other seafood has led to a considerable expansion in their aquaculture in fresh, brackish, and marine areas, with a total production of 73.8 million metric tons and an estimated value of USD 160 billion in 2014 (Food & Agriculture Organization 2016). This included 16.1 million metric ton of mollusks composed of 104 species valued at USD 19 billion (Food & Agriculture Organization 2016). In addition, according to Food & Agriculture Organisation (2017), the world production of cockles in 2017 was 535k tons which slightly decreased from the year 2016 with 561k tons. Meanwhile, the Department of Fisheries Malaysia (2011) reported that 57,544 tons of cockles had been harvested in the past decade along the Peninsular Malaysia's west coast. . The cockle's shell has a very high content of calcium. It is generally composed of calcium carbonate of prismatic layers (Lertwattanaruk et al. 2012; Mohamed et al. 2012). The calcium carbonate, $CaCO_3$, accounts for higher than 90% of the weight in the cockle shell (Jatto et al. 2010; Martínez-García et al. 2017; Mo et al. 2016; Mohamed et al. 2012; Olivia et al. 2015, 2017; Safi et al. 2015). It is almost equal to limestone (Othman et al. 2018; Soltanzadeh et al. 2018).

In order to alleviate this waste from being dumped, researchers have explored the potential use of CBA combined with OPC producing binary blended cement-based concrete (Argiz et al. 2017; Muthusamy et al. 2024) and high strength concrete (Khongpermgoson et al. 2020) However, research on the integration of CBA as partial cement replacement with other types of cement replacement material in ternary blended cement remain to be investigated. The effect of CBA as partial cement replacement combined with cockle shell ash on the flowability, compressive strength and microstructure of cement-based composite remains unanswered. Thus, the present research investigated the effect of integrating CBA as partial cement replacement on the flowability, compressive strength and microstructure. CBA used in this research were collected from power plant. Then it was ground before it is blended as cement replacement CBA ranging from 0% to 60% in mortar mixes. A total of seven mortar mixture were subjected to flowability test and compressive strength test. The use of cockle shell and CBA as partial cement replacements would contribute towards formation of sustainable concrete and helps in reducing waste disposal issues.

2. Methodology

2.1. Materials

Ordinary Portland cement (OPC), fine aggregate, coal bottom ash (CBA), cockle shell ash (CSA) and water were used in this research work. Local river sand passing sieve 1.18 mm were used as fine aggregate. CBA which was obtained from one of the coal power plant were

ground to be fine powder. Cockle shells were collected from the dumping area in a fishing village in Peninsula Malaysia were washed thoroughly using flowing water to remove the mud and dirt before it is dried. Then, the shells were calcined at 650°C using furnace and ground utilizing grinding machine until it trans-formed into fine powder using the processing steps reported by Mohamad et al (2024). In this research, the particle size of CBA and CSA is similar to that of OPC particles with an average size of 45 μm, which is targeted to improve performance in cementitious applications. Both ground CBA and CSA were subjected to wet sieve test to ensure the ashes passes the limit of wet sieve result stated ASTM C618 (2019). Fig. 1 illustrates the CBA and CSA used in this research. The oxide content of the binders is tabulated in Table 1.

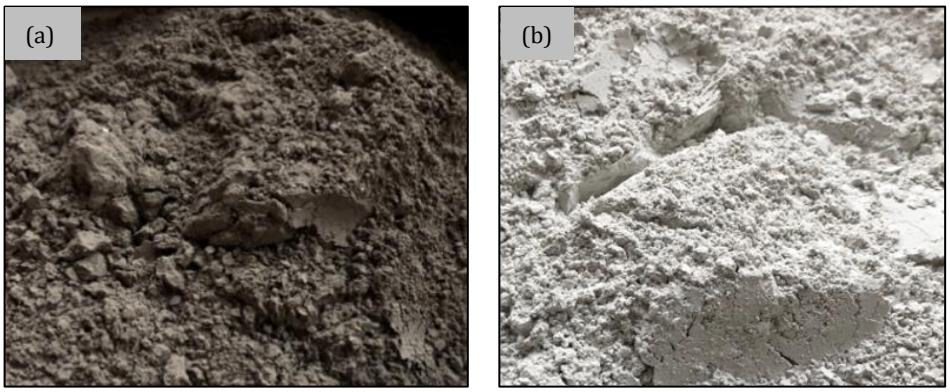

Fig. 1. Binder used: (a) Coal bottom ash; (b) Cockle shell ash.

Table 1. Oxide composition of binders.

Oxide	OPC	CSA	CBA
SiO_2	18.84	0.39	60.14
Al_2O_3	5.39	0.18	19.30
Fe_2O_3	3.79	2.54	13.56
MgO	0.03	0.01	0.04
Na_2O	0.10	0.94	–
K_2O	0.30	0.02	1.19
SO_3	3.06	0.13	0.42
CaO	62.21	93.50	3.56
LOI	3.94	3.97	2.30

2.2. Mix proportion and specimen preparation

Seven mixes of blended cement were used to produce mortar. Mix produced using 10% cockle shell ash (CSA) and 90% identified as CA10, were utilized as control specimen (CA10). A control mix with 100% OPC was not included in this research work, as the focus was to evaluate the effect of a combination of 10% cockle shell ash and various levels of coal bottom ash (CBA) replacement on mortar performance. The contribution of 10% CSA as cement replacement towards strength increment of mortar as compared to other replacement has been reported by Mohamad (2023). Other six mixes were prepared by integrating 10% CSA with CBA ranging from 0% to 60%. Details of the mixes used is shown in Table 2. Preparation of mortar mixture were done using clean apparatus. All ingredient were accurately weighed and mixed homogenously before filled in the oiled mould. Proper compactions were done, and the specimen were left overnight. The next day, the hardened mixes were removed from the mould, labelled and immersed in water for curing until the testing days.

2.3. Testing

The flowability test was carried out using flow table in accordance to ASTM C1437-07 (2007). Earlier, flow table would be ensured to be in damp condition and clean before placing a flow mold in the middle. The mold was then filled in three layers with the mixture. Each layer was compressed with 20 tamping rod strokes. After compacting the top layer, a sawing motion was used to move the stuffing rod to strike the mortar surface. Following that, the mold was removed 60 seconds after the compaction activity was performed and the table was dropped 25 times. Finally, the diameter of the mortar spread was measured along the four-boundary line on the tabletop. The compressive strength test was done in accordance with ASTM C109 (2016). During the testing, the mortar specimen was placed in the testing machine below the center of the upper bearing block. Then, the load rate at a relative rate of movement between the upper and lower platens was applied to specimen faces that were in contact with the true plane surfaces of the mold. The internal structure of hardened mortar mixes was observed through Field emission scanning electron microscopy (FESEM) testing using equipment shown in Fig. 2 which was conducted at Centre of Excellence for Advanced Research in Fluid Flow (CARIFF), UMPSA. The sample was dried and ground to a powdered form. It was then placed on the aluminum stubs using adhesive carbon tape and followed by platinum coating to increase conductivity to prevent charging problems. The stub was then placed into the vacuum chamber of the instrument. The surface morphology obtained by using magnification ranging from 500x to 25,000x times.

Table 2. Mix proportion (kg/m^3).

Mix	Cement	Sand	Cockle shell ash	Coal bottom ash	Water content
CA10	180	600	20	–	0.70
CABA10	160	600	20	20	0.70
CABA20	140	600	20	40	0.70
CABA30	120	600	20	60	0.70
CABA40	100	600	20	80	0.70
CABA50	80	600	20	100	0.70
CABA60	60	600	20	120	0.70

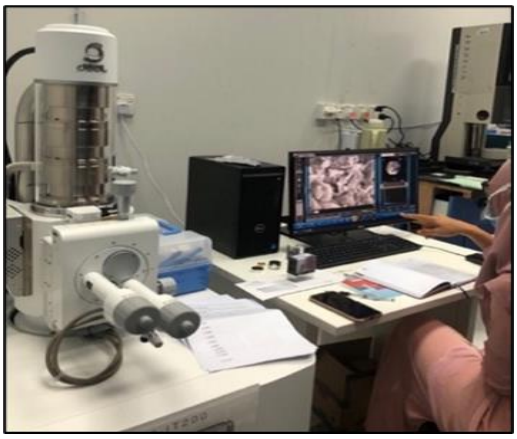

Fig. 2. FESEM testing apparatus.

3. Results and Discussion

3.1. Flowability

The flowability of mortar mixes consisting blend of 10% CSA and varying percentage of CBA is shown in Fig. 3. The control mixture (10% CSA and 0% CBA) revealed an optimal flowability value of about 105%. The introduction of CSA appears to provide good workability characteristics. However, it clearly shows that the flowability values of CSA mortar incorporating different level of CBA replacement labeled as CABA10, CABA20, CABA30, CABA40, CABA50 and CABA60 was found to be 104%, 101%, 93%, 86%, 82% and 73%, respectively. A decrease in flowability is evident when the replacement of CBA in CSA mortar is increased from 10% to 60%. CSA mortar with higher amount of CBA (60% CBA) demonstrate the lowest flowability value of 73%. This reduction can be attributed to CBA's characteristic properties like porous nature of CBA itself that increases water absorption. It can be observed that integration of CBA forms a stickier mixture which reduce the flow dispersion. The rate of flowability reduction ranged from 5% to 31% when compared to the control mix. Flowability value declines as larger percentage of this industrial ash is used. It can be suggested that higher content of CBA, may require an adjustment of water content or the addition of a superplasticizer. The flow spread of CSA mortar with 10% CBA and 60% CBA is illustrated in Fig. 4. The use of the smaller size of CBA with a BET surface area of 22800 cm^2/g as compared to OPC of 5700 cm^2/g resulted in a lower flowability value. The use of finer ash requires a larger amount of water to cover its surface reduced the flowability. The effect of using smaller sized particle towards increased water requirement to coat the bigger surface area has been pointed out by Neville and Brooks (2010).

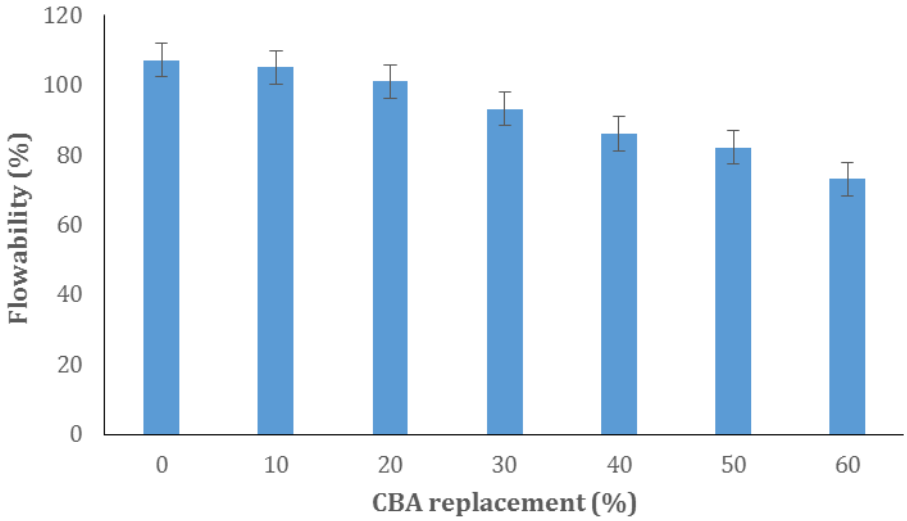

Fig. 3. Flowability test results.

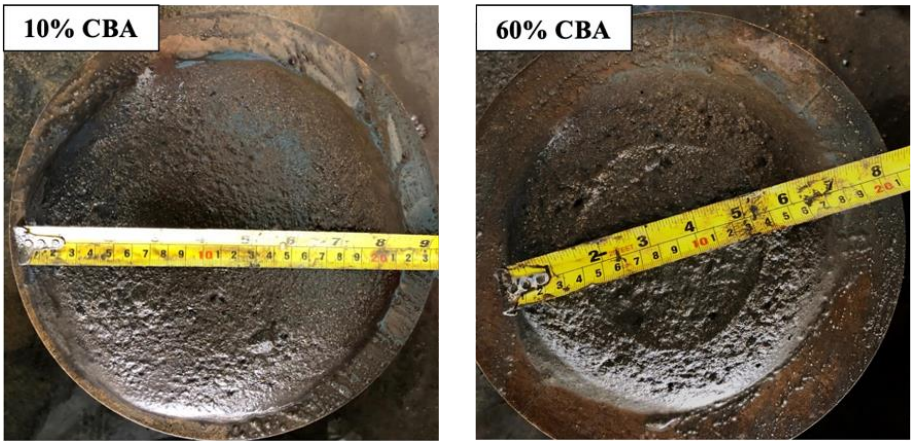

Fig. 4. Effect of CBA content on spread of mortar mixture.

3.2. Compressive strength

The compressive strength of mixes with ternary blended cement cockle shell ash (CSA) and coal bottom ash (CBA) is illustrated in Fig. 5. At day 1, the strength of 10% CSA mortar ranged from 12.40 MPa (0% CBA) to 1.24 MPa (60% CBA replacement). At 3 days, the strength increased to 16.52 MPa to 2.27, followed by 16.75 MPa to 3.23 MPa at 7 days of curing. It is evidently shows that higher proportion of CBA (20% to 60%) reflected significantly lesser compressive strength compared to the control mix and combination with 10% CBA. This happens because of the slow pozzolanic reaction experienced by CBA. Since CBA contains pozzolanic activity, it requires calcium hydroxide (CH) from cement hydration, which is lacking in the early stages of curing leading to a slower formation of C-S-H gel for strength development. By 28 days, the obtained strength was significantly developed between 20.34 MPa to 7.43 MPa. The increase in strength observed for the mixture containing 10%CBA surpassing that of the control mix. It can be attributed to the optimal pozzolanic reaction that appears at this level of replacement. Previous studies also found that the strength of mortar with pozzolanic materials increases over time with optimal performance noted at specific replacement levels (Sakthivel and Suthaviji 2024; Kang et al. 2024; Pinheiro et al. 2024). On the other hand, the finer particle size of CBA (22800 cm^2/g BET surface area) compared to OPC (5700 cm^2/g) helps fill voids in the mortar, reducing porosity and increasing strength. Therefore, prolonged the age of curing has provided the filler action and pozzolanic reaction simultaneously (Chen et al. 2022; Al Biajawi et al. 2024). The maximum strength was reached at 56 days, ranging from 23.12 MPa for control mix to 10.57 MPa for 60% CBA replacement. The maximum strength was reached at 56 days of curing, ranging from 23.12 MPa for control mixture to 10.57 MPa for the 60% CBA replacement. The results show that as the age increases, the strength of all mixes continues to improve due to prolonged hydration and pozzolanic activity. In this stage, the CSA mortar samples with 10% CBA consistently present excellent compressive strength as compared to control mix. It was also found that mortar samples containing 0%, 10% and 20% exceeded the threshold of 20 MPa as shown in Fig. 5, however, a series of CSA mortar mixes significant strength reduction beyond 30% CBA. Therefore, the mix with 10% CBA confirmed the optimal replacement level in the production of 10% CSA mortar but limited the CBA replacement to 20% for acceptable strength development.

Overall, the results show positive strength development with prolonged curing time, indicating increased C-S-H gel formation. This is due to chemical reactions of the binders benefitting from the continuous presence of water for all mixes. The strength of mixes consisting of CBA remains slightly lower because of late pozzolanic reaction which is commonly observed in other types of mortar blended with pozzolanic ash. However, mix with 10% CBA exhibits the highest strength value amongst all mixes after cured for 28 days owing to pozzolanic reaction. Presence of moisture at all time with the blend of right amount of CBA has enabled better hydration process and pozzolanic reaction contributing to formation of binding gel which is crucial for strength of cement-based material. The augmentation of cement-based composites mechanical properties is achievable via enhanced pozzolanic effect and filler role of the pozzolanic material (Isaia et al. 2003). Nevertheless, the overuse of CBA poses adverse effect to the strength achievement due to extreme reduction in cement use that lowers the hydration process with lesser CSH gel and calcium hydroxide formed. As a result, the ample supply of silicon dioxide from CBA unable to form secondary C-S-H gel owing to the limited availability of CBA. The strength declination of cement-based composite resulting from high usage of pozzolanic ash has been reported by Masazza (1993). As a comparison, the denser internal structure of mix with 10% CBA with lesser voids in contrast to mix with 60% CBA content with high number of voids is shown in Fig. 6. The image shows that CABA10 sample containing 10% CSA and 10% CBA shows a denser microstructure, and the voids are smaller and more compact. In contrast, CABA60 sample that incorporating 60% CBA showed a more porous microstructure, looser compaction and larger gaps in the voids. It is proven that CABA10 provides a better particle packing, it improves the filling effect and boost the strength enhancement. Evidently, this finding corroborated with the previous studies (Singh et al. 2021; Alosta et al. 2024).

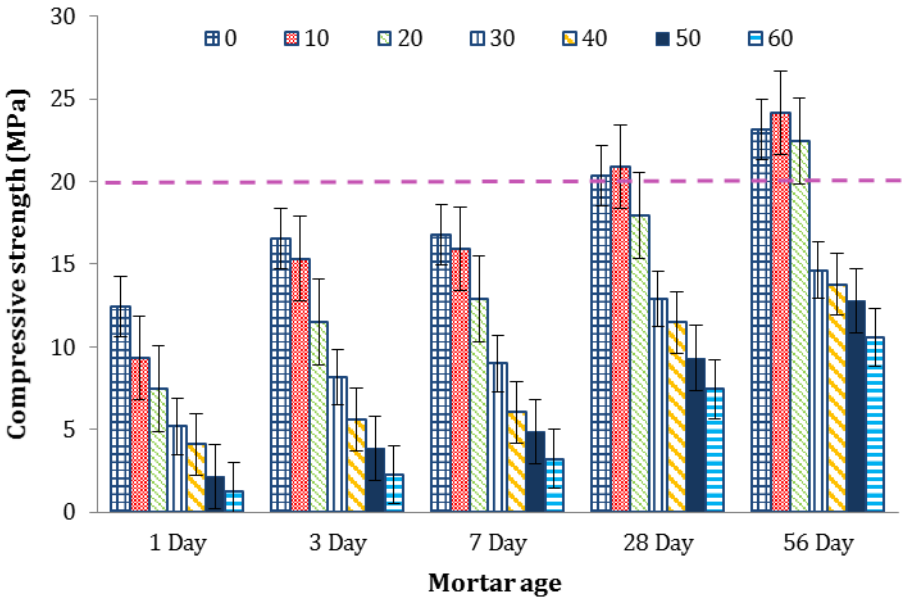

Fig. 5. Compressive strength result of mortar mixes.

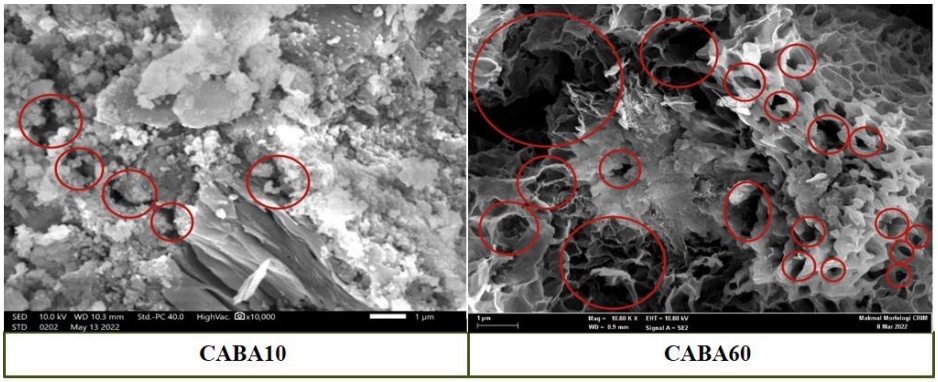

Fig. 6. Morphology of mortar with 10% and 60% CBA with high number of voids.

4. Conclusions

The introduction of coal bottom ash (CBA) in the cockle shell ash (CSA) mortar mixes have significant effect on both fresh and hardened properties. It was observed that flowability continued to decrease with increasing CBA content from 0% to 60%, where the reduction in flowability values ranged from 5% to 31% of that of the control mix. This decrease in workability does not appear to have a large effect on strength development. The results show that the ideal CBA replacement is around 10% to 20% to balance the need between flowability and strength requirements. However, blending 10% CBA contributes towards strength increment through pozzolanic reaction that forms compact microstructure of the cement-based material. Microstructural images also revealed that 10% CBA produce a more compact (denser) and filling effect that directly correlates with strength performance. Excessive use of CBA needs to be avoided as it results in weaker mortar. Ternary blended cement formed of CSA and CBA supports the idea of reducing waste disposal to the environment and optimization on the use of natural resources for cement production. Approach of producing low carbon construction material support implementation of sustainable construction for achieving SDG 11 (Sustainable Cities and Communities).

Acknowledgements

None declared.

Funding

This research was supported by Universiti Malaysia Pahang Al-Sultan Abdullah from under grant number RDU223006.

Conflict of Interest

The authors declared no potential conflicts of interest with respect to the research, authorship, and/or publication of this manuscript.

Author Contributions

All of the authors made substantial contributions to conception and design, or acquisition of data, or analysis and interpretation of data; were involved in drafting the manuscript or revising it critically for important intellectual content; and gave final approval of the version to be published.

Data Availability

The datasets created and/or analyzed during the current study are not publicly available, but are available from the corresponding author upon reasonable request.

REFERENCES

Adesina A (2020). Recent advances in the concrete industry to reduce its carbon dioxide emissions. *Environmental Challenges*, 1, 100004.

Akashi O, Hanaoka T, Matsuoka Y, Kainuma M (2011). A projection for global CO_2 emissions from the industrial sector through 2030 based on activity level and technology changes. *Energy*, 36, 1855–1867.

Al Biajawi MI, Embong R, Kusbiantoro A, Aljabbar HA (2024). Influences of various particle sizes of coal bottom ash as supplementary cementitious material on the pozzolanic properties. In: *Abd. Aziz R, Ismail Z, Iqbal AKMA, Ahmed I (eds). Intelligent Manufacturing and Mechatronics. iM3F 2023*. Springer Proceedings in Materials, vol 40. Springer, Singapore.

Alosta M, Mamdouh A, Al Mufargi H, Abd, Aziz FNA, Rashid A, Elbasir OMM, Al Dughaishi H (2024). Properties and microstructure of treated coal bottom ash as cement concrete replacement. *Civil Engineering Journal*, 10(4), 1125–1144.

Amin MN, Murtaza T, Shahzada K, Khan K, Adil M (2019) Pozzolanic potential and mechanical performance of wheat straw ash incorporated sustainable concrete. *Sustainability*, 11, 1–20.

Argiz C, Sanjuán MÁ, Menéndez E (2017). Coal bottom ash for Portland cement production. *Advances in Materials Science and Engineering*, 2017, 068286.

ASTM C109/C109M-16a (2016). Standard test method for compressive strength of hydraulic cement mortars (using 2-in. or [50-mm] cube specimens). ASTM International, West Conshohocken, PA.

ASTM C1437-07 (2007). Standard test method for flow of hydraulic cement mortar. ASTM International, West Conshohocken, PA.

Baite E, Messan A, Hannawi K, Tsobnang F, Prince W (2016). Physical and transfer properties of mortar containing coal bottom ash aggregates from Tefereyre (Niger). *Construction and Building Materials*, 125, 919–926.

Basirun NF, Wan Ibrahim MH, Jamaludin N, Putra Jaya R (2017). A review: The effect of grinded coal bottom ash on concrete. *MATEC Web of Conferences, International Symposium on Civil Environmental Engineering 2016,* 103, 01007.

Chen Z, Wei J, Yi C, Bindiganavile V, Li S, Li T (2022). Strength and chloride resistance of mortars blended with SCBA: the effect of calcination and particle sizing on its pozzolanic activity. *Journal of Materials Research and Technology*, 22, 1423–1435.

Department of Fisheries Malaysia (2011). Jadual Pendaratan Marin. https://www.dof.gov.my/en/ [accessed 1-6-2024].

Eziefula UG, Ezeh JC, Eziefula BI (2018). Properties of seashell aggregate concrete: a review. *Construction and Building Materials*, 192, 287–300.

Food & Agriculture Organization (2016). FAO Fisheries Statistics 2016. https://www.fao.org/fishery/static/Yearbook/YB2016_USBcard/index.htm [accessed 1-6-2024].

Isaia GC, Gastaldini ALG, Moraes R (2003). Physical and pozzolanic action of mineral additions on the mechanical strength of high-performance concrete. *Cement & Concrete Composites*, 25, 69–76.

Jatto E, Imohimi A, Medjor W, Jatto OE, Asia IO, Medjor WE (2010). Proximate and mineral composition of different species of snail shell. *The Pacific Journal of Science and Technology*, 11(1), 416–419.

Kang M-C, Ju S, Oh T, Yoo D-Y, Pyo S (2024). Novel treatment method of coal bottom ash for strain-hardening alkali-activated composite. *Cement and Concrete Composites*, 151, 105598.

Khongpermgoson P, Boonlao K, Ananthanet N, Thitithananon T, Jaturapitakkul C, Tangchirapat W, Ban CC (2020). The mechanical properties and heat development behavior of high strength concrete containing high fineness coal bottom ash as a pozzolanic binder. *Construction and Building Materials*, 253, 119239.

Lertwattanaruk P, Makul N, Siripattarapravat C (2012). Utilization of ground waste seashells in cement mortars for masonry and plastering. *Journal of Environmental Management*, 111, 133–141.

Liew JJ, Cheah CB, Kevin KLP, Siddique R, Tangchirapat W (2024). Blended cement and mortar with various low-calcium ground coal bottom ash content: Engineering characteristics, embodied carbon and cost analysis, *Construction and Building Materials*, 425, 135987.

Martínez-García C, González-Fonteboa B, Martínez-Abella F, Carro-López D (2017). Performance of mussel shell as aggregate in plain concrete. *Construction and Building Materials*, 139, 570–583.

Menéndez E, Argiz C, Sanjuán MÁ (2021). Reactivity of ground coal bottom ash to be used in Portland cement. *J – Multidisciplinary Scientific Journal*, 4(3), 223–232.

Mirsadeghi SA, Zakaria MP, Yap CK, Shahbazi A (2011). Risk assessment for the daily intake of polycyclic aromatic hydrocarbons from the ingestion of cockle (Anadara granosa) and exposure to contaminated water and sediments along the west coast of Peninsular Malaysia. *Journal of Environmental Sciences*, 23(2), 336–345.

Mo KH, Chin TS, Alengaram UJ, Jumaat MZ (2016). Material and structural properties of waste-oil palm shell concrete incorporating ground granulated blast-furnace slag reinforced with low-volume steel fibres. *Journal of Cleaner Production*, 133, 414–426.

Mohamad N (2023). Strength properties and acid resistance performance of mortar and concrete using blended cockle shell ash and coal bottom ash. *M.Sc. thesis*, Universiti Malaysia Pahang Al-Sultan Abdullah, Pahang, Malaysia.

Mohamad N, Muthusamy K, Razelan ISM, Budiea AMA, Ismail AH (2024). Effect of ground cockle shell ash as partial cement replacement on compressive strength of mortar. *AIP Conference Proceedings*, 3014, 030004.

Mohamed M, Yousuf S, Maitra S (2012). Decomposition study of calcium carbonate in cockle shell. *Journal of Engineering Science and Technology*, 7(1), 1–10.

Muthusamy K, Mohamad Hafizuddin R, Mat Yahaya F, Sulaiman M A, Syed Mohsin SM, Tukimat NN, Omar R, Chin SC (2018).Compressive strength performance of OPS lightweight aggregate concrete containing coal bottom ash as partial fine aggregate replacement. *IOP Conference Series: Materials Science and Engineering,* 342, 012099.

Muthusamy K, Wong WH, Mohamad N, Rajan J, Budiea AMA, Abdul Majeed APP, Kırgız, MS (2024). Properties of concrete containing coal bottom ash as hydraulic binder substitution. In: *Advance Upcycling of By-products in Binder and Binder-Based Materials*. Woodhead Publishing Series in Civil and Structural Engineering, 243–250.

Neville AM, Brooks JJ (2010). Concrete Technology. 2nd edition, Pearson Education Ltd., London.

Olivia M, Mifshella AA, Darmayanti L (2015). Mechanical properties of seashell concrete. *Procedia Engineering*, 125, 760–764.

Olivia M, Oktaviani R, Ismeddiyanto (2017). Properties of concrete containing ground waste cockle and clam seashells. *Procedia Engineering*, 171, 658–663.

Othman NH, Abu Bakar BH, Mat Don M, Megat Johari MA (2018). Cockle shell ash replacement for cement and filler in concrete. *Malaysian Journal of Civil Engineering*, 25(2), 201–211.

Ping KKL, Cheah CB, Siddique R, Tangchirapat W, Megat Johari MA (2022). Coal bottom ash as constituent binder and aggregate replacement in cementitious and geopolymer composites: a review. *Journal of Building Engineering*, 52, 104369.

Pinheiro VD, Abreu RFd, Alexandre J, Xavier GdC, Marvila MT, de Azevedo ARG (2024). Pozzolanic potential of calcined clays at medium temperature as supplementary cementitious material. *Sustainability*, 16(17), 7508–7508.

Ramzi Hannan NIR, Shahidan S, Ali N, Bunnori NM, Mohd Zuki SS, Wan Ibrahim MH (2020). Acoustic and non-acoustic performance of coal bottom ash concrete as sound absorber for wall concrete. *Case Studies in Construction Materials*, 13, e00399.

Safi B, Saidi M, Daoui A, Bellal A, Mechekak A, Toumi K (2015). The use of seashells as a fine aggregate (by sand substitution) in self-compacting mortar (SCM). *Construction and Building Materials*, 78, 430–438.

Sakthivel T, Suthaviji S (2024). Strength and durability studies on concrete using cashew nut shell ash (CNSA) waste as supplementary materials. *Global NEST Journal*, 26(7), 05994.

Scrivener KL, John VM, Gartner EM (2018). Eco-efficient cements: Potential economically viable solutions for a low-CO2 cement-based materials industry, *Cement Concrete Research*, 114, 2–26.

Shanks W, Dunant CF, Drewniok MP, Lupton RC, Serrenho A, Allwood JM (2019). How much cement can we do without? Lessons from cement material flows in the UK. *Resources Conservation Recycling*, 141, 441–454.

Shellfish Association of Great Britain (2012). The nutritional and healthy facts about shellfish. https://www.shellfish.org.uk/files/Healthy-Eating/32571SAGB%20cockles%20fact-sheet%20final%20lo-res.pdf [accessed 1-6-2024].

Singh N, Nassar R, Shehnazdeep K, Anjani B (2021). Microstructural characteristics and carbonation resistance of coal bottom ash based concrete mixtures. *Magazine of Concrete Research*, 74(7), 364–378.

Singh N, Haque MM, Gupta A (2022). Reviewing mechanical performance of geopolymer concrete containing coal bottom ash. *Materials Today: Proceedings,* 65(2), 1449–1458.

Soltanzadeh F, Emam-Jomeh M, Edalat-Behbahani A, Soltan-Zadeh Z (2018). Development and characterization of blended cements containing seashell powder. *Construction and Building Materials*, 161, 292–304.

Challenge Journal of Concrete Research Letters

Research Article

Mechanical and durability study of nano-SiO_2 and nano-TiO_2 on fiber reinforced concrete

Awadhesh Srivastava [a,*], Abhishek Mishra [a], Sachin Kumar Singh [a]

[a] *Department of Civil Engineering, Institute of Engineering and Technology, Lucknow, 226021 Uttar Pradesh, India*

ABSTRACT

This work presents the results of an experimental investigation into the strength and durability properties of fiber-reinforced concretes that have polypropylene (PP) fibers added to the concrete by volume and nano-SiO_2 (silicon dioxide) and nano-TiO_2 (titanium dioxide) used as partial substitutes for cement. Nano-SiO_2 and nano-TiO_2 particles used ranged in size from 40 nm to 400 nm. The specimens were cast using cement blended nano-SiO_2 and nano-TiO_2 percentages of 1%, 2%, 3%, and 4% by weight of cement. M55 grade concrete was employed for the casting process. The addition of PP fibers to the concrete was 0.5% by volume. The specimens underwent a battery of mechanical tests, including microstructural testing, compression testing, split tensile strength testing, and rupture modulus testing. Furthermore, tests for durability factors such as porosity, sorptivity, and degradation were conducted, and the findings are presented. Flexural strength of 2% nano-SiO_2 or nano-TiO_2 increased by 8.09% and 6.89% and porosity decreased by 16.13% and 13.92% with respect to the reference concrete. By comparing the outcomes, it was shown that the inclusion of 0.5% PP fibers and 2% nano-SiO_2 or nano-TiO_2 improved the mechanical qualities, but this was followed by a decrease in strength. The findings demonstrated that 2% nano-SiO_2 combined with 0.5% PP fiber had a greater mechanical strength than 2% nano-TiO_2.

ARTICLE INFO

Article history:
Received – November 14, 2024
Revision requested – December 18, 2024
Revision received – December 21, 2024
Accepted – December 30, 2024

Keywords:
Compressive strength
Silicon dioxide
Titanium dioxide
Porosity
Sorptivity

Citation: Srivastava A, Mishra A, Singh SK (2025). Mechanical and durability study of nano TiO_2 and nano SiO_2 on fiber reinforced concrete. *Challenge Journal of Concrete Research Letters*, 16(1), 33–39.

1. Introduction

Concrete is the most often used construction material worldwide due to its reasonable cost and durability. One of the primary ingredients of concrete, cement, produces significant CO_2 emissions during its production –roughly two billion tons annually, or about 7% of all CO_2 emissions on Earth– during the process (Shi et al. 2011). It is projected that cement production will have grown to over six billion tons per year by 2060. (Pacheco-Torgal et al. 2013). Severe measures have been implemented to reduce the harmful effects of cement on the environment and climate change. There have been a lot of experiments done on finding cement substitutes, like adding pozzolanas and nanoparticles. It would be more accurate to refer to nanoparticles as recently developed concrete additives. Because of their strong reactivity and large area of coverage, nanoparticles are generally employed in cement-based materials not only as additives but also as a substitute for cement to improve certain mechanical and durability-related properties. Over the past ten years, nanotechnology has garnered a lot of attention (Reches 2018; Kim et al. 2015). The use of nanoparticles in cement-based materials has been the subject of much research since their inception. Given their physical impacts (filling and nucleation effects) and chemical reactivity, nanoparticles are known to significantly improve the performance of cement-based materials (Murad 2021; Feng et al. 2023; Luo et al. 2023). For usage in cement-based materials, nano-SiO_2, nano-Al_2O_3, nano-

* *Corresponding author*. E-mail address: kumarawadhesh0011@gmail.com (A. Srivastava)
ISSN: 2548-0928 / DOI: https://doi.org/10.20528/cjcrl.2025.01.004

TiO_2, nano-$CaCO_3$, nano-Fe_2O_3, and nanotubes have all been investigated. Among them, nano-SiO_2 and nano-$CaCO_3$ are frequently employed. This is because nano-SiO_2 can perform better because to its high specific area and pozzolanic activity, while nano-$CaCO_3$ is very inexpensive because it is readily available in limestone, chalk, and marble. The addition of nano- and micro limestone shortened the setting time of ultra-high-performance concrete (UHPC), according to this study's investigation of the material's early age properties (Karthikeyan et al. 2020; Karthikeyan and Dhinakaran 2018; Mohseni et al. 2016). Additionally, compared to a sample without any nano limestone, the inclusion of 2.5% to 5% nano-limestone may result in a 35%–74% boost in first day compressive strength. This study looked into how adding 3% nano-SiO_2 to the mass of cementation materials sped up the hardening process and improved the mechanical qualities of UHPC (Yoo et al. 2022; Hakeem et al. 2022; Marcos-Meson et al. 2020). This study looked into how nano-SiO_2 enhanced compressive strength and decreased UHPC workability, particularly at early stage. While nano-$CaCO_3$ and nano-SiO_2 have the potential to enhance mechanical qualities, their hydration tactics and hardening process are different. Although it is widely acknowledged that adding mineral admixtures, either conventional or nanosized, to concrete increases its strength, numerous researchers have also noted that concrete becomes more brittle as its strength rises (Khotbehsara et al. 2018; Sharmila et al. 2016). The researchers identified inadequate binding and low tensile strength as the causes of this brittleness. Fibers can be added to concrete to aid with the problem of reduced tensile strength. It is widely known that fibers increase the energy absorption capacity of concrete, making it more ductile and resistant to fatigue and impact loads. Numerous studies utilizing fibers in concrete have been conducted; among them, further reports are available for fibers such polymer, carbon, and steel. The impact resistance of concrete containing silica fume and polypropylene fiber—which was added in increments of 0.0%, 0.2%, 0.3%, 0.4% and 0.5% was examined in this study. According to the authors, adding 0.5% of fiber increased the impact resistance. Using silica fume as an additional cementitious material, this study conducted experimental investigations using various fibers and combinations in a high strength concrete mix (Sharmila et al. 2016). While previous studies have focused on single nano material with most commonly steel fiber, our study is the first to investigate the effect of nano material such as nano silica and nano titanium dioxide with polypropylene fiber providing new insights into nanotechnology in concrete. Additionally, we employed different tests to know the optimum percentage of nanomaterials which gives best results in the field of concrete technology. The authors employed a total fiber volume fraction of 1% by volume of concrete using both steel and polypropylene fibers separately as well as in a combination of 0.85% steel and 0.15% polypropylene. According to reports, the combined use of polypropylene and steel performed better than either substance utilized alone. The purpose of this work was to conduct a mechanical, durability and microstructural analysis of ultra-high-performance concrete modified with the addition of nanoparticles. Nano-SiO_2 and nano-TiO_2 used in this research as a nano material with a percentage of 1%, 2%, 3% and 4% as a replacement of cement. In addition, to improve the ductile properties, polypropylene fibers were added with a weight percentage of 0.5% of volume of concrete.

2. Experimental Investigation

2.1. Materials

Ordinary Portland Cement (OPC 53 grade) was used in this study, confirming as per IS code 4031 (1996). Natural coarse aggregate and natural river sand (fine aggregate) was used in this study. All required test of aggregate as per the IS 383 (2016) and IS 2386 (1963). In this study nano-SiO_2 and nano-TiO_2 used size range from 40-300 nm provided from Delhi distributers. Polypropylene fiber (PP fiber) of length 12mm used in this research work provided from Kalyani fiber distributer. To gain required flowability Fosroc Conplast SP 430 superplasticizer was used. All experimental test data are showed in Table 1.

Table 1. Experimental test data of materials.

Designation	Results	IS codes
W/C ratio	0.33	-
Cement type	OPC 53	-
Initial setting time of cement	40 min	IS 4031:1988
Final setting time of cement	382 min	
Specific gravity of cement	3.01	
Specific gravity of fine aggregate	2.64	IS 383:2016 & IS 2386:1963
Specific gravity of coarse aggregate	2.77	
Coarse aggregate water absorption	0.5	
Fine aggregate water absorption	0.9	
Fine aggregate zone	Zone II	

2.2. Mix proportion

High strength concrete of grade M55 used in this study. Mix proportion ratio 1:1.27:2.52 arrived as per the IS 10262 (2019). Total of 9 mix were constructed such as C1, CS1, CS2, CS3, CS4, CT1, CT2, CT3 and CT4. C1 represented the reference concrete, CS1, CS2, CS3 and CS4 represented the 1%, 2%, 3% and 4% nano-SiO_2 along with 0.5% PP fiber, and CT1, CT2, CT3 and CT4 represented the 1%, 2%, 3% and 4% nano-TiO_2 along with 0.5% PP fiber.

The mixing procedures followed as first dry mixing of nano materials and cement with fibers, after dry mixing all ingredients mixed properly in the drum mixer for 2 to 3 min. Table 2 represented the mix proportion of all concrete mix.

Table 2. Mix proportion data (kg/m^3).

Mix ID	C1	CS1	CS2	CS3	CS4	CT1	CT2	CT3	CT4
Cement	477.96	473.18	468.40	463.62	458.85	473.18	468.40	463.62	458.85
Nano-SiO_2 or Nano-TiO_2	0.00	4.78	9.56	14.34	19.12	4.78	9.56	14.34	19.12
PP fiber	0.5% of concrete volume								
FA	611.40								
CA	1212.50								
Water	169.21								
SP	1% by weight of cement								

2.3. Testing methods as per standard

The Indian standard code IS 516 (2021) was followed when performing the compressive, split, and flexural tests. Table 3 shows all of the experimental tests, codal provisions, and specimen kinds that were used in the testing. A specimen's impact resistance can be determined using a variety of techniques, including the drop weight method, instrumented impact, and explosive impact. Many researchers favor the drop weight method over other impact resistance testing techniques because of its ease of use.

Table 3. Test types and IS codes.

Tests	Property	IS codes	Specimen type and size
Strength	Compressive strength	IS 516:2021	Cubes (150x150x150mm)
	Split tensile strength		Cylinders (100x200mm)
	Flexural test		Beams (150x150x700mm)
Chloride attack	Degradation	BS 1881	Cubes (150x150x150mm)
Sorptivity	Water absorption	BS 1881-122	Cubes (150x150x150mm)
Porosity	Volume of pores	-	Cylinders (100x200mm)
Scanning electron microscope (SEM)	Microstructural study	-	Shards of samples

3. Results and Discussion

3.1. Compressive and split tensile strength

Fig. 1 represents the test results of the compressive strength test. CS2 has shown maximum compressive strength above all the mix proportions. CT4 registered a lowest compressive strength in all the mixes. All the concrete mix proportion passed the mean target strength of the concrete and CT4 was minimum. When nano-SiO_2 used in the concrete mix, CS1 and CS2 increased load gradually but after 2% of nano-SiO_2 strength reduces gradually up to CS4. When nano-TiO_2 was used in the concrete mix, strength increased gradually from CT1 to CT2 but after that strength start decreasing. CS2 compressive strength is 0.76% more than CT4 and 3.48% more than C1.

3.2. Split tensile strength

Larger percentage variation of nano materials cannot increase strength because of the less quantity of cement, which degrade the bindings properties of the concrete and nano materials might be react with other minerals (Karthikeyan et al. 2020; Karthikeyan and Dhinakaran 2018). Fig. 2 represents the tensile strength of the concrete. As PP fiber used in the concrete mix, all concrete mix proportion strength in-

creased from a target strength, but above all CS2 concrete mix showed higher strength. Larger amount of nano material not much affected on the split tensile strength properties on the concrete. Split tensile strengths of CS2 and CT2 were higher than C1 about 9.93% and 5.31% respectively.

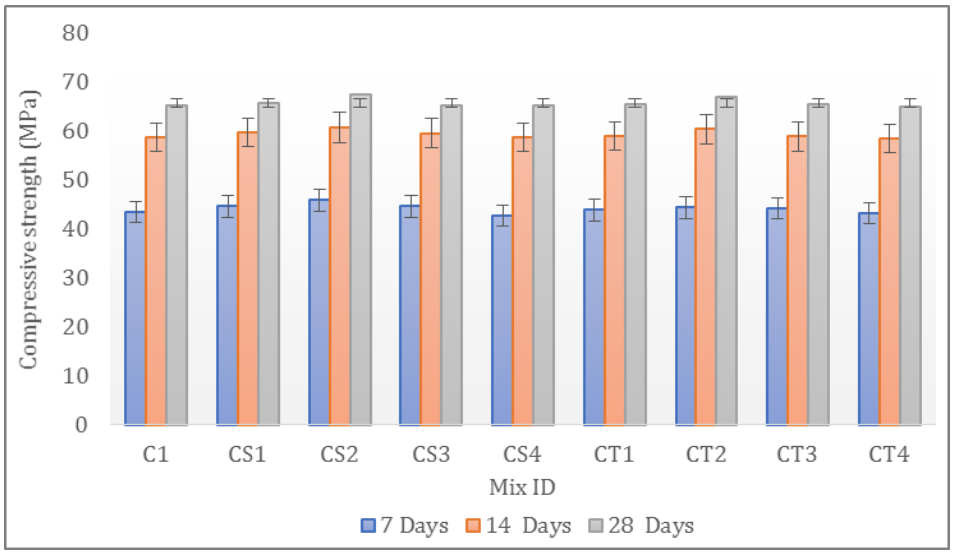

Fig. 1. Compressive strength of the concrete mix at 7, 14 and 28 days.

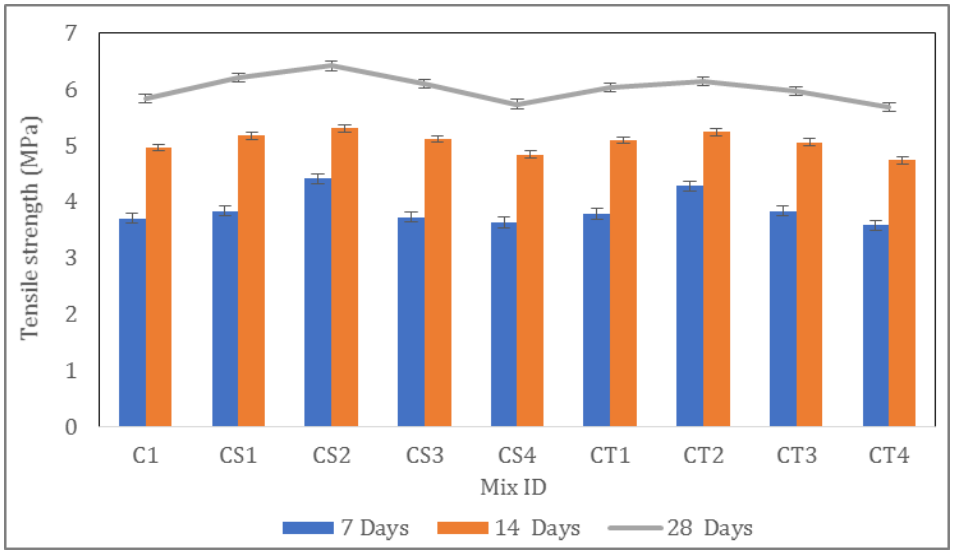

Fig. 2. Split tensile strength of the concrete mix at 7, 14 and 28 days.

3.3. Flexural strength

Fig. 3 represents the flexural strength of the concrete mixes. Flexural strength does not show the higher variation between the concrete mixes. PP fiber works as a reinforcement for the concrete specimens. PP fiber reduces the effects of brittle failures and makes a higher bond between the concrete ingredients and the fiber. CS2 and CT2 flexural strength increased by 8.09% and 6.89% respectively than C1.

3.4. Deterioration of concrete mixes

The elements that originate in the wet atmosphere, such as SO_2, damage specimens exposed to acidic environments. More importantly, the sulphur compounds that are present cause more deterioration because they react with C_3A and calcium hydroxide to form calcium sulphur aluminate, or ettringite, or $CaSO_4$. Because both of these compounds typically occupy a larger volume than their parent compounds, they disrupt the concrete and cause it to become weak and porous. Concrete mixes with 0.5% PP fiber show a higher compressive strength for all the mixes along with flexural and split tensile strength. According to the data, specimens exposed to bases often show a lower percentage of deterioration than specimens exposed to acids (Son et al. 2023; Chithra et al. 2016; Rong et al. 2015; Razak et al. 2004). The rationale for this is that cement's calcium hydroxide can react with salts or other bases to generate aragonite, brucite, and gypsum. They can impede additional infiltration of the salt water and serve as a transient barrier or protective layer.

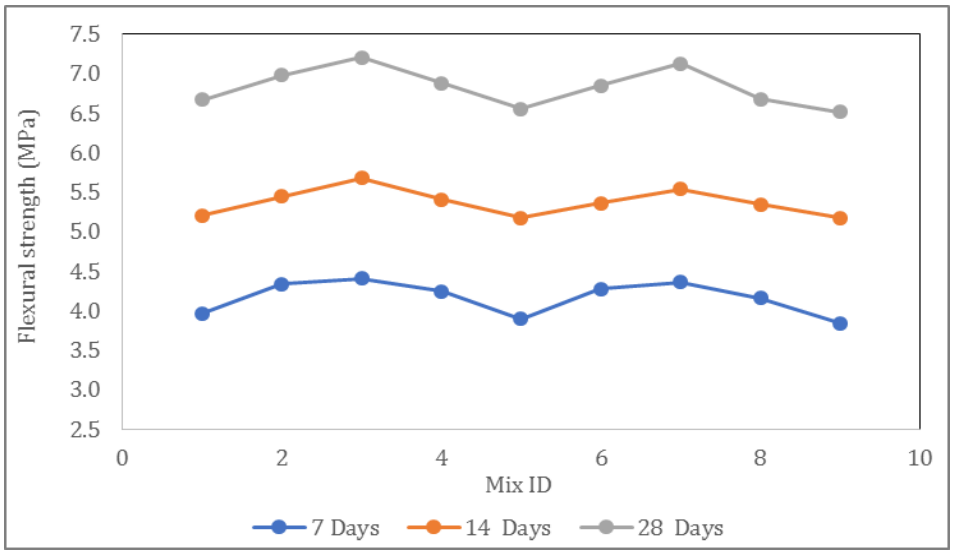

Fig. 3. Flexural strength of the concrete mix at 7, 14 and 28 days.

3.5. Sorptivity

Fig. 4 depicts the water absorption of the concrete mixes. CS2 and CT2 have less water absorption than C1 about 20% and 18.01% respectively. All the concrete mixes of water absorption lie below the 5%. When cement was replaced with nano-SiO_2 and nano-TiO_2 with 0.5% PP fiber, the water absorption gradually decreased up to 2% and then increased. It was discovered that increasing the amount of ultra-fine mineral additives had no effect on the durability characteristics. In the experimental study of Razak et al. (2013), it was found that using silica fumes as a mineral admixture could result in water absorption of 2.9% and 4.8%. Karthikeyan and Dhinakaran (2018) also noted that specimens containing 9.5% silica fume, 0.5% UFTiO_2, and 0.5% steel fiber showed water absorption of less than 1.5%.

3.6. Porosity

Fig. 5 represents the porosity value of all the concrete mixes. C1, CS4 and CT4 concrete mixes showed the higher porosity than the all-other concrete mixes. CS2 and CT2 were about 16.13% and 13.92% less than the C1.

Fig. 4. Sorptivity of the concrete mix.

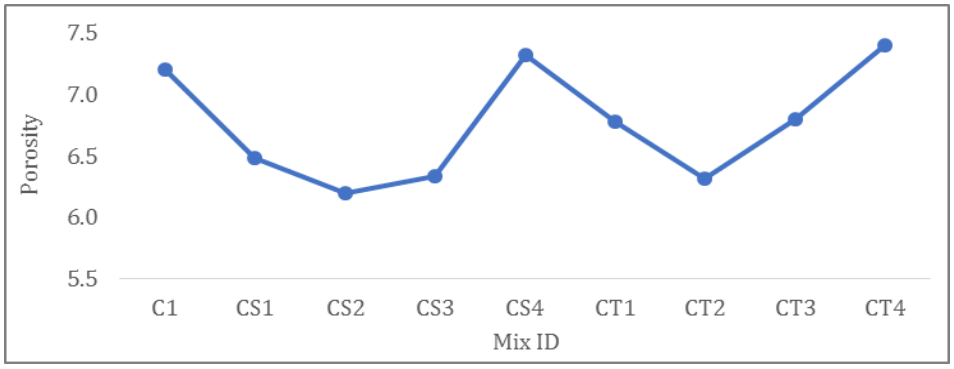

Fig. 5. Porosity of concrete mix.

Using nanoparticles of ZrO_2, SnO_2, and $CaCO_3$ in varying dosages along with fly ash, conducted experimental investigations to study the durability characteristics of self-compacting cement mortars and reported that use of the nanoparticles improved the durability properties, diminishing the porosity and chloride permeability. In their experimental efforts. This study revealed that the sorptivity characteristics of high strength concrete were improved by employing ultra-fine GGBS (Kim et al. 2015; Feng et al. 2023; Karthikeyan and Dhinakaran 2018).

3.7. Microstructural imaging

Scanning Electron Microscope (SEM) image of CS2 and CT2 are shown in the Figs. 6 and 7. In Fig. 6, incorporation of nano silica along with PP fiber shows the higher dense structure so as a results in higher mechanical strength and durability with less water absorption and porosity. While clearly observing the SEM image, it shows the less voids and proper bonding between all the ingredients. CS2 shows the higher compressive as well as flexural and split tensile strength. Fig. 7 shows the incorporation of nano-TiO_2 along with the PP fiber, TiO_2 provided a self-cleaning property to the concrete and reduces the pollution due to the CO_2, SO_2 and NO_x. SEM image of clearly shows that, very less voids available in the CT2 mix compared to C1. CS2 have less voids compared to the CT2.

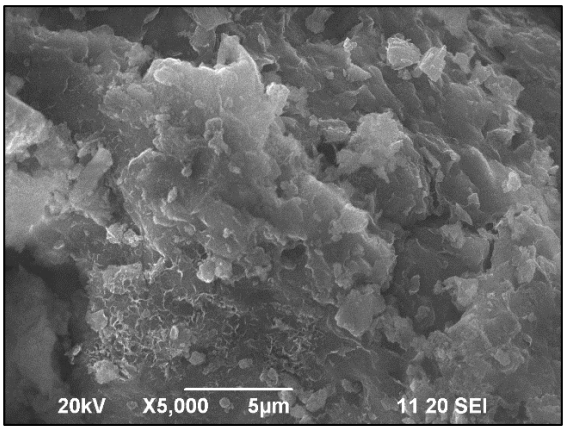

Fig. 6. SEM image of CS2.

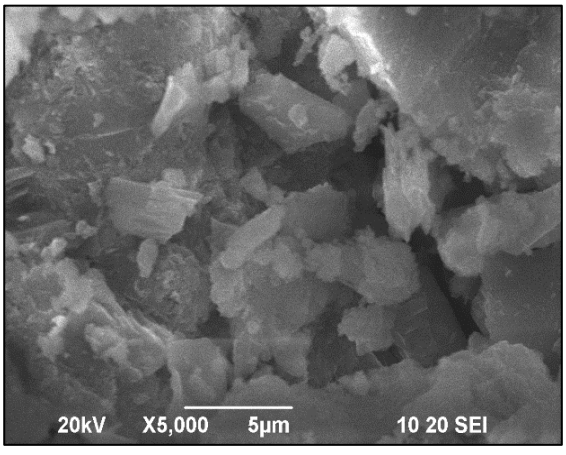

Fig. 7. SEM image of CT2.

4. Conclusions

The following conclusions were drawn from the carried-out experiments:

- All specimens in the fiber-reinforced concrete specimens have exceeded their mean target strength. Notably, the CS2 and CT2 mixes including PP fiber shown excellent performance in both standard water and hostile acid and base environments.
- The strength increased gradually at 1% and 2% of nano-SiO_2 and TiO_2 with 0.5% PP fiber and began to decrease at 3% and 4%; excessive replacement of cement with nano materials with fiber failed to provide suitable bonding.
- CS2 and CT2 flexural strength increased by 8.09% and 6.89% respectively than C1 after 28 days of curing.
- Porosity of CS2 and CT2 was about 16.13% and 13.92% less than the reference concrete.
- Nano-SiO_2 incorporation in concrete is more beneficial than the nano-TiO_2 due to their availability and higher mechanical strength.
- Water absorption value decrease as incorporation of nano materials in concrete at an optimum dosage. All concrete mix specimens have lower than 5%.
- Durability of nano materials concrete is more compared to the referenced concrete.

Acknowledgements

None declared.

Funding

The authors received no financial support for the research, authorship, and/or publication of this manuscript.

Conflict of Interest

The authors declared no potential conflicts of interest with respect to the research, authorship, and/or publication of this manuscript.

Author Contributions

All of the authors made substantial contributions to conception and design, or acquisition of data, or analysis and interpretation of data; were involved in drafting the manuscript or revising it critically for important intellectual content; and gave final approval of the version to be published.

Data Availability

The datasets created and/or analyzed during the current study are not publicly available, but are available from the corresponding author upon reasonable request.

REFERENCES

Chithra S, Senthil Kumar SRR, Chinnaraju K (2016). The effect of colloidal nano-silica on workability, mechanical and durability properties of high performance concrete with copper slag as partial fine aggregate. *Construction and Building Materials*, 113, 794-804.

Feng Y, Zhang B, Xie J, Xue Z, Huang K, Tan J (2023). Effects of recycled sand and nanomaterials on ultra-high performance concrete: Workability, compressive strength and microstructure. *Construction and Building Materials*, 378, 131180.

Hakeem IY, Amin M, Abdelsalam BA, Tayeh BA, Althoey F, Agwa IS (2022). Effects of nano-silica and micro-steel fiber on the engineer-

ing properties of ultra-high performance concrete. *Structural Engineering and Mechanics*, 82(3), 295-312.

IS 383 (2016). Coarse and fine aggregate for concrete – Specification. Bureau of Indian Standards, New Delhi, India.

IS 516 (2021). Testing of strength of hardened concrete. Bureau of Indian Standards, New Delhi, India.

IS 2386 (1963). Methods of test for aggregates for concrete. Bureau of Indian Standards, New Delhi, India.

IS 4031 (1996). Method of physical tests for hydraulic cement. Bureau of Indian Standards, New Delhi, India.

IS 10262 (2019). Concrete mix proportioning – Guidelines. Bureau of Indian Standards, New Delhi, India.

Karthikeyan B, Dhinakaran G (2018). Influence of ultrafine TiO_2 and silica fume on performance of unreinforced and fiber reinforced concrete. *Construction and Building Materials*, 161, 570-576.

Karthikeyan B, Subin, A, Muthulakshmi, T (2020). High strength concrete using ultra-fine TiO_2 and basalt fiber-A study on mechanical and durability characteristics. *Revista Romana de Materiale*, 50(1), 51-58.

Khotbehsara MM, Miyandehi BM, Naseri F, Ozbakkaloglu T, Jafari F, Mohseni E (2018). Effect of SnO_2, ZrO_2, and $CaCO_3$ nanoparticles on water transport and durability properties of self-compacting mortar containing fly ash: Experimental observations and ANFIS predictions. *Construction and Building Materials*, 158, 823-834.

Kim J, Kim, DJ, Park SH, Zi G (2015). Investigating the flexural resistance of fiber reinforced cementitious composites under biaxial condition. *Composite Structures*, 122, 198-208.

Luo Z, Zhi T, Liu X, Yin K, Pan H, Feng H, Su Y (2023). Effects of different nanomaterials on the early performance of ultra-high performance concrete (UHPC): C–S–H seeds and nano-silica. *Cement and Concrete Composites*, 142, 105211.

Marcos-Meson V, Geiker M, Fischer G, Solgaard A, Jakobsen UH, Danner, T, Michel A (2020). Durability of cracked SFRC exposed to wet-dry cycles of chlorides and carbon dioxide–Multiscale deterioration phenomena. *Cement and Concrete Research*, 135, 106120.

Mohseni E, Naseri F, Amjadi R, Khotbehsara MM, Ranjbar MM (2016). Microstructure and durability properties of cement mortars containing nano-TiO_2 and rice husk ash. *Construction and Building Materials*, 114, 656-664.

Murad Y (2021). Compressive strength prediction for concrete modified with nanomaterials. *Case Studies in Construction Materials*, 15, e00660.

Pacheco-Torgal F, Miraldo S, Ding Y, Labrincha JA (2013). Targeting HPC with the help of nanoparticles: an overview. *Construction and Building Materials*, 38, 365-370.

Razak HA, Chai HK, Wong HS (2004). Near surface characteristics of concrete containing supplementary cementing materials. *Cement and Concrete Composites*, 26(7), 883-889.

Reches Y (2018). Nanoparticles as concrete additives: Review and perspectives. *Construction and Building Materials*, 175, 483–495.

Rong Z, Sun W, Xiao H, Jiang G (2015). Effects of nano-SiO_2 particles on the mechanical and microstructural properties of ultra-high performance cementitious composites. *Cement Concrete Composites*, 56, 25-31.

Sharmila P, Dhinakaran G (2016). Compressive strength, porosity and sorptivity of ultra fine slag based high strength concrete. *Construction and Building Materials*, 120, 48-53.

Shi C, Jiménez AF, Palomo A (2011). New cements for the 21st century: The pursuit of an alternative to portland cement. *Cement and Concrete Research*, 41, 750–763.

Son DH, Hwangbo D, Suh H, Bae BI, Bae S, Choi CS (2023). Mechanical properties of mortar and concrete incorporated with concentrated graphene oxide, functionalized carbon nanotube, nano silica hybrid aqueous solution. *Case Studies in Construction Materials*, 18, e01603.

Yoo DY, Oh T, Banthia N (2022). Nanomaterials in ultra-high-performance concrete (UHPC)–A review. *Cement and Concrete Composites*, 134, 104730.

Challenge Journal of Concrete Research Letters

Research Article

Concrete strength monitoring and damage detection using piezoelectric-based wireless sensor

Raju Narwade [a], Ruhita Jadhav [a,*]

[a] *Department of Civil Engineering, Pillai HOC College of Engineering & Technology, Rasayani, 410207 Maharashtra, India*

ABSTRACT

Concrete stands as the predominant and extensively employed structural material in civil engineering. Timely evaluation of concrete strength is essential for maintaining structural safety and minimizing construction delays, thereby avoiding possible structural failures. This early check also ensures that concrete structures can bear loads during construction and throughout their service life. A significant challenge in the construction industry is accurately determining the strength of early-age concrete and identifying potential damage without destructive testing. Conventional techniques often require time-consuming procedures and can be impractical for real-time monitoring. To overcome this issue, IoT-based monitoring systems with piezoelectric sensors provide a practical approach for continuous strength monitoring and damage identification in concrete structures. This study utilized a piezoelectric lead zirconate titanate (PZT) sensor, employing a surface-bonding technique to attach the sensor to the cube specimens. The experimental phase spanned four weeks, including intervals of 7th, 14th, and 28th days by standard construction codes to assess necessary strength levels and identify any damage within the structure. This study verified the results obtained by the piezoelectric-based wireless sensor network are practical and reliable. Correlation coefficient values are analyzed to validate the relationship between data from IoT-based testing and compressive strength. All the results are presented in graphical format, confirming that this non-destructive approach can accurately predict concrete strength and identify structural damage. This study uniquely contributed by validating the use of piezoelectric sensors for continuous, in-situ monitoring of concrete, providing a novel approach to early damage detection and evaluating the structural health of the structure.

ARTICLE INFO

Article history:
Received – December 30, 2024
Revision requested – February 10, 2025
Revision received – February 21, 2025
Accepted – February 24, 2025

Keywords:
Concrete strength
Damage detection
Smart material
Piezoelectric sensor
Wireless sensor network

Citation: Narwade R, Jadhav R (2025). Concrete strength monitoring and damage detection using piezoelectric-based wireless sensor. *Challenge Journal of Concrete Research Letters*, 16(1), 40–50.

1. Introduction

Concrete is the predominant and extensively employed structural material in civil engineering. As the water content diminishes, concrete strength gradually rises, typically reaching its peak around 28 days after casting. Strength development is a consequence of the hydration process, which comprises a sequence of reactions involving cement and water. The primary outcome of this exothermic reaction is the creation of cement gel. After casting, cubes are dried under relative humidity at a constant temperature of 27 °C. This indicates that drying conditions significantly affect the degree of hydration, gradually increasing the compressive strength of concrete cubes (Shafiq and Nuruddin 2010).

Measuring concrete strength is crucial to ensure structural integrity and expedite construction. Two primary approaches exist for this purpose: non-destructive evaluation and destructive evaluation. Destructive methods involve crushing concrete samples to ascertain

* *Corresponding author*. E-mail address: ruhitasj21hmcivil@student.mes.ac.in (R. Jadhav)
ISSN: 2548-0928 / DOI: https://doi.org/10.20528/cjcrl.2025.01.005

strength but could be more practical for monitoring extensive reinforced concrete structures. Ivanchev (2022) explained that the destructive technique provides accurate information on the compressive strength of specimens, but it is more expensive and time-consuming and sometimes weakens the existing structures. Thus, non-destructive techniques are preferred for the real-time monitoring of concrete without damaging the structure. According to Akca et al. (2021), the non-destructive technique has more advantages than the destructive technique, as it can be used multiple times without damaging the specimens. Among the three frequently utilized non-destructive methods are the piezoelectric-based monitoring approach, the hydration heat-based monitoring technique, and the ultrasonic-based monitoring method. According to Hu et al. (2013), piezoelectric-based monitoring is highly effective for structural health monitoring in concrete structures. This method also helps detect any cracks and voids in the structure by utilizing sensors that are either surface-bonded or embedded in concrete. Zhang et al. (2024) explained that the hydration heat-based monitoring technique is crucial in reducing the risk of early-age cracking in concrete structures caused by temperature-induced stress. To prevent this risk, the main focus is monitoring the concrete mix temperature before and after pouring. Lorenzi et al. (2020) highlighted that ultrasonic-based monitoring methods help determine the integrity of the material, improve the quality assurance control during construction, and support rehabilitation decisions.

Various advanced smart materials, such as shape memory alloys, piezoelectric materials, and optical fibers, play an essential role in non-destructive techniques. Mavroidis and Pfeiffer (1999) described how shape memory alloys can regain their original shape after deformation when exposed to particular temperatures. Shape memory alloys are employed in non-destructive testing because of their capacity to change structural configurations, which makes it possible to identify flaws and improve the functionality of intelligent structures. According to Wang et al. (2023), piezoelectric materials generate an electric charge in response to mechanical stress and can conversely induce deformation when an electric field is applied. Due to this dual property, this material is used in structural health monitoring systems as sensors and actuators. This material is generally used for detecting cracks and voids in structures; along with this, it can also be used as a vibration control, energy harvesting, and as an integral component in smart structures. Kuang and Cantwell (2003) explained that optical fibers are used in structural health monitoring due to their sensitivity to strain and temperature changes. Eventually, without compromising the material's properties, the optical fibers help to detect impact damage and monitor structural integrity. Piezoelectric sensors, particularly those made from lead zirconate titanate (PZT), are vital for monitoring structural health. These sensors can be surface-bonded or embedded within concrete to assess integrity based on imped-ance or vibration data. PZTs are characterized by high elastic modulus and brittleness. Modern wireless systems, whether surface-based or embedded, are increasingly employed for their straightforward installation and remote accessibility, enabling continuous monitoring of diverse structural types. Piezoelectric methods are noted for their cost-effectiveness, quick responsiveness, flexibility in design, and straightforward integration. In recent years, piezoelectric sensors have found utility in monitoring concrete strength and detecting damage by integrating them into the host structure. According to Hu et al. (2014), piezoelectric sensors can be used for damage detection by embedding the sensors in concrete slabs with the help of the electromechanical impedance method. The research demonstrated that correlation coefficient deviation and root mean square deviation indices effectively identify the structural damage. Han et al. (2020) explained that a piezoelectric sensor can be used to monitor the strength development of cementitious materials with the help of the electromechanical impedance technique. The study presented here highlights how piezoelectric materials find utility in two essential areas: concrete strength monitoring and identifying damage within concrete structures.

Chaliorisa et al. (2016) introduced WiAM's (Wireless Impedance/Admittance Monitoring System), an innovative real-time structural health monitoring technique. This system is intended to collect voltage-frequency responses from a network of piezoelectric sensors strategically placed on different parts of RC structures. To demonstrate the system's ability to identify damage, the study tested two flexural RC beams subjected to monotonic and cyclic loading and a shear-critical RC beam subjected to monotonic loading. The findings showed WiAM's capability to detect stiffness degradation and damage initiation observing impedance and admittance signature shifts. The results demonstrate that the system detects the course of damage in reinforced concrete structures, offering a valuable tool for structural integrity assessment. Chena et al. (2015) outlined using a wireless sensor network as an alternative to wired data acquisition systems for monitoring concrete strength. The methodology employed two smart aggregates: an actuator to generate high-frequency vibration waves and a sensor to capture these vibrations within the concrete structure. The study relied on two primary wireless nodes: the wireless controller, responsible for sensing and recording vibration data, and the sensing signal conditioner, acting as the wireless coordinator, which generated the actuation signal needed for the smart aggregate's operation. The software implementation was carried out in C language. The network coordinator produced frequencies around 200 Hz, subsequently captured by an oscilloscope for sine excitation. The study's results emphasized the advantages of the wireless system's embedded design, including reduced system size and cost, improved robustness, and enhanced flexibility.

Dumoulin et al. (2015) studied initial-stage concrete monitoring and damage identification using two approaches. The initial method involved tracking the evolution of P-wave velocity in prismatic moulds using smart aggregates known as SMAGs. This method helped assess the hydration process and mechanical property development of concrete. The second method entailed tracking damage evolution in three cube specimens, each

showing cone-shaped failures during pull-out tests. This method helps the piezoelectric transducers effectively capture variation in ultrasonic wave propagation, indicating progressive damage. Fani and Basil (2022) developed a groundbreaking approach called fuzzy linear regression (FLR) to forecast the compressive strength of lightweight foamed concrete. This novel approach integrated trapezoidal fuzzy numbers into the modelling process. The study conducted a comparative analysis to establish the usefulness of the FLR methodology in forecasting the compressive strength of lightweight foamed concrete vs alternative methods such as multivariable nonlinear regression and various single or hybrid machine learning models. Therefore, the study validated that FLR is a reliable alternative to conventional prediction models for lightweight foamed concrete. Feng et al. (2019) presented the innovative concept of the "smart aggregate." This pioneering strategy utilized an active sensing technique that seamlessly incorporated piezoelectric-based transducers. The primary goal was to provide real-time assessments of early-age concrete strength evolution across the critical 0 to 28-day period. To efficiently capture wave responses across the 28-day curing period, two smart aggregates (SAs) were used. One SA performed as an actuator, regularly releasing regulated stress waves, while the second SA served as a sensor capable of detecting stress waves.

Fotouhi et al. (2017) investigated the feasibility of using polyvinylidene fluoride (PVDF) as a sensor element in a passive structural health monitoring (SHM) system. The study explored the integration of piezoelectric nanocomposites into composite materials, emphasizing their high durability, flexibility, and improved signal-to-noise ratio. Their primary focus was on SE70 glass/epoxy laminates used in this sensor system to monitor and assess damage during indentation tests. The study revealed important information about the efficacy of PVDF in SHM for assessing structural integrity. Jerzy S. (2020) extensively examined smart materials in architectural and civil engineering. The study mainly highlighted integrating of smart materials into infrastructure for real-time monitoring, adaptive responses to environmental changes, and energy-efficient improvements. For example, shape memory alloys for adaptive building components, PZT sensors for structural health monitoring, and self-healing concrete for crack repair. This study looked at the various applications and potential benefits of such materials in these fields, emphasizing their contribution to the progress of structural engineering and building approaches. Kuczma et al. (2021) examined a previous inquiry into the sustainability of civil infrastructure and the use of smart materials in civil engineering. The investigation thoroughly examines how incorporating smart materials adds to structural sustainability. Li et al. (2023) proposed a groundbreaking technique for monitoring and forecasting at the initial stages of concrete strength evolution. This method integrates embedded smart aggregates (SAs) based on electromechanical impedance (EMI) technology and machine learning algorithms. The study uses machine learning models to find the correlation between the EMI signature and compressive strength. Because of its simplicity, precision, quantitative capacity, and dependability, it stands out for evaluating and predicting concrete compressive strength.

Noori and Narjabadifam (2019) thoroughly examined a broad spectrum of smart materials and their varied uses within the building sector. This paper highlighted the importance of SHM systems by integrating IoT, AI, and sensor networks. These smart materials contribute to improve real-time data acquisition, enhance urban sustainability, reduce maintenance costs, and improve safety. This insightful analysis offered valuable perspectives into the creative methods employed by these materials to enrich and revolutionize different facets of construction methodologies. Prayuda et al. (2020) presented the implementation of a fuzzy logic methodology for forecasting flexural strength, compressive strength, and flowability in self-compacting concrete. The study utilized a fuzzy-logic prediction model and various mix proportions to estimate the self-compacting concrete based on key parameters for reducing the need for experimental laboratory testing. Providakis et al. (2014) introduced piezoelectric material for identifying damage in concrete reinforcement, utilizing the electromechanical admittance approach. This study presented the laboratory experiments on reinforced concrete specimens to effectively detect changes in structural conditions by monitoring impedance shifts, allowing early identification of reinforcement deterioration. Roy et al. (2016) evaluated smart materials and their various uses in modern structural engineering and building projects. This comprehensive study sheds light on the adaptability and importance of these new materials in defining the future of building and infrastructure development. Samadi and Farrokh (2022) used in-situ experiments and the Adaptive Neuro-Fuzzy Inference System (ANFIS) to forecast concrete's 28-day compressive strength. This ANFIS model predicted concrete strength using diverse input factors such as the water-to-cement ratio and the types of fine and coarse aggregate materials. Saravanan et al. (2017) presented an innovative technology for evaluating concrete strength during the initial stage (3–7 days) and later stages (beyond 7 days) under conditions of large-scale sensor deployment. Under crack opening conditions, this approach detects variations in the EMI signature on PZT-bonded concrete shear walls. This method helps develop a relationship between the strength parameter and root mean square deviation (RMSD).

Sha et al. (2021) demonstrated a compound material comprising cement, epoxy resin, a curing agent, and enhancers. This material was designed to monitor the structural health of concrete structures by utilizing the mechanical sensing capabilities of embedded smart piezoelectric (PZT) sensors. This study highlighted that through a series of experimental tests and numerical simulations, the sensors can detect strain variations, progressive deterioration, and damage initiation in concrete. Shin et al. (2008) presented using the conventional EMI sensing technique alongside PZT patches. This method served to identify and observe the initial development. The study uses an active sensing approach, where PZT sensors generated and received stress waves within the concrete. By analyzing changes in wave propagation characteristics, the study was able to correlate

the sensor data with compressive strength development. This study concluded that PZT sensors offer a practical and effective alternative to conventional destructive testing methods, enabling continuous, in-situ monitoring of concrete curing and early-age strength development. Sobczyk et al. (2021) thoroughly analyzed smart materials in civil engineering and architecture, focusing on using actuators and sensors. The study explained that actuator applications such as kinetic structures, self-regulating facades, and adaptive shading systems demonstrate how smart materials improve energy efficiency and indoor environmental quality. Sensor applications such as environmental sensing, SHM, and occupancy detection contribute to developing of responsive and intelligent buildings. Sun et al. (2020) proposed a computational simulation method to assess the utility of piezoelectric stress wave analysis for monitoring concrete strength. This method uses computer simulations to analyze and determine the effectiveness of concrete strength monitoring by analyzing stress waves generated by piezoelectric sensors. The study developed a finite element model to simulate the interaction between piezoelectric sensors and stress waves in concrete at various curing stages. The study highlighted the correlation between wave velocity and amplitude with the progressive increase in concrete strength. The study concluded that the PZT sensors effectively capture early-age strength development trends by indicating a strong relationship between wave parameters and concrete strength.

Vikram et al. (2023) presented a new piezoelectric cantilever beam electric sensor for pavement monitoring via the Internet of Things (IoT). This pioneering device includes a self-powered wireless acceleration sensor to detect vibrations in small and medium-sized bridges. The study utilizes a PZT sensor to convert mechanical vibrations and stress from vehicular movement into electrical signals, which are then analyzed to assess pavement conditions. Wang et al. (2010) executed an empirical study on monitoring the compressive strength of concrete by integrating embedded piezoelectric lead zirconate titanate (PZT) transducers with the EMI technique. The study concluded that as concrete cures and gains strength, the resonant frequency of the embedded PZT transducers increases, highlighting the strong correlation between resonant frequency and compressive strength. Wu et al. (2022) explained a uniaxial piezoelectric (PZT) sensor tailored to address issues linked to quantifying the output charge of the piezoelectric component. This specialized sensor was incorporated into the concrete framework and situated on its surface to monitor stress, establishing a relationship with the elastic modulus to establish a correlation. Yang et al. (2020) developed a method for monitoring concrete's 28-day age strength by embedding piezoelectric smart aggregates (SA) within glass fiber-reinforced polymer (GRFP) tube columns filled with concrete. The study proposed an innovative, non-destructive method for early-age concrete strength monitoring using power spectral density and wavelet packet analysis by analyzing the vibration response of cube specimens. Zhu (2021) thoroughly analyzed many smart materials' unique properties and prospective applications. The author concentrated on the widespread application in civil engineering, highlighting its function in architectural innovation, strengthening structural integrity, and, ultimately, enhancing structural safety.

According to Zachariah et al. (2023), ThingSpeak is a popular and valuable platform for receiving, hosting, and visualizing sensor data by quickly creating channels. This ThingSpeak platform facilitates online analysis and processing using MATLAB and helps users instantly visualize data presented by devices. Therefore, this study used ThingSpeak, a cloud-based IoT analytics platform that facilitates real-time data visualization and analysis. In addition, NodeMCU, a low-power microcontroller with built-in Wi-Fi capability, processes data and transmits it wirelessly to the cloud for remote monitoring. NodeMCU is an open-source IoT platform with firmware running on the ESP8266 Wi-Fi SoC and hardware based on the ESP-12 module. Due to its affordability and user-friendliness, it is frequently used to create IoT applications with the help of the Lua programming language. According to Ayeni et al. (2024), NodeMCU functionality is based on written code, establishing Wi-Fi connectivity to a predefined network and managing sensor data. ThingSpeak ensures effective data transfer from sensors by enabling smooth interaction with microcontrollers like NodeMCU. ThingSpeak, an IoT-based platform, enables real-time data visualization by converting the transmitted data into graphical representations. ThingSpeak is also helpful for continuous structural health monitoring applications because it supports remote access and real-time data logging.

A statistical relationship between two variables is represented numerically by the correlation coefficient (r or R), which measures some linear association. These variables are derived from observed data, commonly referred to as samples. The correlation values range from -1 to +1, which indicates the most potent possible correlation, and 0 signifies no correlation between variables. Schober et al. (2018) highlighted that the most commonly used correlation coefficient is the Pearson correlation coefficient, which assesses the linear relationship between two continuous variables. Table 1 illustrates how strongly or weakly the variables are associated:

Table 1. Interpreting correlation coefficient values.

r or R (positive/negative values)	Strength or weakness of association between variables
1.0 to 0.90	Very strong
0.89 to 0.70	Strong
0.69 to 0.40	Moderate
0.39 to 0.10	Weak
0.10 to 0.00	Negligible

Previous studies primarily focused on conventional non-destructive testing methods with other integrated IoT and piezoelectric sensors for real-time monitoring of concrete strength and damage detection. Additionally, prior research lacked a well-defined correlation between amplitude values and concrete strength. In contrast, this study mainly focused on surface-bonding techniques for attaching sensors to the cube specimens with wireless data transmission via NodeMCU and ThingSpeak. This study combines compressive strength testing using a CTM and IoT-based testing, allowing for a direct comparison between traditional and advanced monitoring techniques through correlation coefficient analysis. Furthermore, IoT-based testing is used for both concrete strength monitoring and identifying the damage in cube specimens, enhancing the reliability of real-time structural assessment.

2. Methodology

This research was thoroughly investigated to monitor concrete strength and identify structural deterioration using piezoelectric sensors. The study is based on a single circuit diagram, as shown in Fig. 1. This circuit comprised components such as the LM324N operational amplifier, resistors, and capacitors. The experimental configuration, illustrated in Fig. 2, encompasses several components: a waveform generator, a single processing circuit comprising a microcontroller, a Node MCU Wi-Fi module, dual ± 3.3V power supplies, a PZT sensor, and a laptop. The PZT sensors are spaced 120 mm from center to center, as shown in Fig. 3.

This study utilized a pair of PZT sensors measuring 30 mm each. One of these sensors functioned as an actuator, responsible for relaying input data received from the waveform generator operating at a frequency of 10 kHz. Meanwhile, the other sensor served as a receiver, collecting the output data and transmitting it to the microcontroller for subsequent processing. Select the ESP8266 board in the NodeMCU interface, then assign a communication port (COM5) for data collection and transmission to the ThingSpeak platform. ThingSpeak ensures effective data transfer from sensors by enabling smooth interaction with microcontrollers like NodeMCU. Therefore, ThingSpeak and NodeMCU make it possible to analyze and understand gathered data effectively.

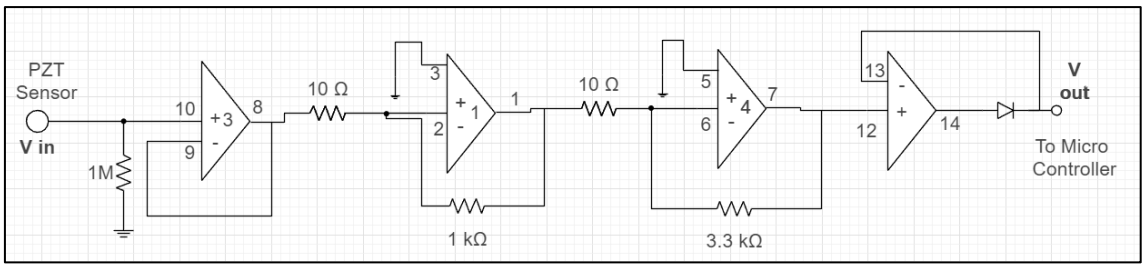

Fig. 1. Single processing circuit diagram.

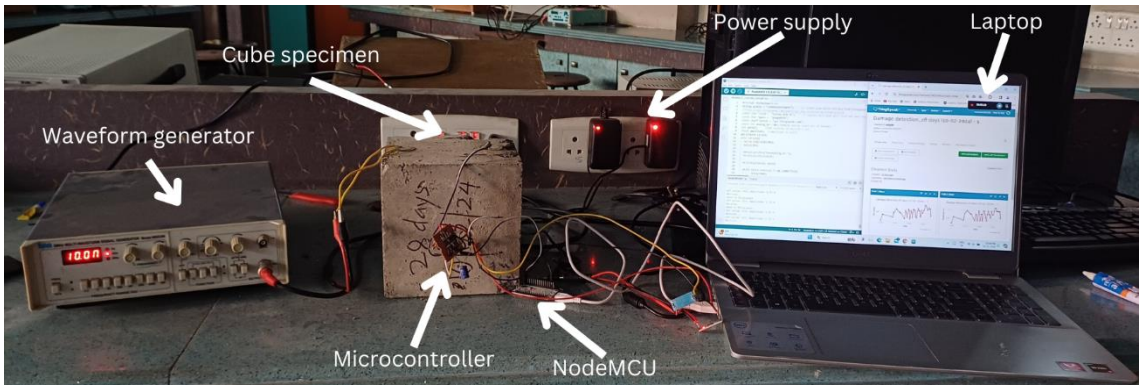

Fig. 2. Experimental setup.

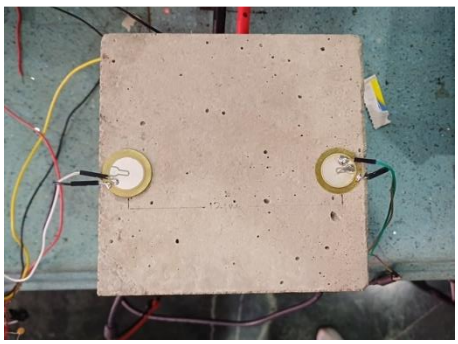

Fig. 3. The PZT sensor positioning.

For this investigation, M30 grade concrete was employed. The components utilized in fabricating the cube specimens were carefully selected to ensure the integrity of the study. These included coarse aggregates (10 mm, 20 mm), fine aggregate (crushed sand), cement (OPC-53 grade), and water. Table 2 provides an overview of the concrete mix proportions specifically designed for M30 grade concrete.

Following the guidelines outlined in IS 456:2000 and IS 516:1959, nine cube specimens were cast, each standard size of 150 mm x 150 mm x 150 mm. According to IS 516:1949, a minimum of three specimens were em-

ployed for each curing period (7th, 14th, and 28th days) to determine the standard testing requirements of strength progression. Despite the limited sample size, this approach ensures a statistically valid representation of compressive strength trends. Subsequently, the identical cube specimens, which were used for IoT-based testing for concrete strength monitoring, underwent testing using a CTM machine. After these tests, damage detection was performed through the IoT-based monitoring system on cube specimens to analyze variations in the results obtained from concrete strength monitoring and damage detection methods. This comparison helps in evaluating the reliability and effectiveness of IoT-based testing in detecting structural changes.

Table 2. The concrete mix proportion for M30 grade.

Sr. No	Item		kg/m³	By weight		Volumetric mix	
1	Cement		405	50	kg	1	bag
2	Fine aggregate	Crushed sand	726.9	89.6	kg	57.8	liter
3	Coarse aggregate	Metal-I	468.2	57.7	kg	38.5	liter
		Metal-II	702.3	86.6	kg	59.7	liter
4	Water		182.5	22.5	liter	22.5	liter
5	Admixture (plasticizer)	Sikament	4.05	0.5	liter	0.5	liter

3. Result and Discussion

The results from the IoT-based testing were for both concrete strength monitoring and damage detection for specific time intervals, including the 7th, 14th, and 28th days. The results of this investigation are depicted graphically, illustrating parameters such as amplitude (V) plotted against time (sec) under the IoT-based method. All the graphs show the total 100 reading output data obtained from the IoT-based testing before CTM testing over cube specimens.

In Fig. 4, the amplitude data observed on the 7th day falls within the range of 0.8 to 1.3 V. Similarly, as depicted in Fig. 5, the amplitude data for the 14th day ranges approximately from 1.15 to 1.3 V. Furthermore, as illustrated in Fig. 6, the amplitude data for the 28th day spans from approximately 1.22 to 1.3 V. These outcomes are detailed at specific time intervals, as outlined in Table 3, providing amplitude data for monitoring concrete strength. As shown in Fig. 7, there is a clear increasing trend in amplitude as the days progress for monitoring concrete strength.

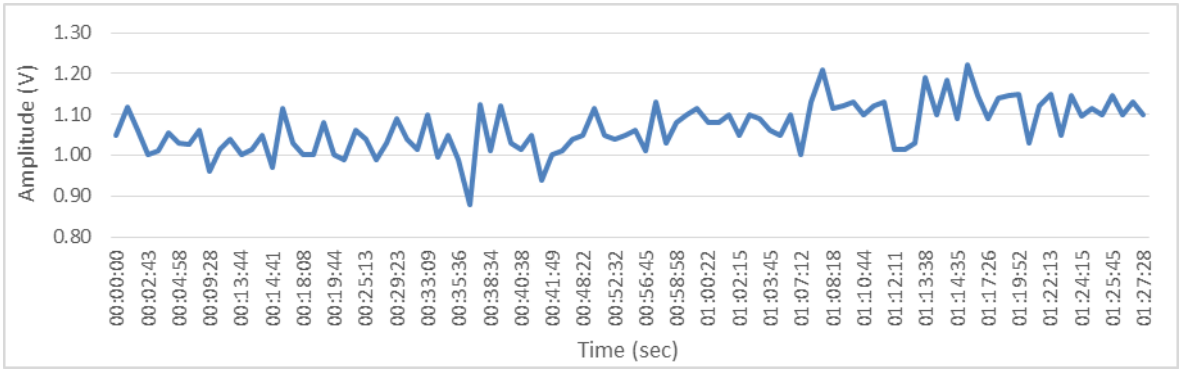

Fig. 4. Amplitude vs. time acquired from IoT-based testing before CTM testing on the 7th day.

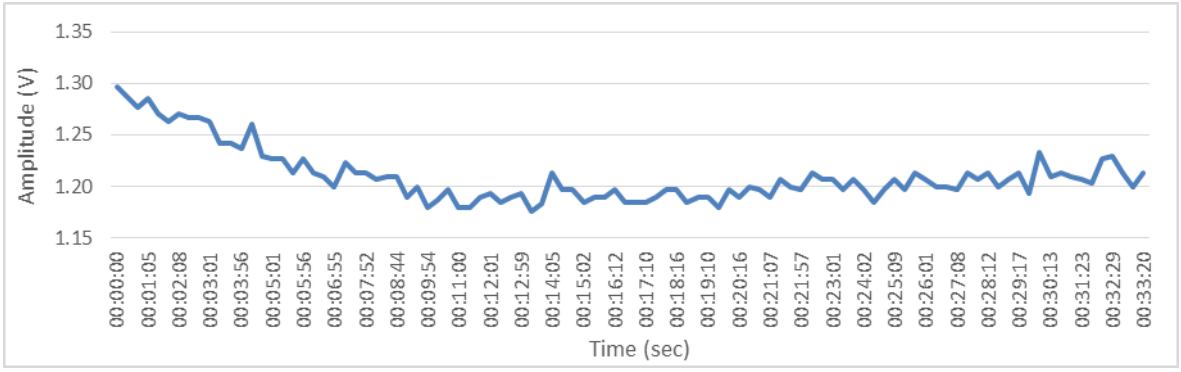

Fig. 5. Amplitude vs. time acquired from IoT-based testing before CTM testing on the 14th day.

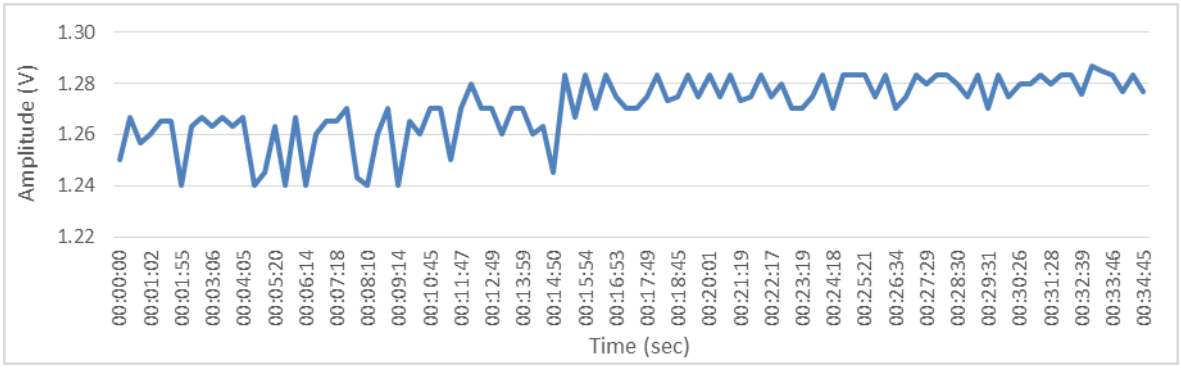

Fig. 6. Amplitude vs. time acquired from IoT-based testing before CTM testing on the 28th day.

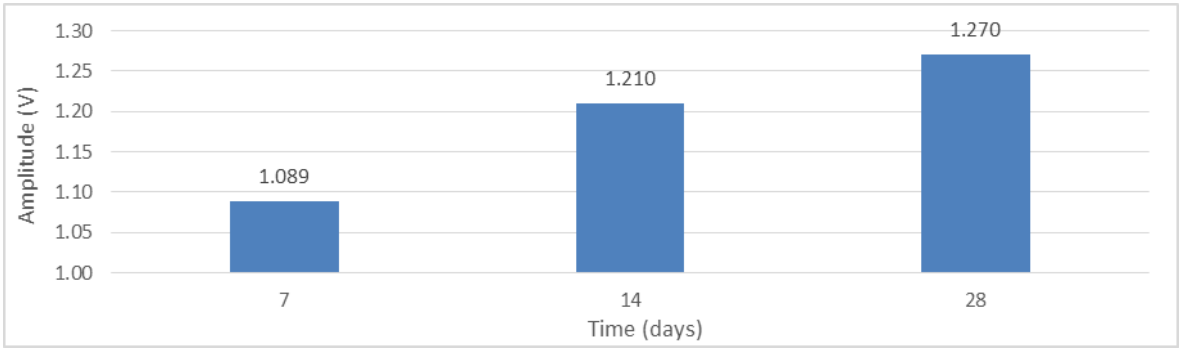

Fig. 7. Amplitude value comparison from IoT-based testing before CTM testing.

Table 3. Amplitude data from IoT-based testing before CTM testing.

Amplitude (V)				
Days	Average	Cube 1	Cube 2	Cube 3
7	1.089	1.133	1.074	1.058
14	1.210	1.231	1.182	1.219
28	1.270	1.273	1.250	1.289

In addition to other methods, this study employs a compressive testing machine (CTM) to quantify the material's compressive strength on the 7th, 14th, and 28th days. To validate the findings from the compressive testing machine (CTM), a formula is outlined in IS 456:2000 to compute the target mean strength of concrete. This mathematical expression is defined in Eq. (1).

$$f'_{ck} = f_{ck} + 1.65 \cdot s \quad (1)$$

where f'_{ck} is the target average compressive strength at 28th days, and s is the standard deviation (from Table 8 of IS 456:2000)

The calculated target compressive strength for M30 grade concrete, derived from the formula above, is 38.25 N/mm². The results of CTM testing are visually represented in Fig. 8 and detailed in Table 4. Consequently, the findings obtained during this investigation indicate a compressive strength of 38.113 N/mm² on the 28th day, which is deemed accurate.

Table 4. Cube compressive strength.

Cube compressive strength (N/mm²)				
Days	Average	Cube 1	Cube 2	Cube 3
7	22.868	22.668	22.512	23.424
14	32.396	32.113	31.892	33.184
28	38.113	37.780	37.520	39.040

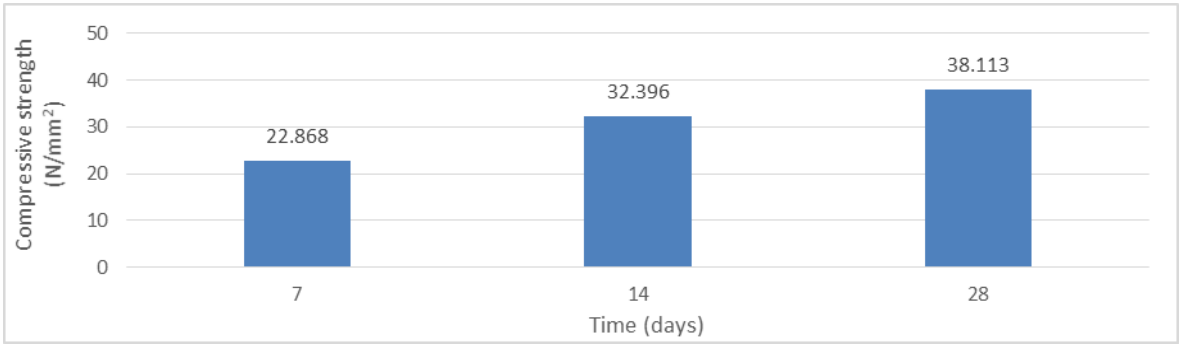

Fig. 8. Compressive strength using CTM testing.

After CTM testing, the damage detection results are depicted graphically, illustrating parameters such as amplitude (V) plotted against time (sec) under the IoT-based method. In Fig. 9, the amplitude data observed on the 7th day falls within the range of 1.0 to 1.6 V. Similarly, as depicted in Fig. 10, the amplitude data for the 14th day ranges approximately from 1.3 to 1.4 V. Furthermore, as illustrated in Fig. 11, the amplitude data for the 28th day spans from approximately 1.4 to 1.44 V. Results are detailed at specific intervals, including the 7th, 14th, and 28th days, as presented in Table 5, showing amplitude data for damage detection after testing the cube specimens under CTM testing. As illustrated in Fig. 12, there is a clear increasing trend in amplitude as the days progress for detecting damage in cubes.

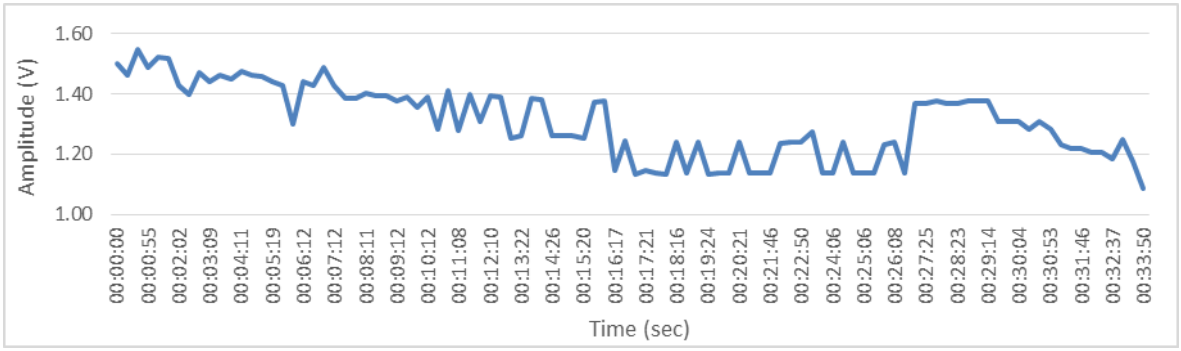

Fig. 9. Amplitude vs. time acquired from IoT-based testing after CTM testing on the 7th day.

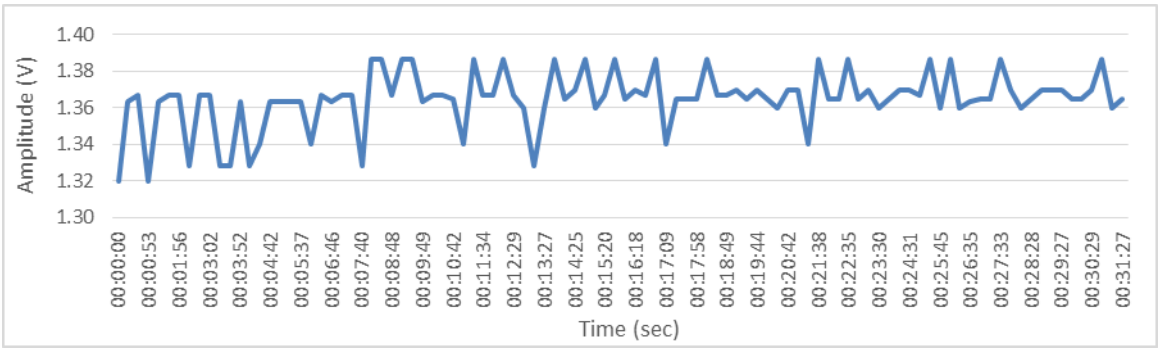

Fig. 10. Amplitude vs. time acquired from IoT-based testing after CTM testing on the 14th day.

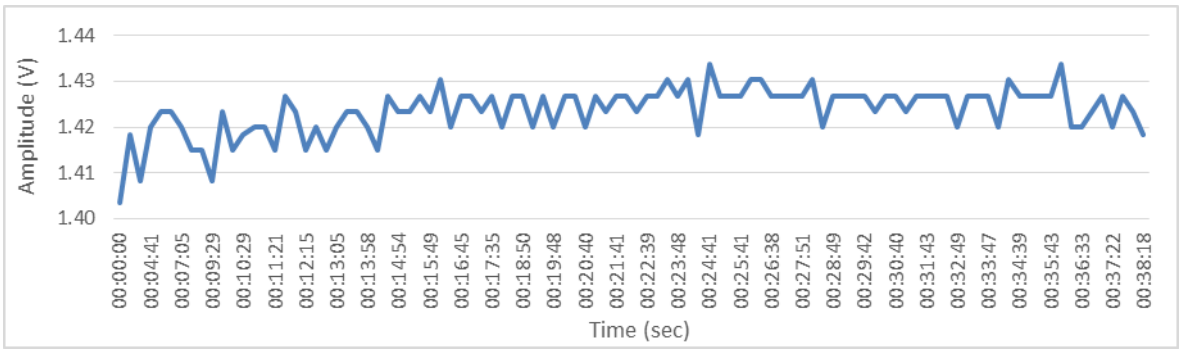

Fig. 11. Amplitude vs. time acquired from IoT-based testing after CTM testing on the 28th day.

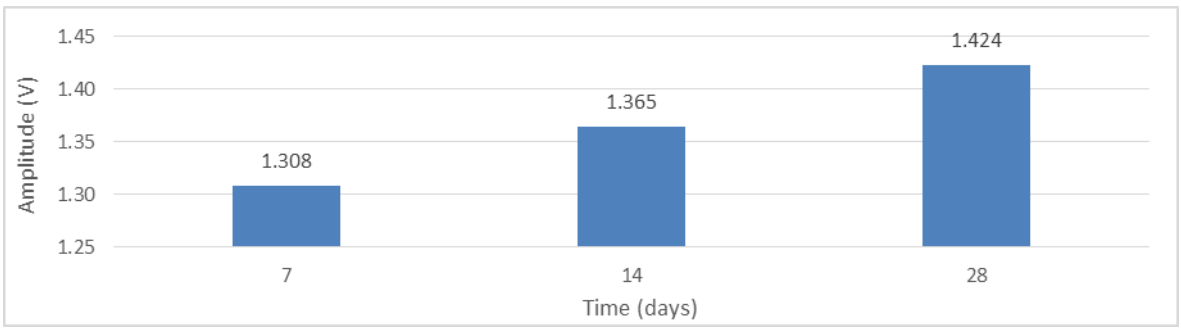

Fig. 12. Amplitude value comparison from IoT-based testing after CTM testing.

Table 5. Amplitude data from IoT-based testing after CTM testing.

Amplitude (V)				
Days	Average	Cube 1	Cube 2	Cube 3
7	1.308	1.261	1.344	1.321
14	1.365	1.342	1.368	1.385
28	1.424	1.394	1.407	1.471

To validate the correlation between amplitude and compressive strength for concrete cubes, Fig. 13 presents a graphical representation between them with the average data provided in Tables 3 and 4. The blue line represents the observed data, while the red dotted line denotes the regression trendline, indicating a positive correlation. The correlation coefficient (r) suggests that higher amplitude values correspond to higher compressive strength. Based on the result obtained from the graph, the correlation of R^2 = 0.9796 (approximately 0.98) is strongly acceptable for practical use in concrete strength monitoring. The linear Eq. (2) obtained from the graph in Fig. 13 is shown below:

$$y = 7.6227 \cdot x + 15.881 \quad (2)$$

where y is the compressive strength (N/mm²), and x is the amplitude (V).

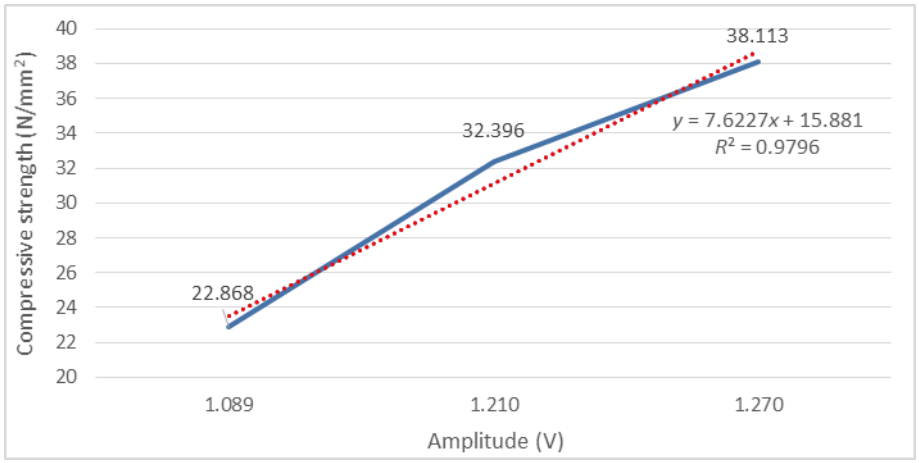

Fig. 13. Correlation between amplitude and compressive strength.

For comparison purposes, the results obtained from IoT-based testing for concrete strength monitoring and damage detection, as shown in Tables 3 and 5, are illustrated in Fig. 14. The results indicate an increase in the values for damage detection compared to concrete strength monitoring on the 7th, 14th, and 28th days. The difference between both results falls within the range of approximately 0.15 to 0.2.

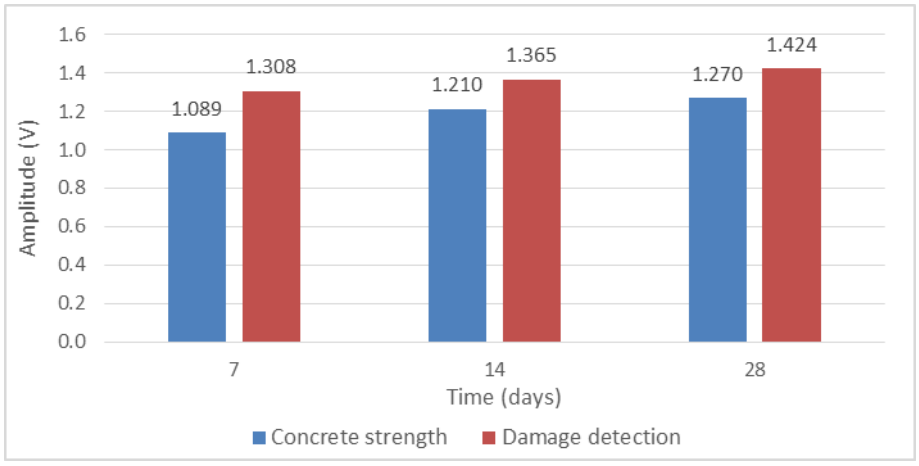

Fig. 14. Comparison between concrete strength and damage detection.

4. Conclusions

A key challenge in the construction industry is the reliance on destructive testing methods, which are time-consuming, labor-intensive, and impractical for real-time concrete strength and structural health monitoring. The present study successfully integrates a piezoelectric lead zirconate titanate (PZT) sensor with an IoT-based monitoring system, offering a practical, non-destructive approach for concrete strength monitoring and damage

detection in concrete structures. The study was conducted on 7th, 14th, and 28th days following standard construction codes. The result demonstrated a strong correlation, R^2=0.9796 (approximately 0.98), between amplitude values and compressive strength, confirming the accuracy and reliability of this non-destructive approach. The recorded compressive strength of 38.113 N/mm^2 on the 28th day closely aligns with the target strength of 38.25 N/mm^2, confirming the effectiveness of the monitoring system. Additionally, damage detection results revealed a consistent increase in amplitude value post-CTM testing, highlighting structural deterioration. This study highlights the benefits of integrating PZT sensors with IoT-based wireless data transmission, enhanced precision, cost-efficiency, and automation in concrete assessment.

For future study, this piezoelectric-based monitoring system can be extended to large-scale structures such as beams, columns, and slabs in real-world applications. For real-time monitoring, some improvements in this monitoring system are necessary. Artificial intelligence (AI) and machine learning models can be integrated to enhance the prediction accuracy of concrete strength and automate damage classification. Additionally, other non-destructive methods can be used for a more holistic evaluation. Future studies should also focus on achieving more accurate results of correlation coefficients (R^2=1) on the same or different grades of concrete to validate the system's reliability further.

Acknowledgements

None declared.

Funding

The authors received no financial support for the research, authorship, and/or publication of this manuscript.

Conflict of Interest

The authors declared no potential conflicts of interest with respect to the research, authorship, and/or publication of this manuscript.

Author Contributions

All of the authors made substantial contributions to conception and design, or acquisition of data, or analysis and interpretation of data; were involved in drafting the manuscript or revising it critically for important intellectual content; and gave final approval of the version to be published.

Data Availability

The datasets created and/or analyzed during the current study are not publicly available, but are available from the corresponding author upon reasonable request.

REFERENCES

Akça B, Keskin SB, Göçügenci A (2021). Predictability of concrete damage level by non-destructive test methods. *Challenge Journal of Concrete Research Letters,* 12(4), 138-150.

Ayeni PO, Adesoba OC (2024). IoT-based home control system using NodeMCU and Firebase. *Journal of Edge Computing*, Early Access.

Chaliorisa C, Karayannis C, Angeli G, Papadopoulos N, Favvata M, Providakis C (2016). Applications of smart piezoelectric materials in a wireless admittance monitoring system (WiAMS) to structures—Tests in RC elements. *Case Studies in Construction Materials*, 5, 1–18.

Chena J, Li P, Song G, Ren Z (2015). Piezo-based wireless sensor network for early-age concrete strength monitoring. *Optik*, 127(5), 2983–2987.

Dumoulin C, Karaiskos G, Deraemaeker A (2015). Concrete monitoring using embedded piezoelectric transducers. *Encyclopedia of Earthquake Engineering*, 94(1), 1-12.

Fani I, Basil K (2022). The use of fuzzy linear regression with trapezoidal fuzzy numbers to predict the compressive strength of lightweight foamed concrete. *Mathematical Modelling of Engineering Problems*, 9(1), 1-10.

Feng Q, Liang Y, Song G (2019). Real-time monitoring of early-age concrete strength using piezoceramic-based smart aggregates. *Journal of Aerospace Engineering*, 32(1), 04018115.

Fotouhi M, Xiao B, Pozegic T, Jalalvand M, Hamerton I, Wisnom M (2017). High performance piezo electric nanocomposite sensor nodes for structural health monitoring. *21st International Conference on Composite Material*, 1-9.

Han G, Su YF, Lu N (2020). Mechanism for using piezoelectric sensor to monitor strength gain process of cementitious materials with the temperature effect. *Journal of Intelligent Material Systems and Structures*, 32(10), 1-12.

Hu B, Kundu T, Grill W, Liu B, Toufigh V (2013). Embedded piezoelectric sensors for health monitoring of concrete structures. *ACI Materials Journal,* 110(2), 149-158.

Hu X, Zhu H, Wang D (2014). A study of concrete slab damage detection based on the electromechanical impedance method. *Sensors,* 14(10), 19897-19909.

IS 456:2000 (2000). Indian Standard Plain and Reinforced Concrete – Code of Practice (Reaffirmed 2005). Bureau of Indian Standards, Manak Bhavan. 9 Bahadur Shah Zafar Marg, New Delhi, India.

IS 516:1959 (1959). Indian Standard Methods of test for Strength of Concrete (Reaffirmed 2004). Bureau of Indian Standards, Manak Bhavan. 9 Bahadur Shah Zafar Marg, New Delhi, India.

Ivanchev I (2022). Investigation with non-destructive and destructive methods for assessment of concrete compressive strength. *Applied Sciences,* 12(23), 12172.

Jerzy S (2020). Application of smart materials in civil engineering and architecture. *2020 World Symposium on Smart Materials and Applications*, 958, 012006.

Kuang K, Cantwell W (2003). The use of plastic optical fibres and shape memory alloys for damage assessment and damping control in composite materials. *Measurement Science and Technology,* 14(8), 1305.

Kuczma M, Tabrizikahou A, Nowotarski P, Kwiatek M, Javanmardi A (2021). Sustainability of civil structures through the application of smart materials: a review. *Materials*, 14(17), 4824, 1-29.

Li G, Luo M, Huang J, Li W (2023). Early age concrete strength monitoring using smart aggregate based on electromechanical impedance and machine learning. *Mechanical Systems and Signal Processing*, 186, 109865.

Lorenzi A, Stein K, Reginatto LA, Pinto da Silva Filho LC (2020). Concrete structures monitoring using ultrasonic tests. *Revista de la Construcción,* 19(3), 246-257.

Mavroidis C, Pfeiffer C (1999). Conventional actuators, shape memory alloys, and electrorheological fluids. *Research in Nondestructive Evaluation,* 14, 1-32.

Noori M, Narjabadifam P (2019). Innovative civil engineering applications of smart materials for smart sustainable urbanization. *Journal of Civil Engineering and Urbanism*, 9(4), 24-35.

Prayuda H, Monika F, Saleh F, Prabandaru P, Emerald J, Maulida N (2020). Prediction of flowability compressive and flexural strength on self-compacting concrete using fuzzy logic. *Advances in Engineering Research*, 199, 89-97.

Providakis C, Angeli GM, Favvata MJ, Papadopoulos N, Chaliorisa C, Karayannis C (2014). Detection of concrete reinforcement damage using piezoelectric materials - analytical and experimental study. *International Journal of Civil, Architectural, Structural and Construction Engineering*, 8(2), 197-205.

Roy S, Mishraand H, Mohapatro BG (2016). Creating sustainable environment using smart materials in smart structures. *Indian Journal of Science and Technology*, 9(30), 1-9.

Samadi H, Farrokh E (2022). Prediction of compressive strength of concrete using Adaptive neuro-fuzzy inference system. *International Conference on Civil Structural and Earthquake*, 1-9.

Saravanan T, Balamonica K, Priya B, Gopalkrishnan N, Murthy S (2017). Piezoelectric EMI–based monitoring of early strength gain in concrete and damage detection in structural components. *Journal of Infrastructure Systems*, 23(4), 04017029.

Schober P, Boer C, Schwarte LA (2018). Correlation coefficients: Appropriate use and interpretation. *Anesthesia & Analgesia,* 1266(5), 1763-1768.

Sha F, Xu D, Cheng X, Huang S (2021). Mechanical sensing properties of embedded smart piezoelectric sensor for structural health monitoring of concrete. *Research in Nondestructive Evaluation*, 32(2), 88–112.

Shafiq N, Nuruddin F (2010). Degree of hydration of OPC and OPC/FA pastes dried in different relative humidity. *Concrete Research Letters*, 1(3), 81-89.

Shin WS, Qureshi AR, Lee JY, Yun CB (2008). Piezoelectric sensor based non-destructive active monitoring of strength gain in concrete. *Smart Materials and Structures*, 17(5), 055002, 1-8.

Sobczyk M, Wiesenhütter S, Noennig JR, Wallmersperger T (2021). Smart materials in architecture for actuator and sensor applications: A review. *Journal of Intelligent Material Systems and Structures*, 33(3), 379–399.

Sun W, Fu TY, Li B, Sun L (2020). Numerical study of monitoring of early-age concrete strength development using PZT induced stress wave. *IOP Conference Series: Materials Science and Engineering*, 789, 012058.

Vikram V, Rajkumar U, Jayaseelan D (2023). An initial investigation of a pavement monitoring platform based on the internet of things using a piezoelectric cantilever beam electric sensor. *Dogo Rangsang Research Journal*, 13(3), 95-99.

Wang W, Xiang Y, Yu J, Yang L (2023). Development and prospect of smart materials and structures for aerospace sensing systems and applications. *Sensors,* 23(3), 1545.

Wang DS, Yu LP, Zhu HP (2010). Strength monitoring of concrete based on embedded PZT transducer and the resonant frequency. *Proceedings of the 2010 Symposium on Piezoelectricity Acoustic Waves and Device Applications*, 202-205.

Wu C, Xiang H, Jiang S, Ma S (2022). Stress monitoring of concrete via uniaxial piezoelectric sensor. *Sensors*, 22(11), 4041.

Yang X, Yang W, Li S, Wu C (2020). Early age concrete strength monitoring using power spectral density and wavelet packet analysis. *Advances in Civil Engineering*, 2020, 1-11.

Zachariah T, Klugman N, Dutta P (2023). ThingSpeak in the wild: Exploring 38K visualizations of IoT Data. *SenSys'22: Proceedings of the 20th ACM Conference on Embedded Networked Sensor Systems,* 1035-1040.

Zhang S, Liu P, Liu L, Huang J, Cheng X, Chen Y, Chen L, He S, Zhang N, Yu Z (2024). Heat of hydration analysis and temperature field distribution study for super-long mass concrete. *Coatings,* 14(3), 369.

Zhu S (2021). Study on smart materials using in civil engineering. *Advances in Social Science, Education and Humanities Research*, 631, 1462-1466.